MICROCOPY RESOLUTION TEST CHART

NATIONAL BUREAU OF STANDARDS 1963 A

DTIC

AN OPTICALLY IMPLEMENTED KALMAN
FILTER ALGORITHM

THESIS

AFIT/GEO/EE/84M-2   WILLIAM A. ROEMER
                      CAPTAIN   USAF

DTIC

MAY 1 7 1984

A

DEPARTMENT OF THE AIR FORCE
AIR UNIVERSITY
AIR FORCE INSTITUTE OF TECHNOLOGY

Wright-Patterson Air Force Base, Ohio

84   05   15   010

AFIT/GEO/EE/ 84M-2

AN OPTICALLY IMPLEMENTED KALMAN
FILTER ALGORITHM

THESIS

AFIT/GEO/EE/ 84M-2   WILLIAM A. ROEMER
                        CAPTAIN   USAF

A

AN OPTICALLY IMPLEMENTED KALMAN
FILTER ALGORITHM

THESIS

Presented to the Faculty of the School of Engineering

of the Air Force Institute of Technology

Air University

in Partial Fulfillment of the

Requirements for the Degree of

Master of Science in Electrical Engineering

by

William A. Roemer B.S.E.

Captain   USAF

Graduate Electro-Optics

December 1983

Preface

This study is a continuation of the effort to design an effective tracking algorithm for use with one of the Air Force Weapons Laboratory's high energy laser weapons. The proposed tracker implements a stochastic estimation algorithm requiring a high level of computation through use of optical processing techniques.

I wish to thank my research advisor, Dr. Peter S. Maybeck, for his unflagging patience and invaluable support. His dedication to his students is well known at the Air Force Institute of Technology and will always be remembered.

I would also like to thank my wife, Stacy, for her support during this difficult period. Her shouldering of a myriad of additional responsibilities remains a sacrifice I deeply appreciate. Finally, I would like to express my appreciation to the selection committee of the Air Force Institute of Technology for affording me this chance to improve my limited abilities.

Contents

Contents

List of Figures

List of Figures

List of Tables

List of Symbols

Symbol

x_I, y_I, z_I	Inertial Coordinate System Dimensions
x_T, y_T, z_T	Target Coordinate Frame Dimensions
$r_H(t)$	Horizontal Tracker to Target Range
$r(t)$	Tracker to Target Slant Range
$\underline{x}_D(t)$, $\underline{x}_A(t)$	State Vectors
$\underline{\dot{x}}_D(t)$, $\underline{\dot{x}}_A(t)$	Time Derivatives of State Vectors
$\underline{F}_D(t)$, $\underline{F}_A(t)$	State-Space Plant Matrices
$\underline{B}_D(t)$	Control Input Distribution Matrix
$\underline{u}_D(t)$	Control Input Vector
$\underline{G}_D(t)$, $\underline{G}_A(t)$	Noise Weighting Matrices
$\underline{w}_D(t)$, $\underline{w}_A(t)$	White Noise Vectors
$\underline{f}[\underline{x}(t),\underline{u}(t),t]$	Nonlinear State Description Driven by Inputs over Time
t_{i+1}	Discretized Time Representing Next Sample Point
t_i	Discretized Time Representing Current Sample Point
$\underline{\Phi}(t_{i+1},t_i)$	State Propagation Matrix
$\underline{Q}$	Noise Variance Matrix
$\sqrt{}$	Cholesky Square Root Decomposition
p_1, p_2	Poles for Atmospheric Shaping Filter
$\alpha(t)$	FLIR Image Plane Horizontal Position
$\dot{\alpha}(t)$	FLIR Image Plane Horizontal Velocity
$\beta(t)$	FLIR Image Plane Vertical Position
$\dot{\beta}(t)$	FLIR Image Plane Vertical Velocity
$I(\alpha,\beta)$	FLIR Image Plane Pixel Intensity Array
α_p, β_p	Coordinates of I_{Max}
I_{Max}	Maximum Target Intensity
v_{pl}	Target Velocity Component Perpendicular to the Line of Sight from the FLIR Image Plane to the Target
v	Inertial Target Velocity
σ_L, σ_S	Eigenvalues of Truth Model Image Intensity Ellipse
ω_p	Pull-Up Maneuver Rate

List of Symbols

Symbol

γ	Target Velocity Plane to FLIR Image Plane Angle
δ	Target Length
σ_L', σ_S'	Target Length Projections Parallel to the FLIR Image Plane
Ψ	FLIR Image Plane Horizontal Angle Subtended by Projected Target Hot Spot Offset
Ω	FLIR Image Plane Vertical Angle Subtended by Projected Target Hot Spot Offset
$\bar{I}_{lm}(t_i)$	Discrete Time Measurement Array due to a Hot Spot Target
$n_{lm}(t_i)$	Discrete Time Noise due to Spatial Correlations
$\vec{e}_\alpha$, $\vec{e}_\beta$	FLIR Image Plane Unit Vectors
$\vec{e}_{m\alpha}$, $\vec{e}_{m\beta}$	Unit Vectors of FLIR Image Plane Translated to the Target Center of Mass
$\vec{e}_{ax}$, $\vec{e}_{ay}$, $\vec{e}_{az}$	Unit Vectors of the Plane Defined by the Target
$\vec{e}_x$, $\vec{e}_y$, $\vec{e}_z$	Unit Vectors of the Plane due to a Target Roll Maneuver
ω_r	Roll Maneuver Rate
ϕ	Roll Displacement Angle
$\Delta_{m\alpha}$, $\Delta_{m\beta}$	Projected Target Hotspot Offsets Parallel to the FLIR Image Plane
$\underline{h}[\underline{x}(t_{i+1}), t_{i+1}]$	Nonlinear Measurement Model Matrix Representing the Intensity of Each Pixel
$F[\cdot]$	Fourier Transform
$F^{-1}[\cdot]$	Inverse Fourier Transform
$\underline{g}(\alpha,\beta)$, $\underline{l}(\alpha,\beta)$	Target and Template Intensity Arrays
$\underline{G}(f_\alpha,f_\beta)$, $\underline{L}(f_\alpha,f_\beta)$	Fourier Transforms of Intensity Arrays
$\underline{R}(\alpha,\beta)$	Cross-Correlation of Target and Template
$\underline{C}(\alpha,\beta)$	Target FLIR Image Plane Center of Mass Location Vector
$T_0(\quad y)$	Fraunhofer Diffraction Pattern
$T_0(\quad f_y)$	Fourier Transform Spatially-Expressed Frequencies
λ	Light Wavelength

ix

List of Symbols

Symbol

f	Lens Focal Length
L	Lens
v_α, v_β	FLIR Image Plane Target Velocity Estimates
a_α, a_β	FLIR Image Plane Target Acceleration Estimates
$\underline{z}(t_i)$	Filter Measurement Vector
α_c, β_c	Coordinates of Target Center of Mass
$\underline{H}$	Measurement State-Space Distribution Matrix
$\underline{v}(t_i)$	Measurement Noise Vector
$\underline{K}(t_i)$	Kalman Filter Optimal Gain Matrix
$\underline{R}(t_i)$	Measurement Covariance (Uncertainty) Matrix
$\underline{P}(t_i)$	State-Space Covariance (Uncertainty) Matrix
$\sigma_{DF}^2, \sigma_{AF}^2$	White Process Power Spectral Density Values
τ_{DF}, τ_{AF}	Correlation Times
v_s	Velocity of Sound in a Crystal
n	Crystal Index of Refraction
ν_s	Sound Frequency
M_ω	AOM Figure of Merit Relative to Water
T	Major Time Period
τ	AOM Delay Time
ω	Acceleration Parameter
α_0	Crystal Sound Frequency Attenuation
$\overline{E}(t_i)$	Monte Carlo Ensemble (Mean) Error
$e(t_i)$	Estimated Error
σ_B	RMS Value of Background Noise
AR	Aspect Ratio
σ_v	Standard Deviation of Target Intensity Pattern along Ellipse Semimajor Axis
σ_{pv}	Standard Deviation of Target Intensity Pattern along Ellipse Semiminor Axis
Θ	AOM Bragg Angle
θ	Angular Orientation of Target Coordinate Frame to Inertial Coordinate System

List of Symbols

Abstract

An extended Kalman filter algorithm which incorporates an enhanced correlator/linear measurement model and a nonlinear target acceleration dynamics model is described for use in a pointing and tracking system for high-energy ground-based laser weaponry. The measurement model used in the filter combines the computational benefits of a correlation algorithm with the statistical accuracy available from a Kalman filter. The dynamics model, based on a constant turn-rate target acceleration model, is deemed to be a better representation of the true target dynamics than a linear first-order Gauss-Markov target acceleration model for the cases of interest. Optical processing techniques are completely specified for the correlation stage to perform the required correlation in real time, and the filter stage to perform the linear algebra required for the Kalman filter. This extensive use of optics allows the development of two tracking algorithms based on the same models: a FLIR-constrained tracker with a 30 Hz frame rate and an unconstrained tracker with a 100 Hz frame rate using real-time sensors in place of the FLIR.

I. Introduction

1.1 - Overview

The decision by the Department of Defense to undertake massive development of high energy laser weapons required solutions to a number of highly complex problems in a wide range of specialty areas. While some of these solutions are fairly well developed, there remain major issues yet to be addressed in the pointing and tracking problem in order to achieve a fully acceptable aiming system.

To understand what issues must be addressed requires a review of systems development to date. Since all of the unclassified efforts which are applicable to the system development within this thesis have been generated at the Air Force Institute of Technology (AFIT) under the guidance of Dr. Peter S. Maybeck, this review will be limited to these efforts. The solutions obtained from this previous work will serve to highlight the advantages and limitations available at the starting point of this effort.

Additionally, as most control engineers lack a background in the field of optical processing, a brief review of the field with particular emphasis on algorithms usable in Kalman filter applications is included. While many of the recently developed optical techniques are highly complex to people outside of the field, they warrant investigation as potential candidates for improving the overall filter performance. This review, along with the development of the specific optical architecture in Chapter IV, will demonstrate that an optical solution includes a number of advantages specifically applicable to the limitations inherent to software versions of the present Kalman filter solutions.

The remainder of this introduction will be built on the review of solutions which exhibit the greatest potential

towards an overall solution of the pointing and tracking problem. The overall solution obtained, using the advantages of an optically-processed Kalman filter to offset previously obtained limitations, will then be presented as the optimal solution within the remainder of this thesis.

1.2 Pointing and Tracking Solution Review

The initial system solution (12,16,20) generated at AFIT used a four-state simple extended Kalman filter to track targets using outputs from a forward-looking infrared (FLIR) sensor as measurements. This technique allowed exploitation of knowledge unused by prior correlation tracker developments: size, shape, and motion characteristics of the target; atmospheric jitter spectral description; and background and sensor noise characteristics. Monte Carlo performance analyses indicated an enhanced ability of the nonadaptive filter to track a realistic distant point source target with an error standard deviation of 0.2 picture elements (where picture elements correspond to a field of view of 20 μrad by 20 μrad), under expected tracking conditions.

Although the simple extended Kalman filter approach achieved very accurate tracking performance under the nominally assumed conditions, robustness studies portrayed a significant degradation in performance when the filter's internal model did not depict the target's intensity profile or motion characteristics well (7,13,14). Background noise properties were shown to be of secondary importance at expected signal-to-noise ratios. These studies emphasized the need for better models and adaptivity within the filter structure.

Further analysis resulted in incorporation of an eight-state filter using a modified target dynamics model as well as online adaptation to target shape effects, changing target motion characteristics, and maximum signal intensity (7,14). This was shown to possess considerable performance potential for highly maneuverable targets despite background clutter.

2

Improvements to the solutions generated by the initial research efforts were incorporated into the third major AFIT system development (19,23). This investigation was based on a tracker able to handle "multiple hot spot" targets, in which digital (or potentially optical) signal processing was employed on the FLIR data to identify the underlying target shape. This identified shape was then used in the measurement model portion of the filter as it estimated target position offset from the center of the field of view. The algorithm then used an extended Kalman filter to process the raw intensity measurements from the FLIR to produce target estimates.

An alternate algorithm also developed within this research effort used a linear Kalman filter to process the position indications of an enhanced correlator in order to generate tracking estimates. This enhancement was achieved by: (1) thresholding to reject lower values of the correlation function so that a simple centroid calculation yielded a result close to the peak of the correlation function; (2) incorporation of the dynamics information from the Kalman filter; and (3), use of the online-identified target shape as a template instead of merely using previous frames of data. Both algorithms, under performance analyses using various tracking environment conditions and different choices of design parameters, exhibited significant potential, with the correlation/filter tracker involving less computational burden in actual implementation.

The final model proposed at AFIT for use in an extended Kalman filter was the constant turn-rate target acceleration model. Target trackers based on this alternative dynamics model were initially developed for both air-to-air (29) gunnery (estimation in three dimensions) and FLIR focal plane (5) target intensity tracking (in two dimensions). Although the extended Kalman filter based on a constant turn-rate target acceleration model was found to outperform both an

3

extended Kalman filter based on a Brownian motion accelera-
tion model and a multiple acceleration model adaptive extended
Kalman filter in two-dimensional estimation, subsequent per-
formance analyses (8,21) indicated that comparable performance
can be achieved in the majority of scenarios through use of
the enhanced correlator/linear Kalman filter combination
based on a first-order Gauss-Markov target acceleration dynam-
ics model. For cases where the target being tracked is at
close range or is performing evasive maneuvers, the extended
Kalman filter based on the constant turn-rate target accel-
eration model significantly outperforms all of the other
filters which have been outlined. However, the computational
burden imposed by a software implementation of the constant
turn-rate filter as previously defined (5) has strongly
motivated use of the linear Kalman filter.

The computational burden is due to two factors. First,
incorporation of the constant turn-rate target acceleration
model yields nonlinear propagation equations as compared to
the linear propagation equations generated by use of the
first-order Gauss-Markov target acceleration model. Secondly,
the constant turn-rate filter as originally defined used the
individual FLIR pixel intensities as its input. This design
required the measurement update equations to be nonlinear as
well, a problem not encountered when the enhanced correlator
produces target position offsets from the center of the FLIR
field of view. Combining the additional processing require-
ments due to these two sources of nonlinearities with the
requirement of real-time performance compatible with the FLIR
sensor's 30 Hz frame rate, it is easy to see the preference
accorded the enhanced correlator/linear Kalman filter ap-
proach.

However, the filter design which yields the best perfor-
mance against the widest range of target scenarios is the
constant turn-rate nonlinear filter. Use of this filter thus
requires that a method of implementation of the algorithm

4

having sufficient system throughput capacity be developed, or that the constant turn-rate dynamics model be combined with the linear measurement model of the enhanced correlator, or both. To develop an optimal aiming system (given the developments to date), the computational burden problem must be overcome.

1.3 Optical Processing Developments

The greatest single asset available through the use of optical architectures is the ability to modulate an extremely high density of data in parallel over one or more spatial dimensions. Use of this asset has tremendously increased system throughput capacity over comparable electronic counterparts.

An additional advantage of optical processing is the "memorylessness" of the components used. Specifically, this advantage allows a large array of functions to be accomplished by a single architecture (e.g., matrix-vector, matrix-matrix, and matrix-matrix-matrix multiplies as well as matrix inversion). Optical architectures are not locked into specific functions.

Recent work within the field of optical processing has included the investigation and development of solutions which incorporate algorithms quite similar to those outlined in Section 1.2. Methodologies for direct transfer of linear algebra to optical architectures have also been outlined. These results, when combined with previously available optical processes, have produced powerful tools which cannot be duplicated with a purely electronic configuration.

Recent developments in transfer methodologies have taken a field once limited solely to Fourier-domain analysis to other transform applications (e.g., optical Mellin transforms), subsets of which have high applicability to problems where the image pixel data is statistically either stationary or nonstationary (9). Optical architecture implementations of such specific functions as matrix inversion (3,4,22),

matrix-matrix multiplication (3,4,10), matrix-vector products (3,4,10), and simple Kalman filters (2) have been detailed for bulk optical configurations. Configurations for all of these functions have also been developed using integrated optical architectures (27), an area which has significant potential for size, weight, and power consumption reductions as well as possessing an inherent advantage in system isolation stability.

Furthermore, use of these architectures has been demonstrated for a wide variety of applications, many of which are almost directly transferable to portions of the pointing and tracking problem. The electro-optic inversion of a complex covariance matrix generated by a phase-array radar (22) represents a potential solution, should a phased array optical imaging configuration be implemented. Several recent developments in optical tunable notch filtering (26) can be reconfigured for the bandpass instead of the bandreject case and represent significant signal enhancement potential. Multi-dimensional correlators (1) have already been deployed and are performing several highly complex algorithms in real time. Although all of these systems have a large potential for future optimization, their current configurations as referenced represent an increase in system bandwidth over their electronic counterparts of from two to four orders of magnitude.

Each of these architectures can be characterized by the type of modulator used to perform the processing operations. This is due to the fact that the performance abilities of any optical architecture are essentially limited by the operating characteristics (modulation dimensions, response time, modulation efficiency, and dynamic range) of the modulator, since it almost always is the only non-passive system element and thus is subject to more corruptive processes. However, because its role is so critical, modulator design and

6

development have an extremly high priority in the field of
optics, and both many different types and many differnt
modulators are available to the optical architect. There
are several different types of point modulators (not dis-
cussed here because they are generally not applicable to
optical processing), as well as linear and two-dimensional
modulators. Linear modulators (30) are generally limited
to either acousto-optic or electro-optic effects as the
type of modulation, whereas two-dimensional modulators
use many different types of modulation criteria. For exam-
ple, included within the subset of available two-dimensional
modulators are liquid crystal light valves (23), magneto-optic
modulators (4), and deformable mirror assemblies (10). Each
of these types of modulators has spawned a series of archi-
tectures which are capable of performing various functions
and which maximize the operational characteristics of the
particular device while circumventing its limitations as well
as possible. All of the previously outlined architectures
use one or another of these modulators, with each specific
problem solution having components matched to the particular
modulator to produce an optimal solution insofar as the
optics is concerned.

The use of optical architectures will be encountered
throughout the research as a method of overcoming the
limitations of the best algorithms currently available.
A more thorough review of the optical developments used
will be included within the appropriate chapters.

1.4 Thesis Problem

Laser weaponry is currently envisioned for use in a
multiplicity of scenarios: ground-to-air, air-to-air, and
space-to-space. As required system performance as well as
system operational parameters vary with application, limi-
tation of the design to one particular scenario is indi-
cated. Since initial feasibility studies and testing will

7

be for a ground-based version of the system, the problem scope will be limited to this scenario. Additionally, as a simpler problem, it is more useful for a feasibility-of-concept demonstration.

The proposed problem, therefore, is the complete mathematical development and performance analysis of a pointing and tracking system having an optical data processor as its core for a ground-based laser weapon. The scope of the problem will thus include model development, choice of sensors exhibiting optimal throughput as well as low noise characteristics, and recommendations for future efforts based on current developments. The mathematical development and all performance analyses will be forcibly restricted to real world constraints by limiting all component selection to off-the-shelf units having well-characterized performance criteria.

The overriding goal of this research will be to demonstrate that the benefits offered by the use of optics are both available and deployable now. Additionally, the thesis will demonstrate that use of optical techniques will enable the employment of even more sophisticated dynamics models (should they be developed in the future) by having more than sufficient system bandwidth in reserve or obtainable through alternate component selection. These demonstrations will form the central core of the proposed approach.

1.5 Approach

The overall system concept plan embodies a heretofor unexplored tracking algorithm: the enhanced correlator linear measurement model combined with the nonlinear constant turn-rate dynamics model as described in Section 1.2. While there are several justifications for using this approach (all of which will be outlined), the central fact remains that the constant turn-rate target acceleration model exhibits equal or better performance over the full

8

operational range of the tracker against anticipated targets compared to any other model yet developed. Additionally, since it has been demonstrated that use of the constant turn-rate target acceleration model provides better than adequate performance (as well as equal of better performance as noted earlier), any multiple-filter algorithm would merely complicate and add an additional computational burden to the overall system without substantial performance benefit. Such an algorithm was considered for this effort and consisted of simultaneously optically processing both the first-order Gauss-Markov target acceleration model and the constant turn-rate target acceleration model in parallel. Both dynamics models used the output from an enhanced correlator as the measurement update. The appropriate dynamics model was selected by considering the range and range-rate data from the previous and current measurement frames to determine the switchover point. However, this concept was rejected due to the analysis outlined.

The method by which the proposed combination is implemented is heavily dependent on the use of optics and optical processors. Not only are the Kalman filter update and propagation cycle linear algebra operations accomplished within the bounds of an optical processing architecture, but the input signal is also passed through a previously developed (23) optical processor in order to provide the cross-correlations necessary for centroid offset calculations at the FLIR plane. Use of this technique thus allows for a potentially significant increase in system processing bandwidth if the FLIR array sensor is replaced by a real-time sensor, thereby providing performance potential far exceeding that obtainable with the FLIR. This issue is potentially more significant than any other possible filter modifications and will be discussed further in Chapter V.

To develop this admittedly very general overall description of system operation into the solution of the problem

```
                    ┌─────────────────────┐
                    │  Model Development  │
                    └─────────────────────┘
                               │
                               ▼
           ┌───────────────────────────────────┐
           │      Transfer of Model to an      │
           │   Optically-Implementable Form    │
           └───────────────────────────────────┘
                               │
                               ▼
              ┌──────────────────────────┐
              │      Optics Design       │
              └──────────────────────────┘
                               │
                               ▼
              ┌──────────────────────────┐
              │     System Analyses      │- - - - - - - - - - - ┐
              └──────────────────────────┘                      │
                               │                                ▼
                               │              ┌───────────────────────────────┐
                               │              │    Construction of Optics     │
                               │              │      Breadboard System        │
                               │              └───────────────────────────────┘
                               │                              │
                               │                              ▼
                               │              ┌───────────────────────────────┐
                               │              │     Optics Breadboard         │
                               │              │     System Analysis           │
                               │              └───────────────────────────────┘
                               │                              │
                               ▼                              │
              ┌──────────────────────────┐                    │
              │    Thesis Generation     │◀ - - - - - - - - - ┘
              └──────────────────────────┘
```
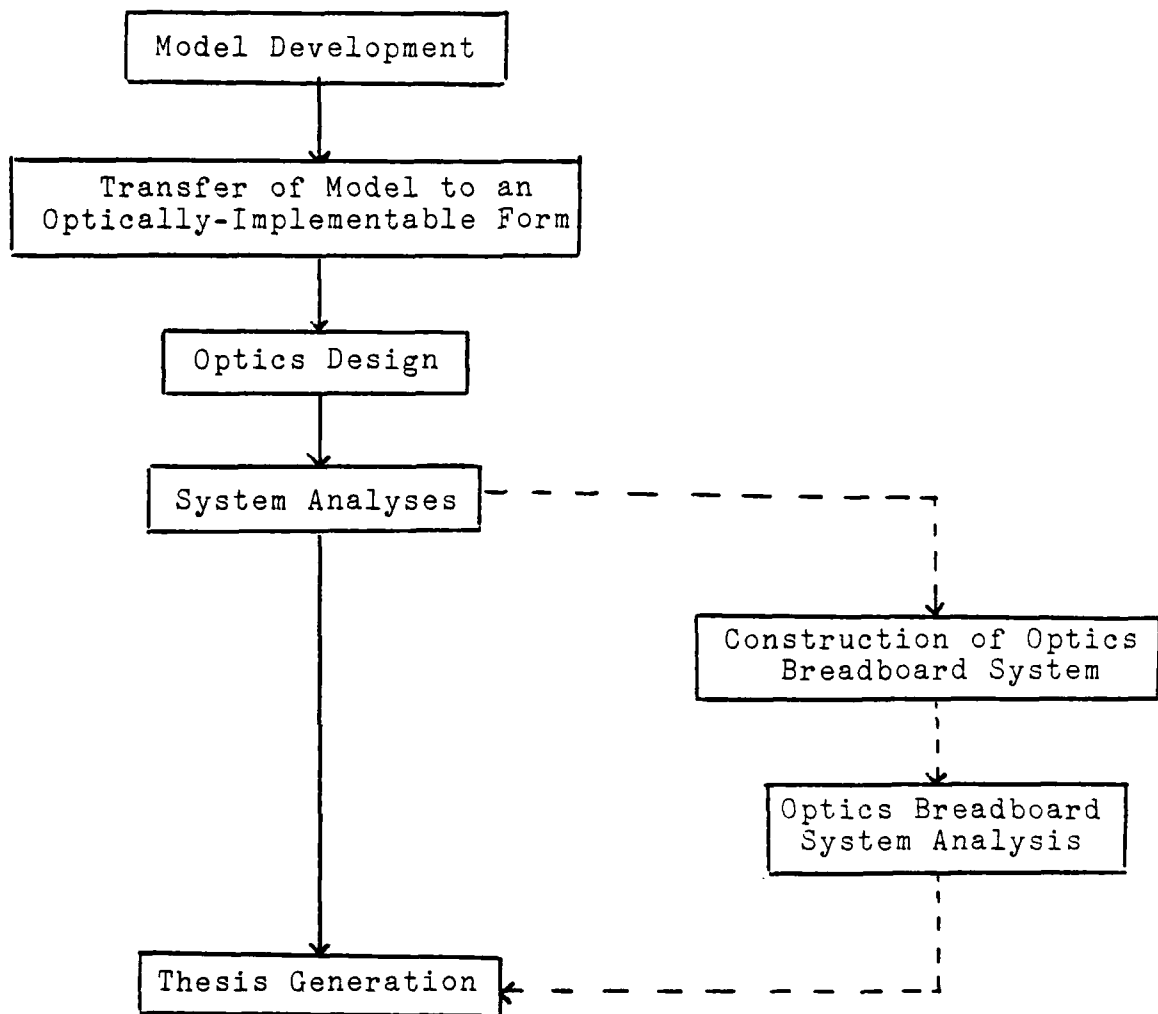
Figure 1 - Research Plan of Attack

outlined in section 1.3, a well-defined research plan of attack must be developed. The remaining paragraphs of this section describe the plan of attack for this research illustrated in Figure 1.

As both the dynamics and the measurement update models for the proposed solution have already been developed, the initial task of this thesis will be to determine the designs of the two optical processors, one to perform the correlations and one to implement the filter. These designs, as noted previously, will be constrained to the real world through limitations as to component choices.

It is extremely important at this point to differentiate carefully between the two optical processors involved. This is particularly true (as will be seen in Chapters III and V) since each processor performs unique tasks unrelated to the other and thus must be designed to different specifications. For these reasons, the optical processor which produces the necessary input cross-correlations will be termed the enhanced optical correlator (EOC), whereas the optical processor which performs the filter operations will be termed the optical Kalman filter (OKF).

As the design of the correlation processor has already been established (23) and will be discussed in Chapter III, criteria for the design of the OKF must be discussed. Here, choice of the optical architecture to be used is dependent on three key parameters: (1) the efficiency with which it accomplishes the linear algebra required for Kalman filter operations; (2) its ability to perform the required processing without decreasing system dynamic range (i.e., adding noise to the system as outlined further in Chapter V); and (3), its potential for increasing the system throughput rate. Combining these requirements with the knowledge that any optical architecture is limited by the performance of the modulator, a system tradeoff analysis based upon the available architectures can be performed.

11

This tradeoff analysis immediately limits the number of architectures available for the OKF. This is due to several facts. First, since any two-dimensional modulator-based optical architecture (designed for linear algebra) is limited to a maximum system bandwidth of 30 Hz for processing at the full dynamic range of the modulator (4,10,23), these architectures are not suitable candidates due to requirement (3). Secondly, electro-optic modulator-based optical architectures can also be discounted due to their presently limited dynamic range (30). This leaves only those optical architectures based on acousto-optic modulators as suitable candidates.

Although architectures based on acousto-optic modulators can be either one- or two-dimensional, all of the available two-dimensional architectures require integrating detectors (1) and thus do not satisfy the final requirement established. This leaves only two optical architectures, both based on single acousto-optic modulators, as candidates for the OKF. These are the (4) engagement array architecture (a pseudo-parallel structure) and the (2) pipelined iterative optical systolic array architecture (a true parallel structure). Of these two, the iterative nature of the pipelined iterative optical systolic array (as fully developed in Chapter V) proved far superior in satisfaction of the efficiency requirement as it could accomplish every operation required without major restructuring. It is for these reasons that the pipelined iterative optical systolic array architecture is the solution of choice for the OKF.

Now that these steps have been accomplished, the optical architecture for each processor must be analyzed so as to take full advantage of the optical processing benefits. This phase will thus require determination of the required system bandwidths, choice of all the specific optical components to be used, and analysis of any constraints and the methods by which they are overcome.

The above steps, having been successfully cc
will then allow the final design of each optical
and computation of each processor's modulation tr
function (MTF). The MTF, being analagous to an i
response in the electronic domain, will not only
system simulation and performance analyses from i
output, but will also conclusively demonstrate th
the optical architectures will not require retuni
filter due to additional noise.

If time had permitted, construction of a lim
width breadboard version of each optical processo
have then been accomplished. Characterization of
response characteristics as compared to their pre
could have been scaled upward and compared with t
dicted system performances obtained earlier for t
scale designs. Correlation, identification, and
of observed deficiencies in either comparison, if
would have been reincorporated into the package.

The final step of the research will be to dr
sions pertinent to the proposed optical implement,
the algorithm and to indicate areas of developmen
the potential to produce useful system refinement
that component selection will be limited to curre:
able hardware, optimizations in this area may pro
icant results. These results due to hardware dev
may then impact the analysis within this thesis,
significantly. Furthermore, recommendations as t
optical implementations of the developed architec
may also hold vast potential.

The overall approach as outlined was selecte
provide as much benfit as possible to both the re
and the sponsoring organization in the five man-m
were available for task completion. It is hoped
effort will be a cornerstone for future system de

13

II. Truth Model Descriptions

2.1 Overview

The definition of a state-space truth model requires that the mathematical representation of any real world process embodied within its confines has the greatest degree of correlation with the physical reality of the real world process, given the bounds of a finite state-space. As such, it becomes the standard against which any proposed filter design is measured and thus mandates that the truth model be free of any biases favoring any particular reduced order filter design approach.

In this chapter, a truth model is developed for the tracking portion of the overall system for which the design goal is the portrayal of measured and true motion of a target acquired by a ground-based high-energy laser weapons system. The targets are further postulated to be either unmanned missiles or manned aircraft (single or multiple engine). To perform this task given the outlined constraints, the approach chosen (7,8,20,21,23) has been to project onto the two-dimensional FLIR image plane the true intensity function generated by a target in three-dimensional inertial space, translationally shifted to account for the phase distortion caused by the atmosphere. Other physical phenomena, such as signal degradation due to FLIR optics mirror jitter, which may impact adversely upon system performance in a mathematically strict sense, are assumed to be of negligible import compared to the FLIR image motion sources (due to the true target dynamics and the translational shift which accounts for the wavefront phase distortion by the atmosphere) and are therefore omitted in the formulation of the state-space dynamics. However, the simulated image that results from the described projection of the target's true intensity function onto the FLIR image plane is subjected to spatially correlated but temporally uncorrelated noise to account for

14

background and inherent FLIR noises (7). The corrupted image
simulation thus obtained is the measurement array, $\underline{z}(t_i)$, of
average pixel intensities (from an 8x8 pixel tracking window)
that would occur at the FLIR image plane, and is the measure-
ment basis used by the enhanced correlator of the filter.

In its original development, the approach chosen to gen-
erate the continuous time target model used the stochastic
form of state-space differential equations in order to account
both for the statistical properties of the atmospheric cor-
ruption and the uncertainty due to the motion sources assumed
to be negligible enough not to warrant explicit modeling.
However, the equations were developed in augmented form so
that the states representing the true target dynamics could
be mathematically manipulated so as to allow for deterministic,
as well as stochastic, inputs without affecting the statistical
properties of atmospheric propagation. The approach thus
allows truth model generation of deterministic target trajec-
tories which, being subject to all of the corruptive (and
statistical) processes described earlier, can then be used to
analyze the performance of any proposed filter design approach.

To present this particular approach to the design of the
truth model in a logical manner, this chapter is divided into
a series of mathematical descriptions which originate at the
true dynamics of a single hot spot target and progress in a
temporal sense to the resultant FLIR image plane measurement
array used as the input data to the proposed filter design.
Extensions for the case of a multiple hot spot target are
presented after complete development of the single hot spot
target case. The truth model thus developed can be directly
appended to any proposed filter model design.

2.2 True Target Centroid Dynamics Model

The projection of any three-dimensional process onto a
two-dimensional measurement plane requires an exact singular-
ity-free mathematical conversion between the two coordinate

systems in order to be able to describe the set of all three-dimensional processes in terms of the two-dimensional coordinate system. Since this condition is fulfilled within the development of this truth model, description of the true target dynamics centroid model is accomplished by mathematically specifying the four deterministic target test trajectories in a three-dimensional inertial space (x_I, y_I, and z_I) having its origin at the tracker. This procedure allows specification of the conversion between the two coordinate spaces to be developed at a more logical point in the overall truth model development.

Since specific target trajectories must be developed not only to illustrate the proposed filter's tracking performance under the full range of conditions anticipated to be encountered but also to establish their baseline performance, Trajectory 1 is defined as a simple target traversal parallel to the x_I-y_I plane and is depicted in Figure 2. Defining the
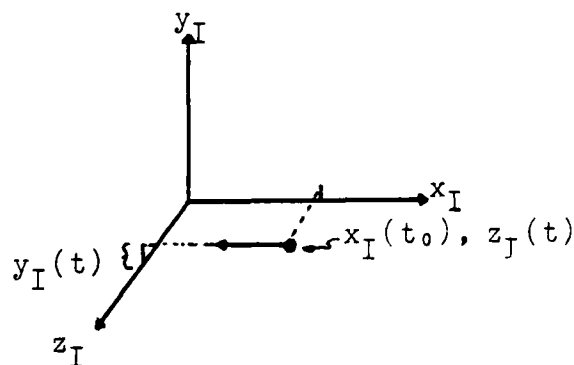
Figure 2 - Trajectory 1 Geometry

inertial target position as

$$x_I(t_0) = 5.0 \text{ km} \tag{2-1}$$
$$y_I(t_0) = 0.5 \text{ km} \tag{2-2}$$
$$\text{and } z_I(t_0) = 20 \text{ km} \tag{2-3}$$

the trajectory throughout the five second simulation is specified as

$$\dot{x}_I(t) = -1 \text{ km/sec} \tag{2-4}$$
$$\text{and } \dot{y}_I(t) = \dot{z}_I(t) = 0 \tag{2-5}$$

16

Additionally, the model for Trajectory 1 includes the capability of performing the traversal described with target roll rates of 0, 0.5, and 1 radian per second. This provision of the model allows inclusion of the change in the FLIR-depicted target shape as a function of the target profile as described in Section 2.5, and thus permits a realistic baseline to be established.

Alternatively, the definitions of Trajectories 2 and 3 represent the desire to establish a proposed filter's tracking performance against the most extreme maneuvers which any potential target can perform. Trajectory 2, depicted in Figure 3, thus portrays a target which, after 2.0 seconds of Trajectory 1 motion, performs either a constant 2g (ω_p = 19.6 milliradians per second) or 5g (ω_p = 49 milliradians per second) pull-up maneuver over two inertial dimensions (a plane in inertial space) ending at six seconds into the simu-
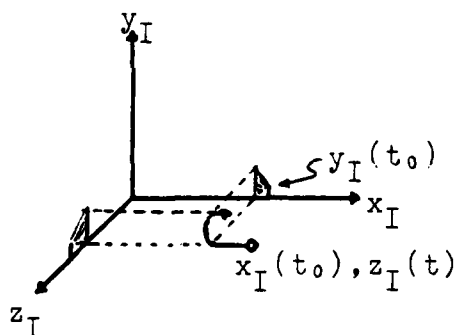
Figure 3 - Trajectory 2 Geometry

lation. Since the maneuver start time is at 2.0 seconds after Trajectory 2 initiation, including the results due to Trajectory 1 motion for the first two seconds yields the mathematical definitions of Trajectory 2 after initiation of the maneuver as

$$\dot{x}_I(t) = -\cos[\omega_p(t-2)] \text{ km/sec} \qquad (2-6)$$

$$\dot{y}_I(t) = \sin[\omega_p(t-2)] \text{ km/sec} \qquad (2-7)$$

$$\text{and } \dot{z}_I(t) = 0 \qquad (2-8)$$

Simple integration then yields the post maneuver target location as (based on the target's initial inertial coordinates as defined by Trajectory 1)

$$x_I(t) = 5 - 2 - \{\sin[\omega_p(t-2)] \ / \ \omega_p\} \text{ km} \qquad (2-9)$$

$$y_I(t) = 0.5 + (\{1 - \cos[\omega_p(t-2)]\} \ / \ \omega_p) \text{ km} \qquad (2-10)$$

$$z_I(t) = 20 \text{ km} \qquad (2-11)$$

An alternative form of Trajectory 2 is defined to portray target motion into the negative inertial z-direction (resulting in the target turning in toward the tracker) instead of the inertial y-direction. Performance of this trajectory redefines the y_I and z_I equations above as

$$\dot{y}_I(t) = 0 \qquad (2-12)$$

$$y_I(t) = 0.5 \text{ km} \qquad (2-13)$$

$$\dot{z}_I(t) = -\sin[\omega_p(t-2)] \text{ km/sec} \qquad (2-14)$$

$$z_I(t) = 20 - (\{1 - \cos[\omega_p(t-2)]\} \ / \ \omega_p) \text{ km} \qquad (2-15)$$

with all variables as defined earlier. Use of this modification enables the projection of three distinct ellipsoidal target intensity patterns onto the FLIR image plane so that target shape effects (to be discussed) can be included in the simulation.

Noting that both Trajectory 2 descriptions simulate the trajectory path change as a step function, it can be concluded that any proposed filter is required to track a far harsher environment than a real situation where ω_p would build up smoothly (in a continuous sense) from zero to its specified terminal value. Satisfaction of filter performance specifications will therefore ensure better than minimal performance against actual targets.

The next test trajectory incorporated in the analysis, Trajectory 3, is specifically designed to evaluate the performance of a proposed filter design against targets both initiating and terminating a maneuver. Implementation of this trajectory can be considered as an extension of

18

Trajectory 2 in that 2g and 5g pull-up maneuvers are initiated
and terminated as step functions at 2.0 and 3.5 seconds, re-
spectively. The target has the same initial position and
inertial velocity descriptions as Trajectory 2 until maneuver
termination. At t = 3.5 seconds, the target continues at the
inertial velocities (determined by use of the Trajectory 2
equations)

$$\dot{x}_I(t \geq 3.5) = -.99958 \text{ km/sec} \qquad (2\text{-}16)$$

$$\dot{y}_I(t \geq 3.5) = .029069 \text{ km/sec} \qquad (2\text{-}17)$$

$$\dot{z}_I(t \geq 3.5) = 0 \qquad (2\text{-}18)$$

for the remainder of the simulation.

The final test case, Trajectory 4, represents the por-
trayal of target trajectory changes simultaneously in all
three inertial dimensions, rather than maintaining at least
one inertial dimension constant as in all of the previous
trajectory descriptions. Use of this test trajectory thus
also enables evaluation of filter performance against targets
whose intensity pattern is continuously changing over all
three inertial dimensions, which is a more realistic por-
trayal of the projected (assumed) ellipsoidal intensity
patterns than that afforded by the alternate form of Tra-
jectory 2.

Trajectory 4 is implemented by simulating a target
which, after establishment of the baseline as defined for
Trajectory 2, performs a 2g pull-up maneuver which mathe-
matically establishes a new three-dimensional coordinate
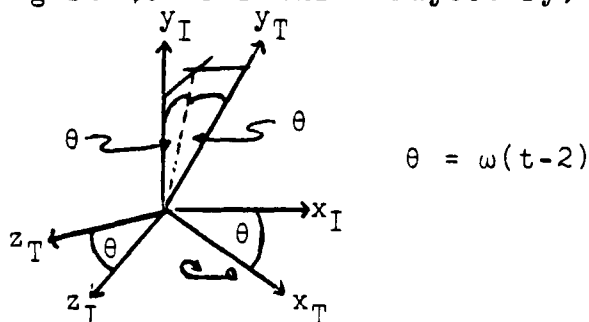system as depicted in Figure 4. For this trajectory, the

$$\theta = \omega(t\text{-}2)$$

Figure 4 - Trajectory 4 In- and Out-of-Plane Coordinate
Transformation Geometry

translated coordinate system (x_T, y_T, and z_T) rotates at the
constant rate ω_p about both the x_I and z_I coordinate axes.
The relationship between the two coordinate systems can thus
be easily established by analyzing the velocity vector rela-
tionships for each of the two two-dimensional case (the x_I-y_I
plane and the y_I-z_I plane) and combining the results vec-
torially. For the trajectory as defined, the coordinate
transformations due to the x_T-y_T plane target motion are

$$\dot{x}_I(t>2) = \cos[\omega_p(t-2)]\dot{x}_T(t) + \sin[\omega_p(t-2)]\dot{y}_T(t) \qquad (2\text{-}19)$$
$$\dot{y}_I(t>2) = -\sin[\omega_p(t-2)]\dot{x}_T(t) + \cos[\omega_p(t-2)]\dot{y}_T(t) \qquad (2\text{-}20)$$
$$\dot{z}_I(t>2) = \dot{z}_T(t) \qquad (2\text{-}21)$$

where all velocity variables are expressed in km/sec. For
the out-of-plane coordinate case depicted in Figure 4, the
coordinate transformations due to the y_T-z_T plane target
motion are

$$\dot{x}_I(t>2) = \dot{x}_T(t) \qquad (2\text{-}22)$$
$$\dot{y}_I(t>2) = \cos[\omega_p(t-2)]\dot{y}_T(t) + \sin[\omega_p(t-2)]\dot{z}_T(t) \qquad (2\text{-}23)$$
$$\dot{z}_I(t>2) = -\sin[\omega_p(t-2)]\dot{y}_T(t) + \cos[\omega_p(t-2)]\dot{z}_T(t) \qquad (2\text{-}24)$$

where the velocity variable units are defined similarly as
in the earlier case. Expressing these coordinate transfor-
mations in matrix form and combining them with the initial
velocity vector specified earlier (from Trajectory 2) yields
the overall coordinate transformation vector after maneuver
initiation as

$$
\begin{bmatrix} \dot{x}_I(t) \\ \dot{y}_I(t) \\ \dot{z}_I(t) \end{bmatrix} =
\begin{bmatrix} 1 & 0 & 0 \\ 0 & \cos\theta & \sin\theta \\ 0 & -\sin\theta & \cos\theta \end{bmatrix}
\begin{bmatrix} \cos\theta & \sin\theta & 0 \\ -\sin\theta & \cos\theta & 0 \\ 0 & 0 & 1 \end{bmatrix}
\begin{bmatrix} -1 \text{ km/sec} \\ 0 \\ 0 \end{bmatrix}
$$

$$
= \begin{bmatrix} -\cos[\omega_p(t-2)] & & \text{km/sec} \\ \cos[\omega_p(t-2)]\sin[\omega_p(t-2)] & \text{km/sec} \\ -\sin^2[\omega_p(t-2)] & & \text{km/sec} \end{bmatrix} \qquad (2\text{-}25)
$$

where θ is defined in Figure 4. Simple integration of the
overall coordinate transformation then yields (in km)

$$x_I(t>2) = 5 - 2 - \sin[\omega_p(t-2)]/\omega \qquad (2\text{-}26)$$

$$y_I(t>2) = 0.5 + \sin^2[\omega_p(t-2)]/2\omega \qquad (2\text{-}27)$$

$$z_I(t>2) = 20 - (t-2)/2 + \sin[2\omega_p(t-2)]/4\omega \qquad (2\text{-}28)$$

Finally, definition of the inertial coordinate relationships allows the out-of-(inertial)plane angle (OPA) of the maneuver described by the translating plane to be easily generated from the relationship (as seen in Figure 4)

$$OPA = \tan^{-1} z_I(t)/y_I(t) \qquad (2\text{-}29)$$

for all time after maneuver initiation.

With the true target centroid dynamics described in inertial space, the apparent FLIR image plane motion must be transformed to the inertial motion descriptions. Although this transformation can be accomplished within several different formats, the previously developed singularity-free mathematical conversion defines the inertial space to FLIR image plane geometrical relationship as depicted in Figures 5 and 6, where the inertial coordinates are as defined earlier, $r_H(t)$ represents the horizontal tracker to target range, and $r(t)$ represents the tracker to target slant range.
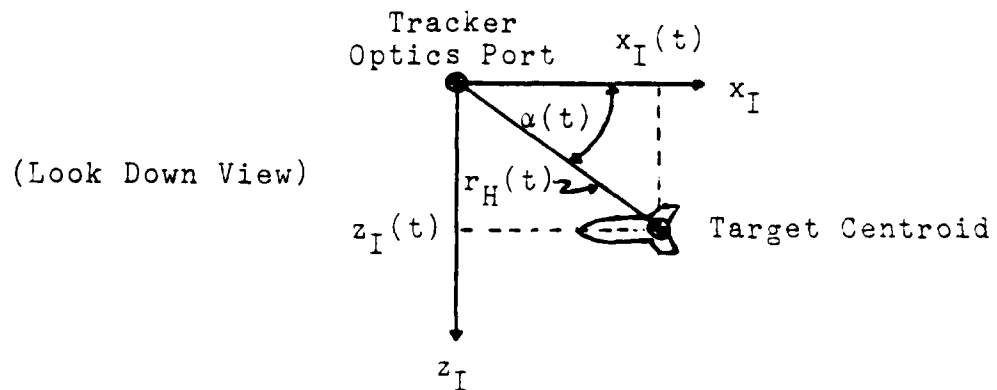
Figure 5 - Horizontal Inertial Space/FLIR Image Plane Geometrical Relationship

It is apparent from the figures that defining the tracker's optics port as the inertial origin of coordinates results in a tremendously simplified geometry for hemispheric tracking while insuring the singularity-free conversion required for the analysis.

21
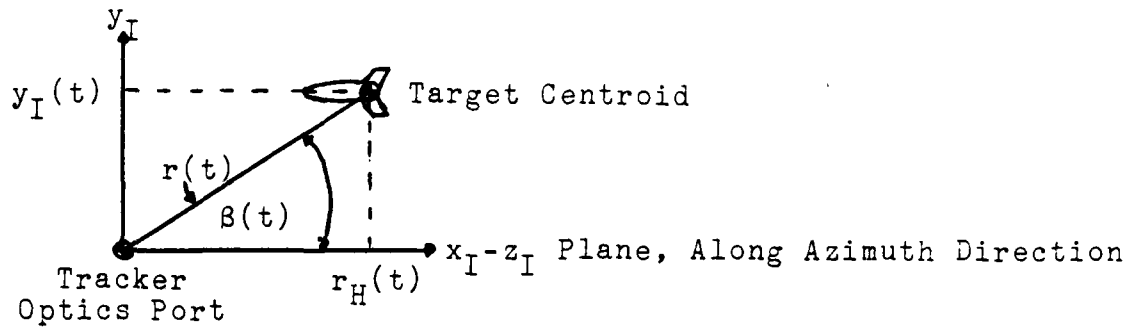
Figure 6 - Vertical Inertial Space/FLIR Image Plane
Geometrical Relationship

The governing correlation equations are generated from
the appropriate figure. Thus, in the horizontal direction,

$$\alpha(t) = \tan^{-1} \left[z_I(t)/x_i(t) \right] \text{ rad} \qquad (2\text{-}30)$$

yielding upon differentiation

$$\dot{\alpha}(t) = \frac{x_I(t)\dot{z}_I(t) - z_I(t)\dot{x}_I(t)}{x_I{}^2(t) + z_I{}^2(t)} \text{ rad/sec} \qquad (2\text{-}31)$$

where Equation (2-31) can be converted into pixels per second
by using the pixel/field of view relationship of 20 microra-
dians per pixel. Similarly, in the vertical direction,
Figure 6 yields the equation

$$\beta(t) = \left[y_I(t)/r_H(t) \right] \text{ rad} \qquad (2\text{-}32)$$

where $r_H(t) = \left[x_I{}^2(t) + z_I{}^2(t) \right]^{\frac{1}{2}}$ as defined in Figure 5.
Differentiation thus yields

$$
\begin{aligned}
\dot{\beta}(t) &= \frac{r_H(t)\dot{y}_I(t) - y_I(t)\dot{r}_H(t)}{r_H{}^2(t) + y_I{}^2(t)} \\
&= \frac{r_H(t)\dot{y}_I(t) - y_I(t)\dot{r}_H(t)}{r^2(t)} \text{ rad/sec}
\end{aligned}
\qquad (2\text{-}33)
$$

where $\dot{\beta}(t)$ can also be expressed in pixels per second through
use of the same relationship as defined for the horizontal

22

direction. These equations coupled with the deterministic target trajectories (or a target trajectory expressed in stochastic form, as will be discussed in Section 2.3) thus fully define the true target centroid dynamics model as projected onto the FLIR image plane. Furthermore, definition of the FLIR horizontal and vertical axes in this manner tremendously simplifies formulation of the FLIR image plane target dynamics model which accounts both for the target motion and the translational shift due to atmospheric phase distortion. Therefore, discussion of the FLIR image plane target dynamics model is the next logical link in the model chain.

2.3 FLIR Image Plane Target Dynamics Model

With both the inertial coordinates and the deterministic target trajectories defined, the model must account for the target dynamics as perceived by the FLIR image plane. The approach chosen has been to generate equations which represent the motion due to the target dynamics in terms of the FLIR image plane coordinate axes as defined above (whose states are subscripted with D for dynamics) to which are augmented atmospheric states (subscripted A) to account for the translational shift along both axes due to the atmospheric jitter phenomenom.

The continuous-time FLIR image plane target dynamics model thus incorporates two dynamics states to represent the true location of the target centroid on the two-dimensional FLIR image plane. As defined earlier, these states are defined as $\alpha(t)$, the perceived FLIR image azimuth (horizontal position), and $\beta(t)$, the perceived FLIR image elevation. Putting these defined state variables in linear differential equation form yields

$$\underline{\dot{x}}_D(t) = \underline{F}_D(t)\underline{x}_D(t) + \underline{B}_D(t)\underline{u}_D(t) + \underline{G}_D(t)\underline{w}_D(t) \qquad (2\text{-}34)$$

where

23

$$\underline{\dot{x}}_D(t) \equiv [\dot{\alpha}(t) \quad \dot{\beta}(t)]^T$$

$\dot{\alpha}(t) \equiv$ apparent horizontal target velocity (azimuth rate of change) on the FLIR image plane

$\dot{\beta}(t) \equiv$ apparent vertical target velocity (elevation rate of change) on the FLIR image plane

$\underline{F}_D(t) \equiv$ the 2x2 state distribution matrix

$\underline{x}_D(t) \equiv [\alpha(t) \quad \beta(t)]^T$ with $\alpha(t)$ and $\beta(t)$ as defined above

$\underline{B}_D(t) \equiv$ the 2x2 control input distribution matrix

$\underline{u}_D(t) \equiv$ the two-dimensional vector of system control inputs

$\underline{G}_D(t) \equiv$ the 2x2 dynamics driving noise distribution matrix

and $\underline{w}_D(t) \equiv$ the two-dimensional dynamics driving noise vector assumed to be independent white noise of mean zero and strength $\underline{Q}_D(t)$; i.e.,
$$E\{\underline{w}_D(t)\underline{w}_D^T(t+\tau)\} = \underline{Q}_D(t)\delta(\tau)$$

The nonlinear form of the continuous-time FLIR image plane target dynamics model is defined to be

$$\underline{\dot{x}}_D(t) = \underline{f}[\underline{x}_D(t), \underline{u}_D(t), t] + \underline{G}_D(t)\underline{w}_D(t) \qquad (2\text{-}35)$$

where

$\underline{f}[\underline{x}_D(t), \underline{u}_D(t), t] \equiv$ the two-dimensional vector composed of possibly nonlinear functions of $\underline{x}_D(t)$, $\underline{u}_D(t)$, and t which represents the state description of target motion driven by the inputs over time

is the only other definition required. Definition of the stochastic state-space differential equations in this manner therefore allows the generation of the true target trajectories that are dictated by test requirements and outlined in Section 2.2. This deterministic form is accomplished by using the linear form Equation (2-34) while defining

24

$$\underline{F}_D(t) = \underline{0}$$
$$\underline{B}_D(t) = \underline{I}$$
$$\text{and } \underline{G}_D(t) = \underline{0}$$

thereby allowing truth model generation of specific time histories of $\alpha(t)$ and $\beta(t)$ as a function only of the deterministic inputs, but in the stochastic differential equation format by developing the appropriate $\alpha(t)$ and $\beta(t)$ to yield these time histories via integration. It is important to note, however, that redefinition of $\underline{F}_D(t)$ and $\underline{G}_D(t)$ to allow nonzero entries permits incorporation of either a mixed deterministic/stochastic form (for only one FLIR axis affected) or a fully stochastic form of Equation (2-34) into the truth model trajectory description. This capability can be used, for example, to simulate jinking or turbulence effects on top of a purposeful (deterministic) trajectory.

Equations (2-34) and (2-35) are then augmented by expressions which represent the apparent target motion and statistics which are due to the atmospheric wavefront phase distortion. These atmospheric disturbances, as developed previously (7), are modeled as a third-order Gauss-Markov process which is describable as the output of a shaping filter with a frequency domain transfer function of

$$\frac{\alpha_A}{w_3} = \frac{K(14.14)(659.5)^2}{(s+14.14)(s+659.5)^2} \qquad (2-36)$$

driven by a unit strength white gaussian noise w_3. A duplicate independent model is also used to generate β_A in the vertical FLIR image plane direction. The form of the stochastic differential equation used to represent the atmospheric jitter thus becomes

$$\underline{\dot{x}}_A(t) = \underline{F}_A(t)\underline{x}_A(t) + \underline{G}_A(t)\underline{w}_A(t) \qquad (2-37)$$

where

$\underline{\dot{x}}_A(t) \equiv$ vector of the six atmospheric noise state
derivatives

$\underline{F}_A(t) \equiv$ atmospheric plant matrix

$\underline{G}_A(t) \equiv$ atmospheric noise uncertainty distribution matrix

and $\underline{w}_A(t) \equiv$ two-dimensional vector of white Gaussian noise
inputs with statistics: $E\{\underline{w}_A(t)\} = \underline{0}$ and
$E\{\underline{w}_A(t)\underline{w}_A^T(t+\tau)\} = \underline{Q}_A(t)\delta(\tau)$

After augmenting the atmospheric states to the dynamics states,
the discretized solution to the truth model propagation (7)
for the motion of the target centroid as perceived by the
FLIR image plane (using a deterministic model for true cen-
troid motion) becomes

$$\underline{x}(t_{i+1}) = \underline{\Phi}(t_{i+1},t_i)\underline{x}(t_i) + \left[\frac{\underline{B}_d(t_i)}{\underline{0}}\right]\underline{u}_d(t_i) + \left[\frac{\underline{0}}{\underline{Q}_{Ad}}\right] \quad (2\text{-}38)$$

where

$\underline{x}(t_i) \equiv$ state vector of the two dynamics states and the six
atmospheric states

$$\underline{\Phi} \equiv \left[\begin{array}{c|c} \underline{\Phi}_D(t_{i+1},t_i) & \underline{0} \\ \hline \underline{0} & \underline{\Phi}_A(t_{i+1},t_i) \end{array}\right]$$

$$= \left[\begin{array}{c|c} \exp \underline{F}_D\Delta t & \underline{0} \\ \hline \underline{0} & \exp \underline{F}_A\Delta t \end{array}\right] \quad \Delta t = t_{i+1} - t_i$$

since both $\underline{F}_D$ and $\underline{F}_A$ are time invariant for this
problem

$\underline{B}_d(t_i) \equiv$ input matrix for dynamics
$\int_{t_{i+1}}^{t_i} \underline{\Phi}(t_{i+1},t_i)\underline{B}(\tau)d\tau$

$\underline{u}_d(t_i) \equiv$ piecewise constant function (between sample times)
evaluated at the midpoint of the interval as an
approximation to the integral of $\dot{\alpha}(t)$ and $\dot{\beta}(t)$
from t_i to t_{i+1}

$$= \left[\begin{array}{c} \dot{\alpha}(t_i + \Delta t/2) \\ \dot{\beta}(t_i + \Delta t/2) \end{array}\right]$$

$\underline{w}_{Ad}(t_i) \equiv$ zero mean discrete-time white Gaussia.
statistics: $E\{\underline{w}_{Ad}(t_i)\underline{w}_{Ad}^T(t_j)\} = \underline{I}\delta_{ij}$

$\underline{Q}_{Ad}(t_i) = \sqrt{\underline{Q}_{Ad}(t_i)}\ \sqrt{\underline{Q}_{Ad}(t_i)}^T$

$\qquad = \{\int_{t_{i+1}}^{t_i} \underline{\Phi}_A(t_{i+1},\tau)\underline{G}_A(\tau)\underline{Q}_A(\tau)\underline{G}_A^T($

$E\{\sqrt{\underline{Q}_{Ad}(t_i)}\ \underline{w}_{Ad}(t_i)\} = \underline{0}$

$E\{\sqrt{\underline{Q}_{Ad}(t_i)}\ \underline{w}_{Ad}(t_i)\underline{w}_{Ad}^T(t_j)\sqrt{\underline{Q}_{Ad}(t_j)}^T$

where $\sqrt{\underline{Q}_{Ad}}$ is the Cholesky square r:
sition of $\underline{Q}_{Ad}$ (15)

and the apparent target centroid is located at (
$[\beta_D(t_i)+\beta_A(t_i)]$). Explicitly, the state transit:
$[\underline{\Phi}(t_{i+1},t_i)$ from Equation (2-38)] is

$$
\begin{bmatrix}
1 & 0 & 0 & 0 & 0 & 0 \\
0 & 1 & 0 & 0 & 0 & 0 \\
0 & 0 & e^{-p_1\Delta t} & 0 & 0 & 0 \\
0 & 0 & 0 & e^{-p_2\Delta t} & \Delta t e^{-p_2\Delta t} & 0 \\
0 & 0 & 0 & 0 & e^{-p_2\Delta t} & 0 \\
0 & 0 & 0 & 0 & 0 & e^{-p_1\Delta t} \\
0 & 0 & 0 & 0 & 0 & 0 \\
0 & 0 & 0 & 0 & 0 & 0 \\
\end{bmatrix}
$$

where the lower two 3x3 submatrices in $\underline{\Phi}(t_{i+1},t_i)$
and propagate the atmospheric disturbances in the
and elevation directions with the single pole (re
p_1 above) and double pole (p_2 above) as defined i
(2-36). Finally for the purposes of this truth n
is defined to be

$$
\begin{bmatrix}
\Delta t & 0 \\
0 & \Delta t \\
0 & 0 \\
0 & 0 \\
0 & 0 \\
0 & 0 \\
0 & 0 \\
0 & 0 \\
\end{bmatrix}
$$

Definition of all factors as identified above thus allows truth model representation of the target dynamics on the FLIR image plane with all major factors affecting target motion included. However, as the actual FLIR image plane presentation consists of an IR intensity function distribution measurement rather than a focused image of the target centroid, the truth model must account for these additional factors inherent to the real world process. Definition of these factors in the FLIR image plane measurement model presented below thus completes the truth model for the single hot spot case, from which extensions can be made to define the truth model completely for the additional case of a multiple hot spot target.

2.4 FLIR Image Plane Measurement Model

In order to preserve the maximum degree of correlation between the truth model and the physical reality of the actual process within the bounds of a finite state-space, any mathematical distribution used to represent the IR image distribution on the FLIR image plane must approximate the actual measured pattern to a very high degree. Previous efforts (7,16,20) in this area have shown that a more than adequate relationship exists when the pattern due to distant targets is represented by a bivariate Gaussian function having circular equal intensity contours. Furthermore, it has been additionally established (7,20) that the only change required for representation of closer range targets is the geometry used to represent the equal intensity contours. For this case, an elliptical pattern maintains the desired correlation. These developments allow the perceived FLIR image plane intensity function for either case to be expressed as

$$I(\alpha,\beta) = I_{Max} \exp\{-\tfrac{1}{2}\left[(\alpha-\alpha_p)(\beta-\beta_p)\right]\left[\underline{P}^{-1}\right]\left[(\alpha-\alpha_p)(\beta-\beta_p)\right]^{T}\} \quad (2\text{-}39)$$

where the variables, as shown in Figure 7, are

$I_{Max} \equiv$ maximum target intensity

28

α_p, β_p ≡ coordinates of I_{Max} which correspond to the apparent target centroid location on the FLIR tracking window

σ_L, σ_S ≡ eigenvalues of $\underline{P}$ corresponding to the ellipse semimajor axis along the velocity vector and the ellipse semiminor axis perpendicular to the velocity vector, respectively, where l and s denote large and small (measured in pixels)

v_{pl} ≡ target velocity component perpendicular to the line of sight from the FLIR image plane to the target, which is defined to be conincident with the ellipse semimajor axis as depicted

and θ ≡ v_{pl}-FLIR plane orientation angle defined by the intensity pattern semimajor axis and the FLIR horizontal axis (α) translated to the apparent target centroid (α_p,β_p)
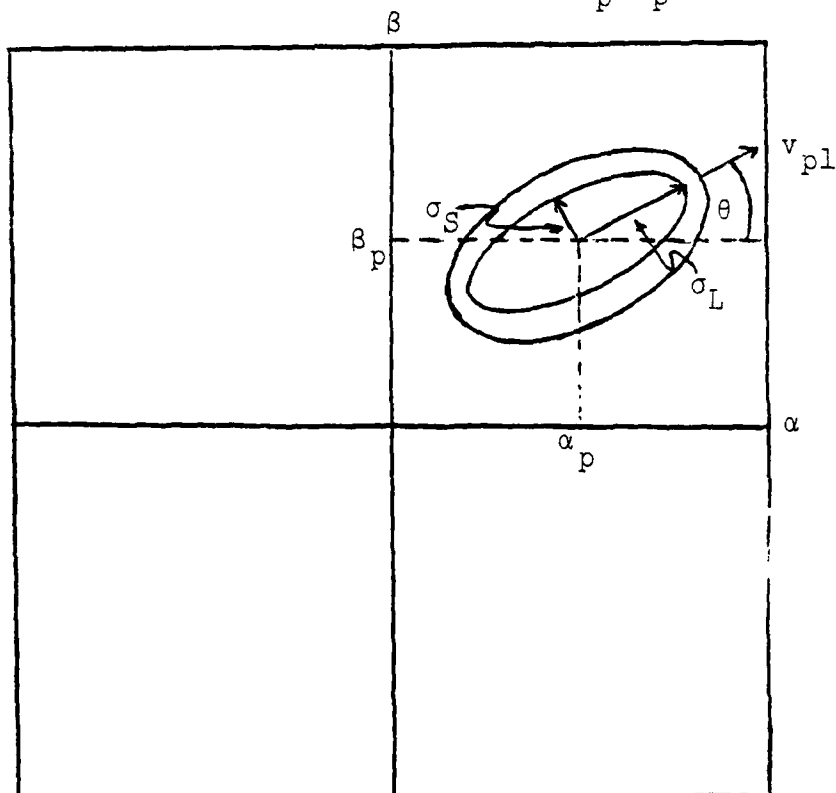

Figure 7 - Image Intensity Characteristics

29

Prior to any additional development, one additional factor must be considered. Recalling that each pixel of the 8x8 FLIR tracking array has a field of view (FOV) of 20x20 microradians, it is apparent that the small resultant total FOV is conducive to approximating the target angular displacement by the linear displacement of the target image centroid on the FLIR plane. It has also been demonstrated (7) that this relationship holds for the FLIR image plane velocity components as well. Since, as noted previously, all of the displacement and velocity FLIR plane components (α, $\dot{\alpha}$, β, and $\dot{\beta}$) are expressible in terms of angular or displacement units, an initial angular calculation is required to generate the angular displacement of the inertial target velocity (depicted in Figure 8) out of the FLIR image plane. The entire balance of the truth model target intensity pattern generation can then be accomplished using angular measurements.

The first step in this generation is thus to calculate the target velocity plane to FLIR image plane angle, γ. This computation is necessary to obtain the FLIR image plane velocity component perpendicular to the line of sight (v_{pl}), which is the projection of the inertial velocity (v) known from the simulation. From Equations (2-31) and (2-33), $\dot{\alpha}$ and $\dot{\beta}$, respectively, are generated in terms of radians per second. Since $r(t)$ is also defined by Equation (2-33), it is easy to see than an equivalent representation of FLIR image plane velocity translated to inertial space is

$$\dot{\alpha}'(t) = r(t)\dot{\alpha}(t) \text{ meters/second} \qquad (2\text{-}40\text{a})$$
$$\text{and } \dot{\beta}'(t) = r(t)\dot{\beta}(t) \text{ meters/second} \qquad (2\text{-}40\text{b})$$

where the prime superscript is used to indicate variables translated from the FLIR plane to the target and whose displacement variables are always expressed in meters instead of pixels. Since the inertial velocity is known to be

$$|v| = \left[\dot{x}_I^2(t) + \dot{y}_I^2(t) + \dot{z}_I^2(t)\right]^{\frac{1}{2}} \qquad (2\text{-}41)$$

30

and the FLIR image plane velocity (as depicted in Figure 8) is defined to be

$$|v_{pl}| = [\dot{\alpha}^2(t) + \dot{\beta}^2(t)]^{\frac{1}{2}} \qquad (2\text{-}42)$$

the target velocity plane to FLIR image plane angle γ is

$$\cos \gamma = r(t)|v_{pl}|/|v| \qquad (2\text{-}43)$$

The remainder of the angular relationships depicted in Figures 8 and 9 can now be developed. Specifically, these are

$$\cos \theta = \dot{\alpha}(t)/|v_{pl}| \qquad (2\text{-}44)$$
$$\sin \theta = \dot{\beta}(t)/|v_{pl}| \qquad (2\text{-}45)$$
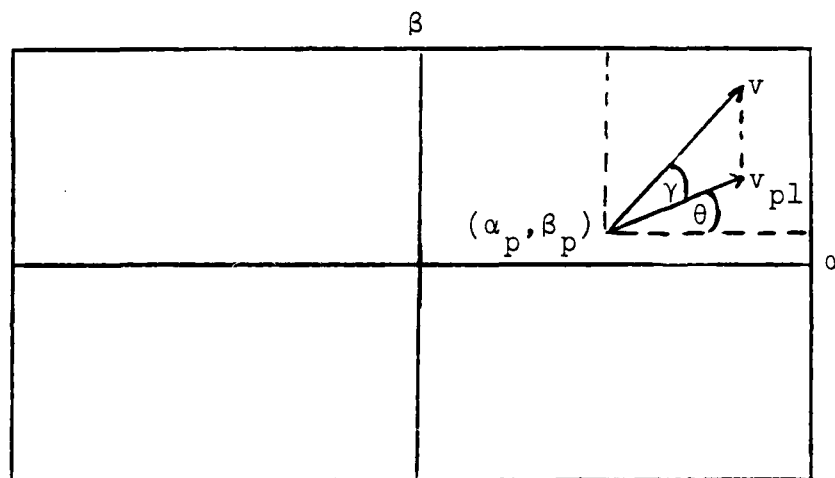
Figure 8 - Image Projection Relationships

With $\cos \gamma$ determined, the semimajor axis of a single hot spot target can be projected onto the FLIR image plane. For δ defined to be the length of the target in meters, the apparent length of the target to be measured by the FLIR plane is

$$\sigma_L' = \delta \cos \gamma \text{ meters} \qquad (2\text{-}46)$$

as depicted in Figure 9. Since, as noted previously, the fields of view are sufficiently small, the angle Ψ is

$$\Psi = \sigma_L'/r(t) \text{ radians} \qquad (2\text{-}47)$$

31
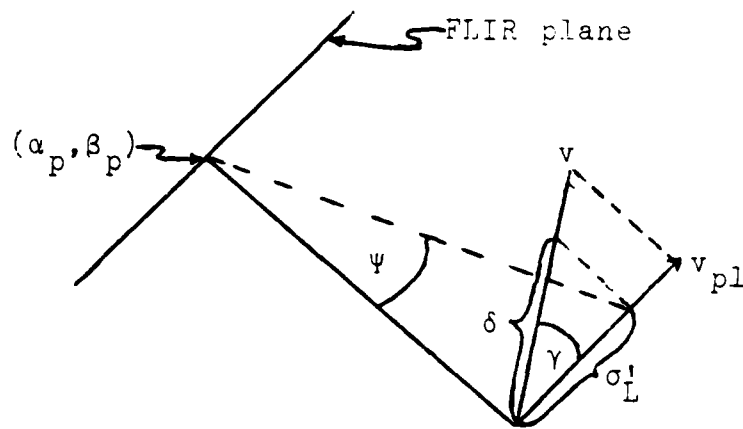
Figure 9 - Ellipse Semimajor Axis Projection Relationships

which then allows σ_L to be calculated as (with the appropriate pixel conversion factor)

$$\sigma_L = \Psi/20 \times 10^{-6} \text{ pixels} \qquad (2\text{-}48)$$

Similarly, the ellipse semiminor axis can be defined as

$$\sigma_S = \sigma_S'/r(20 \times 10^{-6}) \text{ pixels} \qquad (2\text{-}49)$$

where σ_S' is the target's IR cross-section.

In this analysis, an additional manipulation is incorporated to lessen computation time. Recalling that each trajectory as defined yields $\gamma=0$ at $t=0$, σ_L and σ_S immediately become

$$\sigma_L(0) = \delta/r(20 \times 10^{-6}) \quad \text{pixels} \qquad (2\text{-}50a)$$
$$\sigma_S(0) = \sigma_S'/r(20 \times 10^{-6}) \text{ pixels} \qquad (2\text{-}50b)$$

To preclude recalculation of all quantities at each analysis point, the simple ratios

$$\sigma_L(t) = (\cos \gamma)[\sigma_L(0)][r(0)]/r(t), \ t \neq 0 \qquad (2\text{-}51a)$$
$$\sigma_S(t) = [\sigma_S(0)][r(0)]/r(t) \qquad , \ t \neq 0 \qquad (2\text{-}51b)$$

are set up to calculate the ellipse semimajor and semiminor axis lengths efficiently. This then establishes all parameters required for the analysis.

The intensity at any point in the image plane can now be computed in the image ellipse principal axis coordinate system. Here, Equation (2-39) is redefined after the coordinate

32

change as

$$I(L,S) = I_{Max} \exp\{-\tfrac{1}{2}[\Delta L \ \Delta S] \begin{bmatrix} \sigma_L^2 & 0 \\ 0 & \sigma_S^2 \end{bmatrix}^{-1} \begin{bmatrix} \Delta L \\ \Delta S \end{bmatrix}\} \qquad (2\text{-}52)$$

where

$$\Delta L = (\alpha - \alpha_p)\cos\theta + (\beta - \beta_p)\sin\theta$$
$$\Delta S = (\beta - \beta_p)\cos\theta - (\alpha - \alpha_p)\sin\theta$$

and θ is as defined earlier. Since the average intensity for any pixel, as measured by the FLIR, is the integral of the apparent target intensity function over the pixel area, divided by the area of the pixel, and corrupted by FLIR and background noise, these effects must be included in the final expression.

To generate this final expression, it can be noted that previous work (7) has shown that the apparent target intensity function can be well approximated by averaging the intensity over 25 equally spaced points within each pixel. Additional work done at the same time documented the existence of spatial correlations of background noise in each data frame with nonnegligible spatial correlations between each pixel and its closest two neighboring pixels in each direction. Since this work also justified that any temporal correlations of these noises are negligible, only a single noise term (n_{lm}) need be incorporated into the expression for the average intensity in the pixel in the l-th row and m-th column of the 8x8 array. This expression now becomes

$$\bar{I}_{lm}(t_i) = \frac{1}{25} \sum_{k=1}^{5} \sum_{j=1}^{5} I_{Max} \exp\{-\tfrac{1}{2}[\Delta L_{ljk} \ \Delta S_{mjk}] \begin{bmatrix} \sigma_L^2 & 0 \\ 0 & \sigma_S^2 \end{bmatrix}^{-1} \begin{bmatrix} \Delta L_{ljk} \\ \Delta S_{mjk} \end{bmatrix}\}$$
$$+ \ n_{lm}(t_i) \qquad (2\text{-}53)$$

and represents the measurement array for a single hot spot target which is then input to the correlator/filter. For multiple hot spot targets, three Gaussian hot spots with elliptical constant intensity contours and parallel

33

semimajor axes were used in this study. The measurement thus becomes the summation of the apparent intensity functions due to each spot plus the noise term for each pixel. This development is fully outlined in the following section.

2.5 Projection of Multiple Hot Spots

For previous truth model calculations involving only single hot spot targets, the target center of mass (COM) was assumed conincident with the center of the intensity ellipsoid. Since the method for projecting the target intensity pattern is the same for both cases, a solution for the target COM for the multiple hot spot case can potentially be generated given the assumption that the angular orientation of any of the hot spots' principal axes is identical to the others. If the relationship of each ellipsoid center to the target COM is known in inertial coordinates as well, a simple transformation of these relationships into FLIR image plane coordinates will guarantee a solution.

Prior to defining these additional relationships for the thesis problem, it is necessary to set up the geometry properly for their use. As depicted in Figure 10, where all
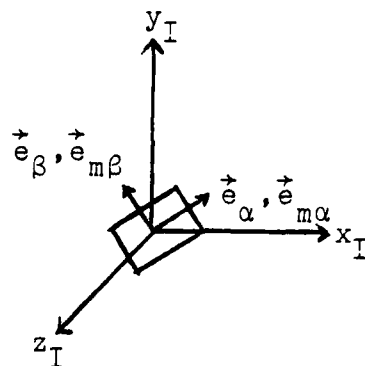
Figure 10 - Relation of the $\vec{e}_{m\alpha}$-$\vec{e}_{m\beta}$ Plane Unit Vectors to the FLIR Plane Unit Vectors

the coordinate frames are shown, the unit vectors $\vec{e}_{m\alpha}$ and $\vec{e}_{m\beta}$ are related to the FLIR plane unit vectors (for ease in implementing the required coordinate transformation) by the

34

expressions

$$\vec{e}_{m\alpha} = \vec{e}_{\alpha} \tag{2-54a}$$
$$\vec{e}_{m\beta} = \vec{e}_{\beta} \tag{2-54b}$$

where the subscript m is used to define FLIR plane translated variables. Figure 11 thus depicts the translation of the plane determined by $\vec{e}_{m\alpha}$ and $\vec{e}_{m\beta}$ in inertial space so that its origin is coincident with the target's COM. Since this new plane is parallel to the FLIR plane, any descriptions of target properties in terms of this "m" plane are easily relatable to FLIR plane variables as well.
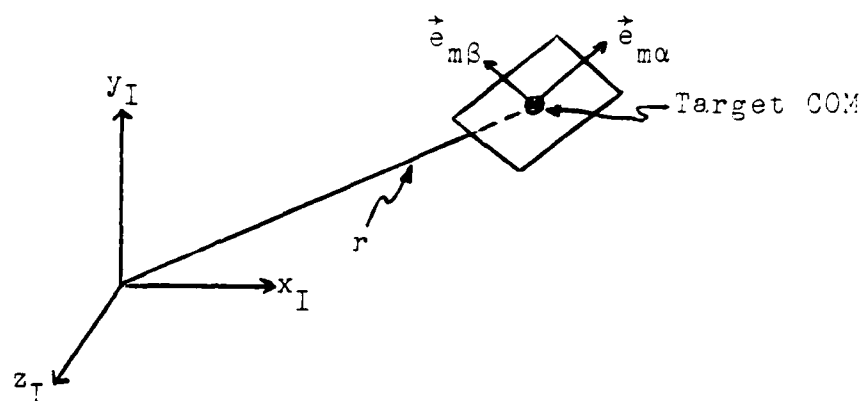
Figure 11 - Translation of the $\vec{e}_{m\alpha}$-$\vec{e}_{m\beta}$ Plane to the
Target COM

From the trajectory model, the velocity vector of the target is known. Since the location of hot spots in a fixed frame can be determined for a specific simulated target, the velocity vector (which is assumed to point towards the nose of the target) can be used to define one axis of another coordinate frame used to accomplish this hot spot determination also having its origin at the target COM. Defining the unit vector in this axis as $\vec{e}_{x}$, two other unit vectors are defined as follows. By performing a cross-product of $\vec{e}_{x}$ with a unit vector ($\vec{e}_{j}$) in the inertial y-direction, a second axis with unit vector $\vec{e}_{y}$ which will always lie in the horizontal inertial plane is defined. The final axis of the new frame is then defined as having a unit vector, $\vec{e}_{z}$, corresponding to

35

the cross-product of the two previously defined target frame
vectors. These relationships are depicted in Figure 12.
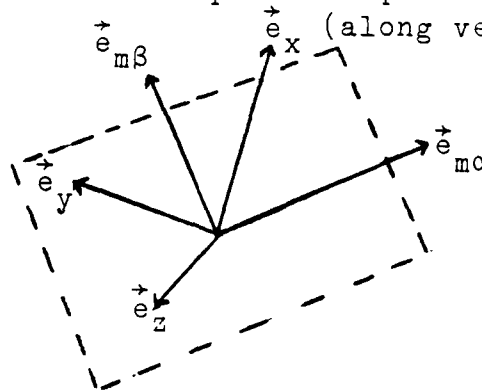
Figure 12 - $\vec{e}_{m\alpha}$-$\vec{e}_{m\beta}$ and $\vec{e}_x$-$\vec{e}_y$-$\vec{e}_z$ Relationships

A coordinate system for the target must now be defined.
Assuming that the target is a multi-engine aircraft with hot
spots as depicted in Figure 13, the arbitrary initial specifi-
cation for this thesis is that the aircraft's initial orien-
tation (of the plane defined by the aircraft wings and fuse-
lage) is coincident with the $\vec{e}_x$-$\vec{e}_y$ plane. Additionally, the
following unit vectors used to establish a coordinate refer-
ence frame for the aircraft are defined: $\vec{e}_{ax}$ from the air-
craft COM towards the nose, $\vec{e}_{ay}$ from the aircraft COM towards
the right wing, and $\vec{e}_{az}$ as the cross-product of $\vec{e}_{ax}$ and $\vec{e}_{ay}$.
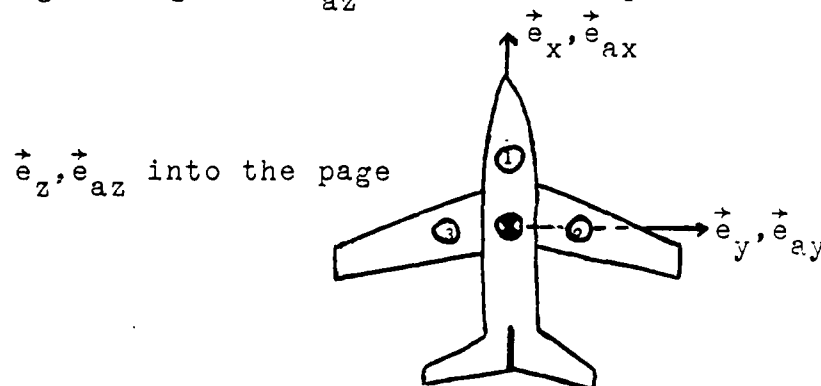
Figure 13 - Initial Ellipsoid Centers

These assumptions and definitions thus specify that the cen-
ter or the ellipsoid due to hot spot 1 in Figure 13 will
always lie along the $\vec{e}_x$ axis. Furthermore, the centers of

36

the ellipsoid due to hot spots 2 and 3 will remain along the $\vec{e}_y$ axis unless the aircraft performs a roll maneuver.

For this analysis, roll maneuvers were simulated by applying one of the constant roll-rates as defined for Trajectory 1 (Section 2.2) as a step input. In a coordinate frame sense, the necessary transformations are depicted in Figure 14. Although a step input application of the maneuver is again done for simulation simplicity, the technique insures that any performance analysis exhibiting adequate or better performance can reasonably be expected to reflect a design which will perform even better in a real world case where the roll-rate would build up smoothly.
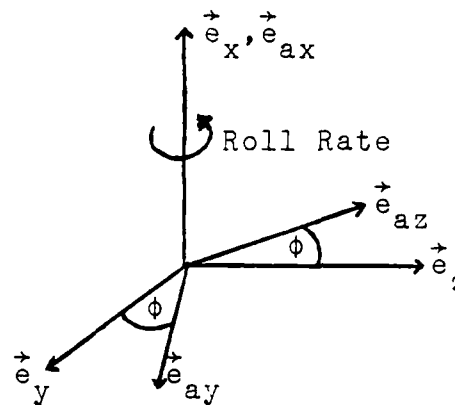
Figure 14 - Roll Maneuver Geometry

Mathematically, the only calculation resulting from performance of a roll maneuver is a simple planar rotation to determine the direction of the ellipsoid centers. For the aircraft roll-rate defined to be ω_r, the amount of planar rotation [with the assumption that $\phi(0)=0$ and t_r defined as the time of roll maneuver initiation] becomes

$$\phi(t) = \omega_r(t - t_r) \qquad (2\text{-}55)$$

The planar rotation depicted in Figure 14 can thus be expressed as

$$\vec{e}_{ay} = \vec{e}_y\cos\phi + \vec{e}_z\sin\phi \qquad (2\text{-}56)$$

and the location of the three hot spots relative to the coordinate frame specified by the aircraft velocity vector and

37

the horizontal inertial plane can always be determined.

All that remains to be done to complete the analysis is to convert the rotated distance to the equivalent offset distance on the FLIR image plane. If Δ_{ay} is defined to be the distance in meters from the aircraft COM to the center of hot spot 2 (lying in the positive $\vec{e}_{ay}$ direction), dot products of this vector length with the "m" plane unit vectors yield the offsets with the required geometry. Specifically, this projection to the $\vec{e}_{m\alpha}$-$\vec{e}_{m\beta}$ plane yields $\Delta_{m\alpha}$ and $\Delta_{m\beta}$ along the $\vec{e}_{m\alpha}$ and $\vec{e}_{m\beta}$ axes as

$$\Delta_{m\alpha} = \Delta_{ay}[\vec{e}_{ay} \cdot \vec{e}_{m\alpha}] \qquad (2\text{-}57a)$$
$$\text{and } \Delta_{m\beta} = \Delta_{ay}[\vec{e}_{ay} \cdot \vec{e}_{m\beta}] \qquad (2\text{-}57b)$$

as shown in Figures 15 and 16.
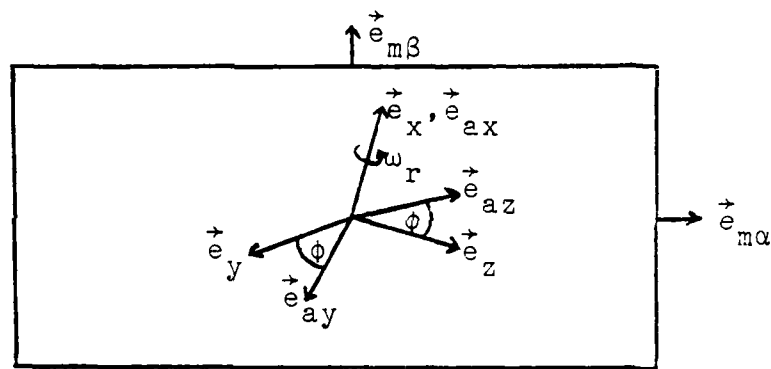
Figure 15 - Hot Spot Offset
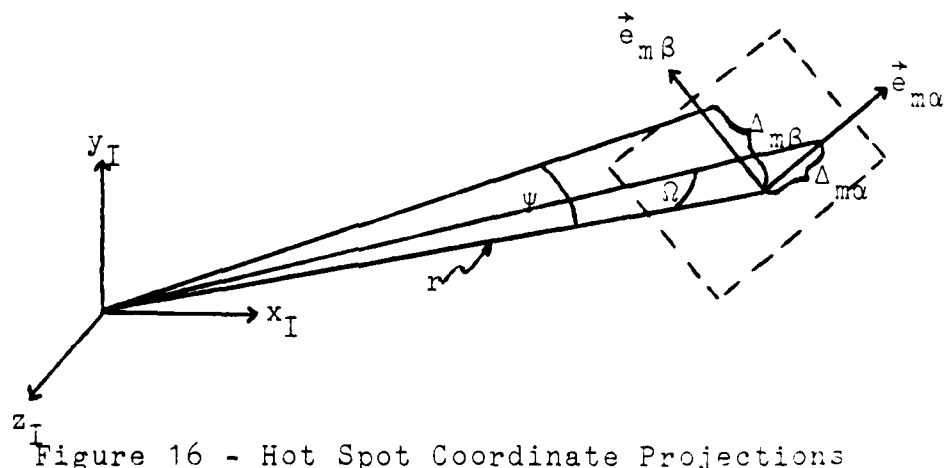
Figure 16 - Hot Spot Coordinate Projections

38

To convert $\Delta_{m\alpha}$ and $\Delta_{m\beta}$ to FLIR image plane offsets requires only simple calculations at this point. Since the $\vec{e}_{m\alpha}-\vec{e}_{m\beta}$ plane is parallel to the FLIR plane and normal to the line-of-sight vector to the aircraft, the small angle approximation is again valid, yielding the FLIR plane displacements

$$\Delta_{\alpha} = \Omega = \Delta_{m\alpha}/r(20\mathrm{x}10^{-6}) \text{ pixels} \qquad (2\text{-}58a)$$
$$\text{and } \Delta_{\beta} = \Psi = \Delta_{m\beta}/r(20\mathrm{x}10^{-6}) \text{ pixels} \qquad (2\text{-}58b)$$

These displacements are then at the FLIR plane location of the center of the ellipsoid due to hot spot 2. Since hot spot 3 is located on the same (aircraft) axis in a reverse orientation and is assumed to be at the same distance from the aircraft COM as hot spot 2, its offset can readily be calculated to be $(-\Delta_{\alpha}, -\Delta_{\beta})$.

To demonstrate this projection, previous efforts (7,8,23) have run a simple trajectory having the initial inertial coordinates

$$x_I(0) = y_I(0) = z_I(0) = 10 \text{ km}$$

and the constant inertial velocities

$$\dot{x}_I(t) = \dot{y}_I(t) = \dot{z}_I(t) = -0.5 \text{ km/sec}$$

Since this defines a target moving directly towards the center of the FLIR image plane and having a velocity vector normal to the FLIR image plane,

$$\dot{\alpha}(t) = \dot{\beta}(t) = 0$$

for the entire trajectory. Hot spots were defined as

    1 at one meter forward of the aircraft COM
        along $\vec{e}_{ax}$
    2 and 3 at ±0.5 meters on the sides of the aircraft
        COM (along $\vec{e}_{ay}$)

and two simulations were used to demonstrate the projection model.

The first simulation, depicted in Figure 17, shows that for a roll of π radians, the ellipsoid center due to hot spot 1 stays centered in the FLIR plane, while the ellipsoid
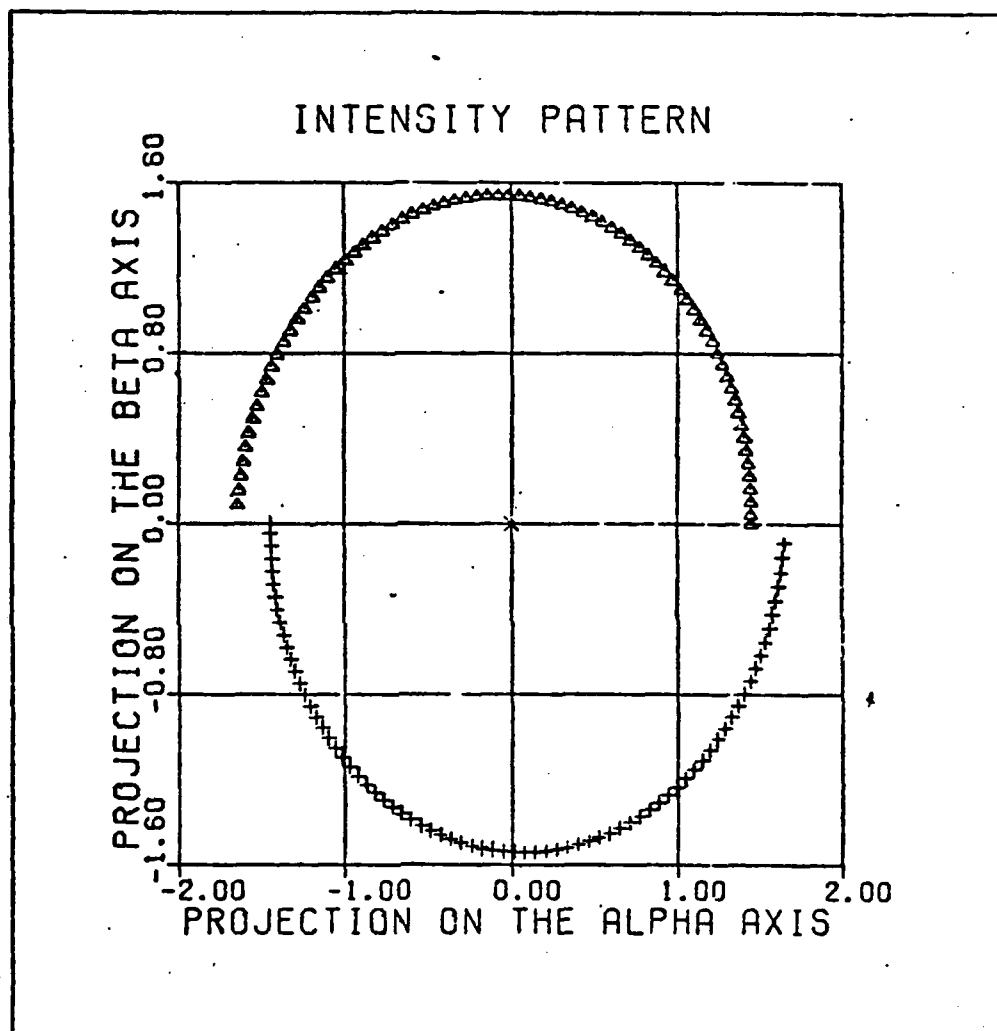
Figure 17 - π Radians Roll

centers due to hot spots 2 and 3 roll through π r
while remaining at a relative position (to each o
radians. The pixel offset change in the figure (
seen in Figure 18 which depicts a roll of 2π radi.
to the increase in projected hot spot offset dist:
function of the decreasing range. For example, f
simulation time of five seconds, the initial pixe.
for the two hot spots in the horizontal FLIR dimen

$$\pm\Delta_\alpha = \frac{\pm 0.5}{[3\times(10,000)^2]^{\frac{1}{2}}(20\times10^{-6})} = \pm1.44 \text{ p:}$$

whereas at the termination of the simulation, the:

$$\pm\Delta_\alpha = \frac{\pm 0.5}{[3\times(7500)^2]^{\frac{1}{2}}(20\times10^{-6})} = \pm1.93 \text{ pi:}$$

For a target performing a roll through 2π rad
gure 18 clearly illustrates the above relationshiμ
maintaining the correct offsets as defined. Thus
is valid and can be used for the multiple hot spot

Now that the truth model used to input data t
ter model has been defined, the next step of this
quires that the tracking algorithm to be used be ±
scribed prior to depicting the results of the syst
formance analyses. Since a hybrid (optical/electr
processor has been determined to be the solution c
for this effort, the most logical method of accomμ
this step is to follow the flow of data from input
As the input stage requires a complete definition
enhanced correlator and the (optical) method of it
mentation, Chapter III is devoted solely to this t

41

Figure 18 - 2π Radians Roll

42
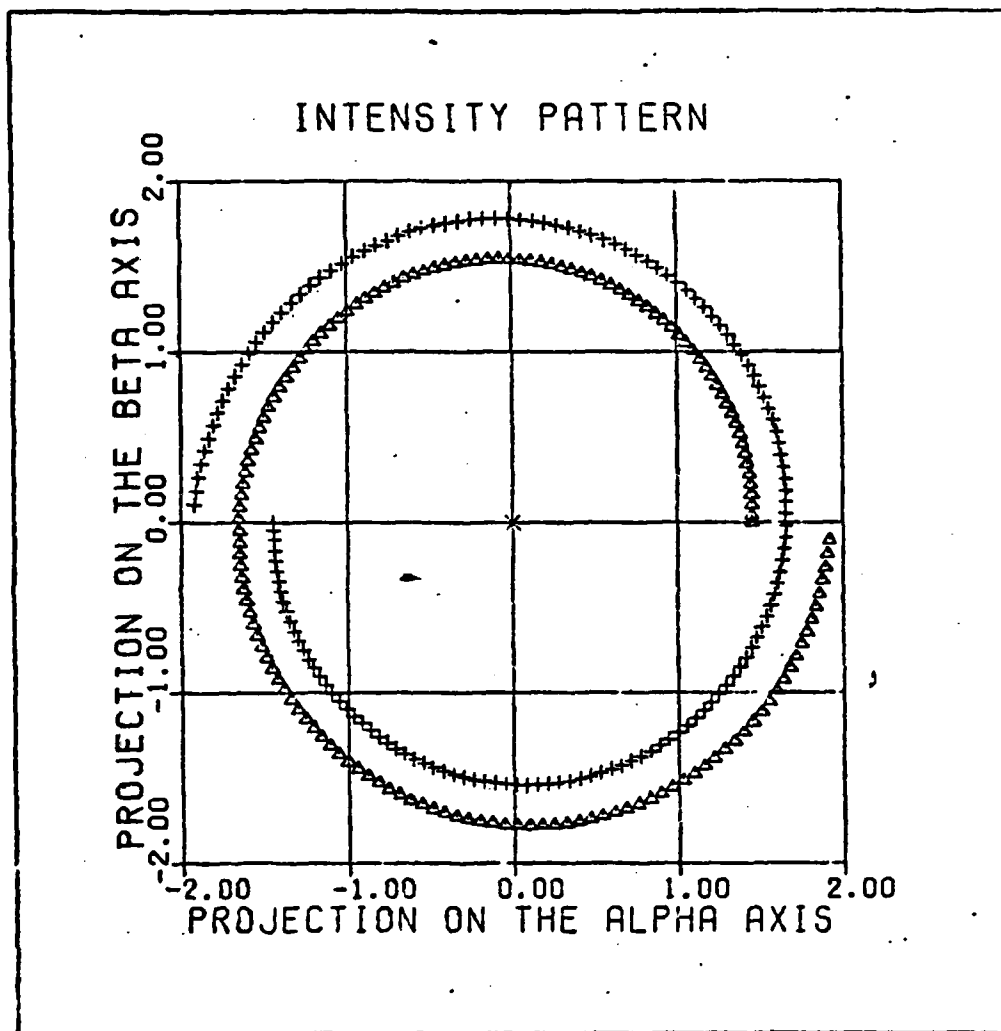
III. Enhanced Correlator

3.1 Overview

The sole thrust of this chapter is to define the enhanced optical correlator (EOC) completely. To accomplish this task requires that the original electronic implementation (23) of the correlator be both mathematically specified and justified as well as the optical processor to be used. The one additional analysis required to complete this chapter is the comparison of the projected EOC performance with that obtainable from a software implementation after all EOC components have been specified.

Two points require clarification before proceeding with the analysis. First, the software processed version of this algorithm uses the raw intensity data obtained from each FLIR frame as the input to the correlator. The correlator then processes this data to obtain the noise corrupted target position offset measurements from the center of the FLIR tracking array field of view, $\underline{z}(t_i)$. In contrast, the optically processed enhanced correlator uses the projected IR image (that would be seen by a FLIR array sensor if one were present) as its input. It then projects the required correlations for a simple target center of mass calculation onto a measurement array sensor. As a FLIR array sensor was mandated for these efforts, such a sensor is used in all analyses. Chapter V suggests some alternatives in this area which have the potential for significantly enhancing the performance of the overall tracking system.

Secondly, successful demonstration of the optically processed enhanced correlator thus requires that it output equivalent or better results than those obtainable from a software implementation of the algorithm. This is particularly true due to the method by which each version generates the required Fourier transforms outlined in Section 3.2. Although previous analyses (23) have shown that the algorithm

43

used in the software version is essentially insensitive to wordlength, it is obvious that the quality of the transforms (particularly those due to images corrupted by noise) is dependent on the specific discrete Fourier transform (DFT) software used in the correlator. When the requirement of processing within the 30 Hz FLIR frame rate (especially when combined with the additional processing required) is combined with the infeasibility of having a large main-frame computer at every weapon site, it can be postulated that the quality (in terms of correlation peak locations) may suffer in an actual implementation due to use of a more efficient but less accurate DFT algorithm. In an optical version, the limitation in transform production (at least for the optically produced transform of the noise-corrupted signal) is dus to two factors. Since analog processing is used, the transform quality is initially limited by the dynamic range of the modulators used (here, approximately 40 dB at best). Additionally, since the optical transform is produced spatially and optical components do not have infinite dimensions, some transform components are lost (this will be addressed in Section 3.3). However, due to the nature of the algorithm outlined in Section 3.2, direct comparison of the optically processed correlator to the software processed version as previously defined (23) is achievable, because the limitations outlined for the optical package are of negligible significance for data of very low frequencies as in this case. Thus, the analysis in Section 3.4 provides a direct comparison of the EOC implementation to a large main-frame (Cyber 175) implementation.

With these points clarified, the mathematics to be used must be specified. The following section performs this task for the algorithm itself. Those interested in details of the software implementation may wish to consult Appendix A of this thesis which is identical to the same section of Reference 23.

3.2 Enhanced Correlator Algorithm Development

The concept behind the enhanced correlator algorithm represents a desire to combine the benefits offered by the relatively low computational burden of a correlation algorithm (as compared to a highly-dimensioned extended Kalman filter) with the statistical accuracy (in an environment which is not free of sources of error) available from a Kalman filter. Additionally, the developed algorithm, by exploiting knowledge about the target's dynamics and any disturbances which have the potential to cause apparent translational intensity function offsets, enhances performance over standard correlation algorithms which use only the raw data from previous frames.

To accomplish these actions, the template to be used for correlation is generated from data obtained directly from the propagation cycle of the Kalman filter which will be described in Chapter IV. Specifically, the propagated state estimates, $\underline{\hat{x}}(t_{i+1}^-)$, are used to generate [from Equation (2-39)] an estimated FLIR target intensity function, $\underline{h}[\underline{\hat{x}}(t_{i+1}^-), t_{i+1}]$. This estimated FLIR target intensity function has two important properties: (1) it is due to a target center of mass (COM) located exactly at the center of the FLIR image plane since the propagation cycle of the Kalman filter produces the necessary data to center the target in the tracking window field of view (FOV); and (2), it is uncorrupted by either temporal or spatial noise by design. These properties, combined with the template's incorporation of image intensity changes due to target roll rates and/or range rate changes (see Section 2.5), would thus correlate perfectly with an intensity pattern due to a perfectly modeled target in a noise-free environment.

Since it is as impossible to model the target parameters of interest perfectly in the real world as it is to have a noise-free environment, correlation of a template representing an assumed perfect target intensity in an ideal (free

45

of noise) environment with the signal due to the actual process in a real environment will yield the best correlation that can be expected. In either a purely electronic or optical configuration, this correlation is best transformed in the transform domain. Defining

$$F[\underline{g}(\alpha,\beta)] = \underline{G}(f_\alpha, f_\beta) \qquad (3\text{-}1)$$
$$\text{and } F[\underline{l}(\alpha,\beta)] = \underline{L}(f_\alpha, f_\beta) \qquad (3\text{-}2)$$

to be the Fourier transforms of the two-dimensional pixel sequences $\underline{g}(\alpha,\beta)$ and $\underline{l}(\alpha,\beta)$, their cross-correlation $\underline{R}(\alpha,\beta)$ can be written as

$$\underline{R}(\alpha,\beta) = \underline{g}(\alpha,\beta) * \underline{l}(\alpha,\beta) = F^{-1}[\underline{G}(f_\alpha, f_\beta) \cdot \underline{L}^*(f_\alpha, f_\beta)] \qquad (3\text{-}3)$$

where $\underline{L}^*(f_\alpha, f_\beta)$ represents the complex conjugate of $\underline{L}(f_\alpha, f_\beta)$. If it is further postulated that $\underline{l}(\alpha,\beta)$ represents the estimated FLIR target intensity function $\underline{h}[\hat{\underline{x}}(t_{i+1}^-, t_{i+1})]$ from the Kalman filter and $\underline{g}(\alpha,\beta)$ represents the actual FLIR target intensity sequences, it is easy to see that implementation of the algorithm of Appendix A yields the required Fourier transforms required for the enhanced correlator.

To examine the correlation in specific detail, consider the simple case of correlating two two-dimensional Gaussian structures. Here, $\underline{l}(\alpha,\beta)$, as depicted in Figure 19, is the template due to a single hot spot target which is sufficiently far enough away from the tracker (or a target with a circular cross-section having a velocity vector normal to the FLIR plane) to have circular equal intensity contours with $\sigma^2 = 2$ pixels. Furthermore, the representation of the target as depicted reveals that the template data is padded by surrounding the original 8x8 array by eight rows and columns of zeros to generate a 24x24 pixel array structure. This artificial bandwidth limitation (as the Fourier frequencies are now present in a spatial sense) of an assumed periodic in two dimensions mathematical function which in reality is infinite in extent allows the FFT algorithm to represent the transform far more accurately than for the case of a non-padded array where higher frequencies are undefined.

46
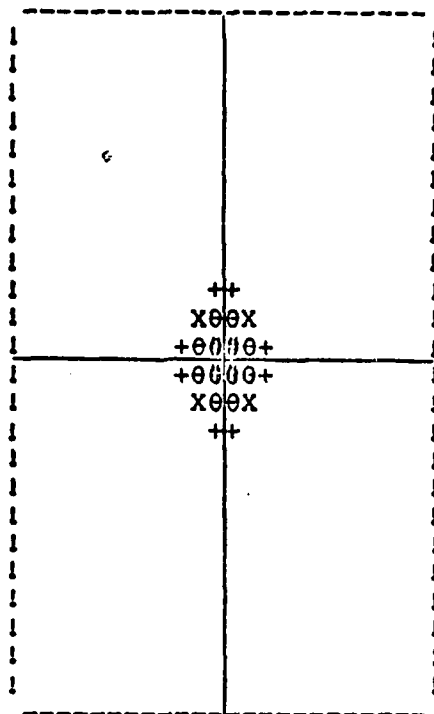
Figure 19 - Centered Single Gaussian Template

Similarly, Figure 20 depicts a typical representation of $\underline{g}(\alpha,\beta)$. This array of slightly noise-corrupted data, containing the target's offset intensity function, is offset by one pixel in the horizontal ($\vec{e}_\alpha$) direction from the center of the 24x24 pixel array. Correlation of the data depicted in Figures 19 and 20 then produces the cross-correlation, $\underline{R}(\alpha,\beta)$, depicted in Figure 21.

Noting that the expected result of correlating two Gaussian arrays is another Gaussian array, it can easily be established that the symmetry of the correlation array will be representative of any offsets (spatial frequency differences) present between the two input data arrays. The data in Figure 21 shows this information explicity. In the vertical ($\vec{e}_\beta$) direction, $\underline{R}(\alpha,\beta)$ is symmetric which indicates that no offset is present in this dimension between the target and template. The fact, however, that a one pixel circular shift to the left is required to restore symmetry (a function of the assumed origins of the two images in performing the DFT) in the horizontal direction clearly shows that $\underline{R}(\alpha,\beta)$ does

```
                    +X +
                    XθOX
                   +θθθθ+
                   +θθθθ+
                   +XθθX
                    +++


               +                        + 
            + +            ÷
                     +
                +
```
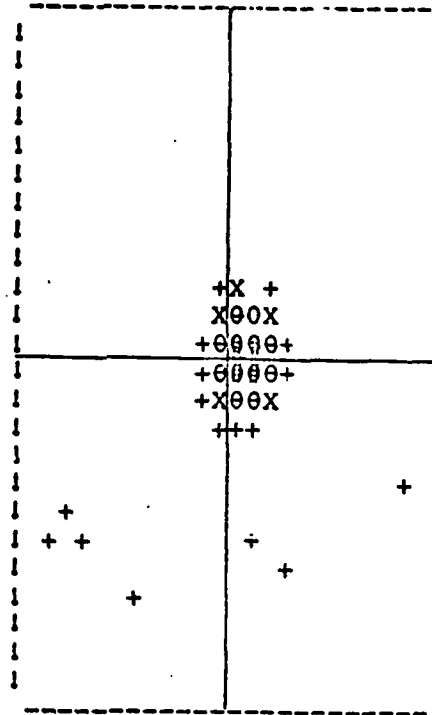
Figure 20 - Noise Corrupted Data Array

```
!θθθθX+                              Xθ!
!θθθθX+                             +Xθ!
!θθθX+                              +X!
!XXX+                                +!


              I            II




!++
!XX++                                +!
!θθθX+                              +X!
!θθθθX                              +0!
```
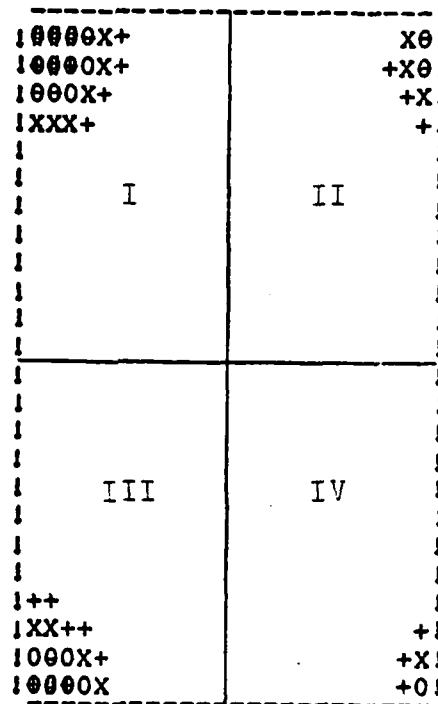
Figure 21 - Result of Cross-Correlation of Data and Template

48

indeed contain the $\underline{g}(\alpha,\beta)$ offset information due to the target's true position relative to the tracking window at the sample time.

Before proceeding further with the analysis, it is important to note that use of the circular shift is justified by the assumption that the Fourier transforms produced are in reality infinitely periodic. Since the data contained in $\underline{R}(\alpha,\beta)$ represents only a single period of the result, the next pixel to the left of column one is defined to be equal to the corresponding pixel in column 24. Similarly, corresponding pixels in rows one and 24 are defined. Once these definitions are made, the correlation data depicted in Figure 21 can be restructured to a more useful form.

This $\underline{R}(\alpha,\beta)$ data restructuring is depicted in Figure 22. Here, in line with the definitions established above, the original correlation data (Figure 21) of quadrant I is
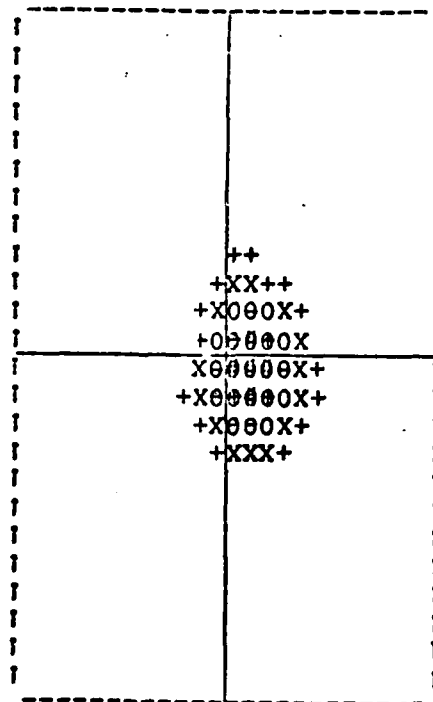
Figure 22 - Diagonal Quadrant Swap of Cross-Correlation

swapped with the original correlation data of quadrant IV. In a similar manner, the data of quadrants II and III are also swapped. This 180-degree circular shift over two dimensions produces a $\underline{R}(\alpha,\beta)$ representation where the relative position offset between the template and target is now the offset of the resulting Gaussian's maximum from the center of the sequence. This form thus enables an easy and efficient calculation of the offsets as will be described.

It is important to note at this point that this shift is only required for a purely electronic implementation of the algorithm. This is due to the fact that the origin of the correlation depicted in Figure 21 directly corresponds to the origins of the original two data sequences depicted in Figures 19 and 20. Use of this convention requires that the origins of the original two sequences be superimposed to create the first correlation data point. Thus the correlation data corresponding to the four pixels which surround the centers of the FOVs of the original two sequences is contained in the four corner pixels of the correlation matrix. By defining the center of the 24x24 correlation matrix as the correlation of the centers of the original sequences, the enhanced optical correlator directly produces the data depicted in Figure 22.

Returning to the analysis, a comparison of the original Gaussian template, $\underline{1}(\alpha,\beta)$, depicted in Figure 19 with the $\underline{R}(\alpha,\beta)$ output shown in Figure 22 reveals some degeneracies which must be addressed. Specifically, these degeneracies are a spreading of the function as well as some degree of assymmetry caused by the noise present in the $\underline{g}(\alpha,\beta)$ sequence. Since the $\underline{R}(\alpha,\beta)$ pixel magnitudes correspond directly to the degree of resemblance between the noise-free template and the noisy target signal, simple thresholding of the $\underline{R}(\alpha,\beta)$ data can produce significant smoothing of the correlation. The use of thresholding is justified if the assumption is made that the correlations produced by the noise and template are insignificant in magnitude compared

to the correlations of interest. Additionally, the use of thresholding allows an easy calculation of the CCM rather than a more complicated and ambiguous peak detection scheme. Figure 23 thus depicts the result of setting the threshold at half the value of the maximum magnitude of the correlation shown in Figure 22. The data of Figure 23 was produced by subtracting the threshold value from each pixel in turn. If the resulting magnitude was less than or equal to zero, the element was considered to contain poor correlation information and thus was set to zero. All resulting positive magnitudes were retained at their original (pre-thresholding) values. As can clearly be seen in Figure 23, significant smoothing of both degeneracies is induced.
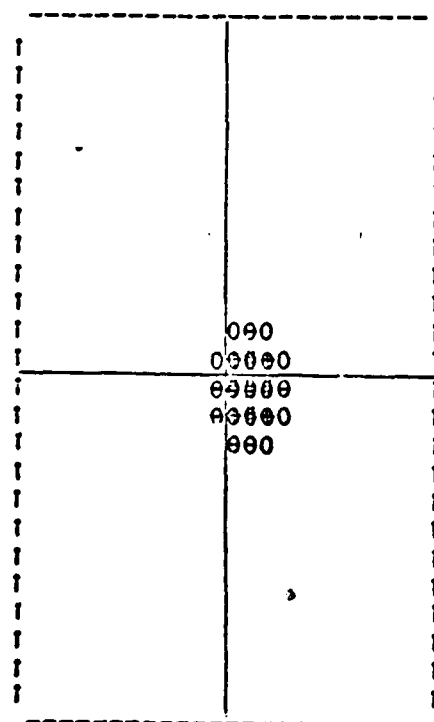
Figure 23 - Result of Thresholding of .5

The fraction of the sequence maximum magnitude used as the threshold warrants careful investigation. If it is set too low, the correlations due solely to the noise are not

significantly countered and the resulting COM statistics
suffer. The original development (23) of the enhanced cor-
relator used 0.5 as the threshold fraction. Further efforts
in this area (21) have indicated a potential for enhanced
performance if a value of 0.3 is used. Thus, although the
example used for illustrative purposes above uses the 0.5
threshold value, the analyses of the enhanced correlator
operation as defined in this thesis directly represent the
use of the lower stated value.

Now that the data has been obtained in a usable form,
an efficient means of extracting it is required. Instead of
a peak detector, the enhanced correlator uses a centroid
summation of the $\underline{R}(\alpha,\beta)$ sequence since it is assumed that
the center of mass of the threshold correlation is a good
indication of the peak location. Specifically, for either
the horizontal or the vertical direction, this centroid
summation is defined as

$$C = \frac{\sum\limits_{i=1}^{N} i \cdot |I_i|}{\sum\limits_{i=1}^{N} |I_i|} \qquad (3-4)$$

where i is the horizontal or vertical coordinate of a given
pixel, $|I_i|$ represents the magnitude of the pixel intensity
at that location, and N is the total number of pixels in the
array. Equation (3-4) is thus used twice in the correlator,
one time to produce the horizontal centroid and the second
time to produce the vertical centroid. The resulting cen-
troid, $\underline{C}(\alpha,\beta)$, is then the measured position offset of the
target from the center of the data frame.

The development of Equation (3-4) concludes the speci-
fication of the enhanced correlator. Since this thesis en-
visions the use of an optical architecture to perform this
enhanced correlation, the design of the enhanced optical
correlator must be specified and its performance analyzed.
The next section thus specifies the EOC design.

52

3.3 Enhanced Optical Correlator Design

Prior to EOC design specification, an outline of the basic laws of Fourier optics as they pertain to this development is required. Since this outline can hardly be termed comprehensive, the reader interested in exploring this topic further is urged to consult Reference 6.

Starting with the simple case, consider first the system illustrated in Figure 24. This two-dimensional system uses (as indeed do all optical transform systems) optical interference to process incoming signals. Specifically, light from a laser point source S is collimated by lens L_c. This collimated beam of quasi-monochromatic coherent light (as defined further in Chapter V) then illuminates an object placed in plane P_1 resulting in the formation of a diffraction pattern. By placing the object exactly one focal length (f_1) in front of the transform lens L_1, a phase-flat classical Fraunhofer diffraction pattern, $t_0(x_2,y_2)$, due to the object's space-varying amplitude transmittance is formed at plane P_2 located at exactly one focal length behind L_1. The complex field of this Fraunhofer diffraction pattern is mathematically equal to the spatial Fourier transform of the object. This can clearly be illustrated by comparing both mathematical definitions, which are

$$T_0(x_2,y_2) = k_1 \iint t_0(x_1,y_1) \exp\left[\frac{-j2\pi}{\lambda f_1}(x_2 x_1 + y_2 y_1)\right] dx_1 dy_1 \qquad (3-5)$$

$$T_0(f_x,f_y) = k_1 \iint t_0(x_1,y_1) \exp\left[-j2\pi(f_x x_1 + f_y y_1)\right] dx_1 dy_1 \qquad (3-6)$$

where

$k_1 \equiv$ a complex constant required for each integral

$T_0(x_2,y_2) \equiv$ Fraunhofer diffraction pattern at P_2

$T_0(f_x,f_y) \equiv$ Fourier transform of the spatial frequencies of the object at P_1 at P_2

and $\lambda \equiv$ wavelength of the laser

As the quantities $(x_2/\lambda f_1)$ and $(y_2/\lambda f_1)$ do indeed define the
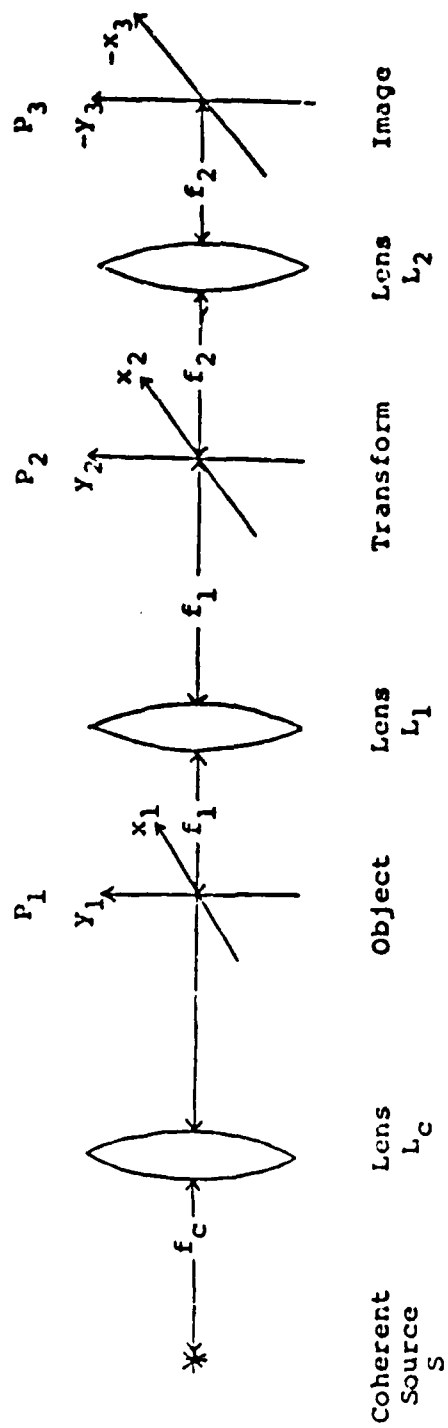
Figure 24 – Basic Optical Processing System

54

horizontal and vertical spatial frequencies, resp
due to the object at P_1, the two expressions are
tically identical.

With a Fourier transform available at P_2, m
of its information can be simply produced. By p
optical filter at P_2, the complex optical filter
produces a second diffraction which is then colle
L_2. Defining f_2 to be the focal length of L_2, a
image is produced at plane P_3 when configured as
Figure 24.

Extending these principles to the dynamic ca
EOC, simple extensions from the static case outli
serve to define the required process completely.
image formed at the FLIR image plane is a dynamic
of the static object specified at P_1. Since this
actually $\underline{g}(\alpha,\beta)$, it can easily be seen that $\underline{G}(f_\chi,$
produced at P_2. Since this transform must be mul
$\underline{L}(f_\alpha,f_\beta)$ in order to produce the required correla
$\underline{R}(\alpha,\beta)$, some type of modulator is required to "fi
$\underline{G}(f_\alpha,f_\beta)$ data points on a real-time (or pseudo re
basis. It is important to note that this modulat
able to represent $\underline{L}(f_\alpha,f_\beta)$ as defined in Section
suming for the moment that such a modulator is av
it is obvious that the resulting diffraction patt
reality the multiplication of the two transforms
by Equation (3-3). Thus, as L_2 is in effect prod
Fourier transform of a Fourier transform, the res
verted image at P_3 is $\underline{R}(\alpha,\beta)$. By placing an arra
at this image plane, the required cross-correlati
readily be converted back into an electronic sign
electronic signal is then used to compute $\underline{C}(\alpha,\beta)$
thresholding all of the data.

Since the type of array detector to be used
been specified, the only true component variable
specified is the modulator to be used. Although

55

the requirement of proper lens specification, the statement is valid due to the fact that modulator choice will specify lens choice, since the modulator dimensions will determine the spacing between the discreet transform frequencies which a lens must provide. Here, lens choice is completely determined by the relative spatial dimensions of the FLIR array sensor pixels and the modulator pixels as the FLIR image plane (P_1) image is assumed to correspond exactly with the FLIR array sensor. Thus, an examination of the performance requirements of the modulator will serve to specify the appropriate choice of modulator from those available and the balance of the system as well.

Looking at the obvious requirements, the modulator must both be able to modulate the IR signals of interest efficiently and be able to perform this modulation at a minimum system throughput rate of 30 Hz. The efficiency requirement arises from two factors: (1) the IR signals of interest cover a fairly wide dynamic range (at least 30 dB given the original use of the FLIR sensor at the image plane); and (2), not all modulators are designed to operate at the IR wavelengths of interest. Additionally, detectors at these wavelengths (30) do not exhibit high quantum efficiencies (the ratio of electrons emitted per photons incident). Since the minimum system throughput rate precludes the normal method of longer integration times to produce larger signals, the efficiency requirement is the determining factor. Additionally, as all of the modulation devices outlined in Chapter I are capable of operation at 30 Hz, the efficiency requirement becomes the mandatory performance criterion factor as well.

Other performance criteria exist which would enhance (or not detract from) system performance and thus are desirable. Foremost among these is pixel dimension compatibility (with the FLIR array sensor pixel size) so that extensive image magnification which can lead to optical aberrations can be avoided. Secondly, an ability to support a system throughput

56

rate greater than 30 Hz (while maintaining the modulation efficiency) is desired. Finally, since the Fourier transform $\underline{L}(f_\alpha, f_\beta)$ is produced in software, direct digital loading to the device is desirable to avoid the delay incurred by D/A conversion. Basically, these desired performance criteria indicate a desire to provide a noise-free correlator (despite thresholding elimination of any errors that would be produced) in terms of the optics themselves as well as providing the ability to support higher bandwidth tracker operations.

Out of all the modulators outlined in Chapter I, all of these criteria merge in only one distinct modulator. This modulator, manufactured by Texas Instruments, is the TI deformable mirror assembly. From the TI specification sheet (Number 82-149, March 1982), the performance criteria of interest are:

Modulation Bandwidth	120 Hz
Dynamic Range	>42 dB from DC to 100 Hz
Modulation Efficiency at Wavelengths of Interest	0.88
Input Signal Required	14-bit Digital
Pixel Dimension	Same as FLIR array
Pixel-to-Pixel Accuracy	±1 bit

Since all specifications, both mandatory and desired, are met or exceeded only with this modulator, it is obvious that this is the modulator of choice. It must be noted, however, that choice of this modulator requires thermoelectric coolers for optimal performance. This is due to the fact that the mirrors on the array are metallic and will partially absorb the IR signals. Since this requirement is easily met, the final design can now be specified.

As illustrated in Figure 25, this design is quite simple. It is assumed both here and in the analysis of Section 3.4 that optical bandpass filtering to produce an image of only the signals of interest is accomplished by the input optics.
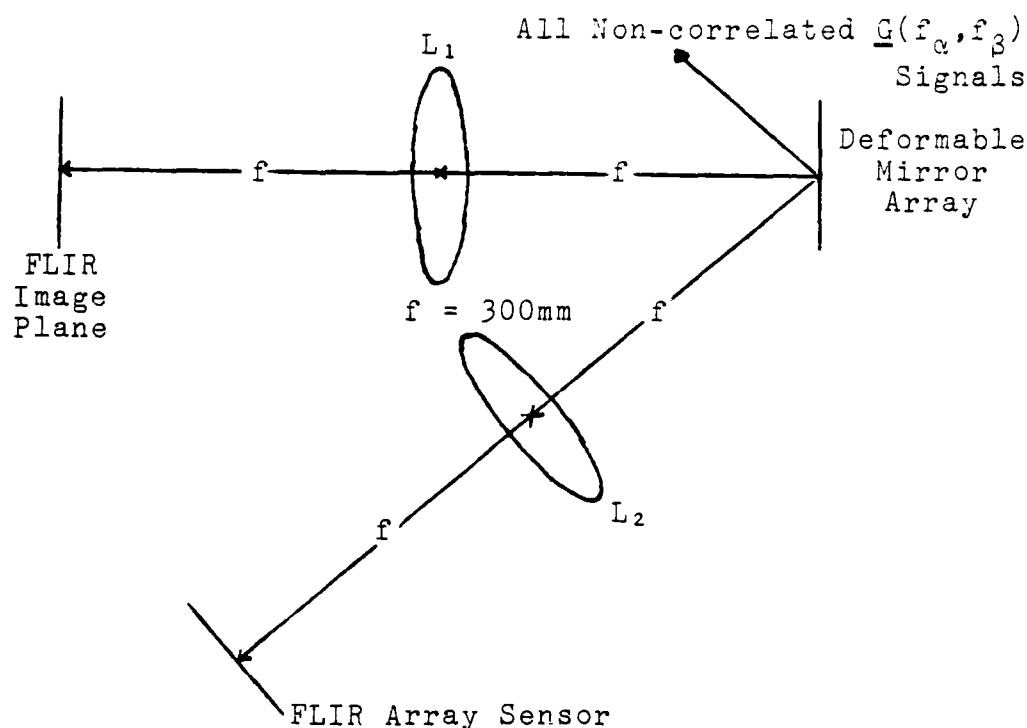
Figure 25 - Enhanced Optical Correlator Design

The choice of lenses illustrated is a direct result of positioning the optical transform products $\underline{G}(f_\alpha, f_\beta)$ produced by L_1 at the centers of each pixel of the deformable mirror array. Additionally, both L_1 and L_2 have the same focal length so as to maintain the same image size at both input and output planes. The only other pertinent fact of interest is the option made available by the larger-than-required dynamic range. This option allows for image intensification in the following manner. Since the magnitude of I_{Max} is known from the previous frame of data, the next frame can boost or lower the maximum value (and thus all other values) of $\underline{L}(f_\alpha, f_\beta)$ to compensate at least partially for low dynamic range signals. Use of this option, although unexplored for this effort, would thus maintain FLIR sensor operation at as efficient a level as is possible.

Now that the EOC design has been specified, an analysis of its performance, particularly compared to an enhanced correlator implemented totally in software, is required for system acceptance. This process is accomplished next in Section 3.4.

3.4 EOC Performance Analysis

Before developing the system MTF, the system operating characteristics must be specified. For the purpose of this thesis, these characteristics are specified to be: (1) system operation at a throughput rate of 30 Hz; (2) input of the maximum intensity of $\underline{L}(f_\alpha, f_\beta)$ at +30 dB to the modulator; and (3), use of the FLIR array sensor as defined.

The EOC MTF is developed here only to illustrate the flatness (i.e., the uniform response) of the optical system. Since the image cannot be altered, the only parameters of interest are the system components. With the lens diameters specified to be at least four times the image size at the image plane, the lenses produce no significant aberrations that would affect image quality as defined. Similarly, use of a FLIR array sensor does not produce any noise which has not been previously modeled. This leaves only the deformable mirror array as a potential source of error.

Since this modulator is specified as having ±1 bit accuracy, the worst case is considered. Assuming two contributing (at the image plane P_3) one-bit errors are made while operating at the 30 dB (10-bit) dynamic range specification, the relative error would be

$$\% \text{ variation} = (2/1024) \times 100 \cong 0.195\% \qquad (3\text{-}7)$$

which is insignificant. Thus the image produced at the FLIR array sensor is subject to a maximum error that, if considered noise, would be far below the other noise sources of the problem.

The major analysis of interest is a comparison of the optical transform quality with that obtainable from a software implementation. Here the parameter of interest is the relative spatial frequencies obtainable by each method. If the optical system can produce transforms of equal or better resolution than those implemented in software, use of the EOC is enabled. For this case, the limiting system resolution will be the transform developed in software, $\underline{L}(f_\alpha, f_\beta)$.

Since this transform is limited by the FLIR array sensor (or modulator) spatial resolution in either the EOC or a software implementation, the center-to-center pixel distance becomes the limit. As this distance is specified (by the same specification sheet outlined earlier in this section) to be one millimeter for either dimension, the maximum spatial resolution required is one per millimeter. As the field of Fourier optics can easily generate spatial resolutions of 100 per millimeter (6), the spatial resolution required is well within the achievable bounds of the EOC and its use is justified.

With $\underline{R}(\alpha,\beta)$ available, software will be used to generate $\underline{C}(\alpha,\beta)$ after thresholding. This process is described in detail in Chapter V. Since $C(\alpha,\beta)$ is the desired measurement to be incorporated within the filter, the next logical step in the development of the proposed tracker is to specify the filter models used. Only after the filter algorithm has been described can the optical Kalman filter be specified and the entire system subjected to performance analyses. Thus, the next chapter is devoted to this task.

IV. Filter Models

4.1 Overview

Inherent to any Kalman filter algorithm is the strict separation of its two distinct functions, propagation and measurement. Since the Kalman filter is designed to operate in a stochastic (uncertain) environment as well, each filter design requires two models given the assumption that the measurement uncertainty is truly independent of the uncertainty due to incomplete knowledge of the system's dynamics. The first of these required models is the measurement update model, which is used to generate enhanced state (variable of interest) estimates from measurements which are assumed to be corrupted by noise. The other required model propagates the enhanced state estimates forward in time based on knowledge of the system's dynamics (which are assumed to be known with some degree of uncertainty). As such, it is termed the system dynamics model.

Although a relatively new field in filtering, a large number of stochastic filter algorithms are available (11,15,17). These include both linear and nonlinear Kalman filters as well as several types of second-order filters, some of which can be implemented either on a continuous-time or a sampled-data basis. Here, the sampled-data basis is required by the problem definition. However, the problem definition does not specify a choice as to the type of stochastic filter algorithm to be employed.

Noting that the measurement update and sytem dynamics models for this problem have been implemented in both linear and nonlinear form in the past, a set of tradeoff criteria needs to be developed to make a realistic design choice (given the necessity of operating within the FLIR 30 Hz frame rate) from the available options. As in all other engineering professions, the most important criterion is the ability of the system to perform at an acceptable level over the full

range of the problem specification. However, particularly in
military systems, better than the defined acceptable perfor-
mance level is often desired. This may necessitate accepting
the additional computational burdens of a nonlinear Kalman or
second-order stochastic filter algorithm in order to provide
more realistic modeling. If such is the case, the system
sampling rate may have to be decreased due to the additional
computation time incurred. Since fewer measurements are thus
available for a given time period, the performance enhance-
ment obtained may not be justifiable. This is particularly
true if the decrease in sampling rate requires a major re-
structuring of previously specified system components.

As outlined in Chapter I, this thesis problem arises
from this dilemma. Here, two methods of solution are used
to generate an achievable filter algorithm (in terms of the
time specification) with enhanced performance: (1) optical
processing techniques with their inherently higher processing
rates are used extensively throughout the system; and (2),
a linear measurement model, deemed to have sufficient accu-
racy for the desired tracking system performance, is used in
place of a nonlinear algorithm in an attempt to reduce the
overall computational burden. By using both of these solu-
tions, the disadvantages of additional computational burden
are overcome while yielding the performance enhancement due
to more realistic modeling of the problem's dynamics.

To define the filter in the most logical manner, sepa-
rate sections are devoted to each filter model. In a tempo-
ral sense, the next system activity after production of the
centroid coordinates, $\underline{C}(\alpha,\beta)$, is the Kalman filter measure-
ment update cycle. As such, the next section fully describes
this model. Section 4.3 then concludes this chapter with a
description of the filter's propagation cycle as specified
by the state dynamics model.

4.2 Measurement Update Model

Recalling that the input $\underline{C}(\alpha,\beta)$ to the measurement update cycle of the filter is in reality the target's center-of-mass (COM) position in the tracking window, a linear law is easily developed. By defining

$$\underline{C}(\alpha,\beta) = \begin{bmatrix} \alpha_c & \beta_c \end{bmatrix}^T \qquad (4-1)$$

where α_c and β_c are the measured target's COM pixel positions, at a given sample time t_i

$$\underline{z}(t_i) = \begin{bmatrix} \alpha_c(t_i) & \beta_c(t_i) \end{bmatrix}^T \qquad (4-2)$$

where $\underline{z}(t_i)$ is the discrete-time measurement vector required by the model.

Before specifying the model, however, several other definitions are required. First, the state vector itself must be specified. Here an eight-state state vector is defined as

$$\underline{\hat{x}}_F = \begin{bmatrix} \hat{\alpha}_D & \hat{\beta}_D & \hat{v}_\alpha & \hat{v}_\beta & \hat{a}_\alpha & \hat{a}_\beta & \hat{\alpha}_A & \hat{\beta}_A \end{bmatrix}^T \qquad (4-3)$$

where the subscript F denotes a filter variable, the caret superscript denotes an estimate,

$\hat{\alpha}_D$, $\hat{\beta}_D$ ≡ FLIR plane target position estimates due to the target's dynamics

$\hat{v}_\alpha$, $\hat{v}_\beta$ ≡ FLIR plane target velocity estimates

$\hat{a}_\alpha$, $\hat{a}_\beta$ ≡ FLIR plane target acceleration estimates

and $\hat{\alpha}_A$, $\hat{\beta}_A$ ≡ FLIR plane target position estimates due to atmospheric effects on the signal of interest

Additional variables requiring definition are

t_i^- ≡ time immediately prior to measurement availability, to which all state and state uncertainty values are propagated

t_i^+ ≡ time postulated to be immediately post measurement which represents state estimate and state covariance (uncertainty) measurement-enhanced values

63

$\underline{v}(t_i) \equiv$ additive noise corruption at the sample time, assumed to be white, and Gaussian, with statistics to be determined

$\underline{R}(t_i) \equiv$ the degree of measurement uncertainty due to $\underline{v}(t_i)$: specifically, $E\{\underline{v}(t_i)\underline{v}^T(t_j)\} = \underline{R}\delta_{ij}$

and $\underline{P} \equiv$ state covariance (uncertainty) matrix defined as the matrix of products from $P_{ij} = r_{ij}\sigma_i\sigma_j$, r_{ij} defined as the correlation coefficient which is equal to one for $i=j$, and σ defined as the standard deviation of the appropriate state

With these defined, the linear measurement model for the proposed correlator/filter tracker can be defined.

For this effort, the measurement update model is defined as

$$\underline{z}(t_i) = \underline{H}\,\underline{x}_F(t_i) + \underline{v}(t_i) \qquad (4\text{-}4)$$

where

$$\underline{H} = \begin{bmatrix} 1 & 0 & 0 & 0 & 0 & 0 & 1 & 0 \\ 0 & 1 & 0 & 0 & 0 & 0 & 0 & 1 \end{bmatrix} \qquad (4\text{-}5)$$

Definition of the model in this manner yields the Kalman filter measurement update equations in linear form. Specifically, these are

$$\underline{K}(t_i) = \underline{P}(t_i^-)\underline{H}^T\left[\underline{H}\,\underline{P}(t_i^-)\underline{H}^T + \underline{R}(t_i)\right]^{-1} \qquad (4\text{-}6)$$

$$\hat{\underline{x}}_F(t_i^+) = \hat{\underline{x}}_F(t_i^-) + \underline{K}(t_i)\left[\underline{z}(t_i) - \underline{H}\,\hat{\underline{x}}_F(t_i^-)\right] \qquad (4\text{-}7)$$

$$\underline{P}(t_i^+) = \underline{P}(t_i^-) - \underline{K}(t_i)\underline{H}\,\underline{P}(t_i^-) \qquad (4\text{-}8)$$

where $\underline{H}$, as in Equation (4-4), is defined to be time-invariant.

Since Equations (4-6) through (4-8) are to be wholly implemented within the optical Kalman filter (OKF) described in Chapter V, no further differentiation of filter measurement update operation is required. However, a statistical characterization of $\underline{v}(t_i)$ must be accomplished in order to specify the model upon which the update equations are based completely.

64

Previous work in this area (21,23) has characterized these statistics for correlator threshold fractional values of 0.3 and 0.5. Since a threshold fractional value of 0.3 is defined for this research, only statistics for this case are reported. Figures 26 and 27 thus represent previously obtained (21) error histograms for the correlation errors produced by the correlator described in Chapter III.

These error histograms were obtained in the following manner. An offset between the target and template of 0.15 pixels was selected as being representative of the antici- pated propagation error of the filter. Two sets of 1000 runs each were executed in software (one for the single hot spot case and the other for the multiple hot spot case) to develop the correlator statistics for this offset error. Each set used the truth model developed in Chapter II to provide the true trajectory information, resulting FLIR intensity pattern, background noises (allowed to vary over the full range of signal-to-noise ratios of 10 to 20), and FLIR noises due to the spatial correlation betweening adjoining pixels. The offset error thus defined is the deviation of the offset produced by the correlator from the correct value of 0.15 pixels. The offset error produced by each run was collected and placed in a bin which is 0.01 pixels wide and within -0.2 pixels to +0.4 pixels of the true offset. Each histo- gram thus depicts the total number of times (out of 1000) that the error corresponding to each bin was observed for the case identified. The statistics (in pixels) produced by these simulations are listed in Table I.

Table I. Correlation Errors

Target Type	Mean Error (α Offset)	Std. Dev (α Offset)	Mean Error (β Offset)	Std. Dev (β Offset)
Single Hot Spot	-.00113	.13262	-.00117	.13374
Three Hot Spot	-.00053	.03858	.00225	.05428
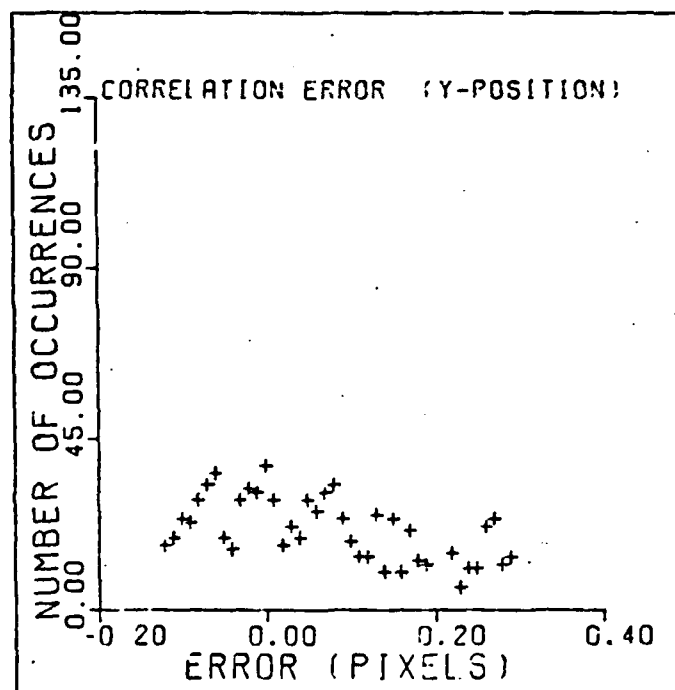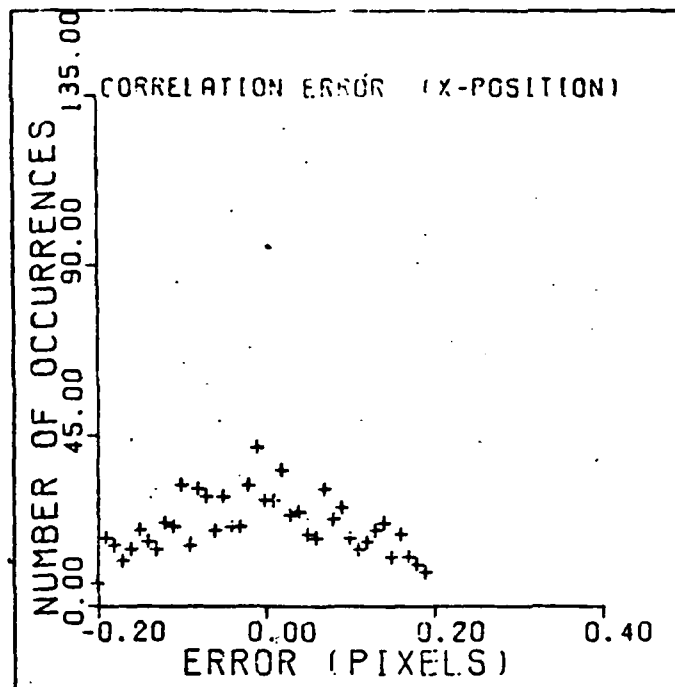
Figure 26 - Histogram of Errors-FFT Method
(Threshold = .3, One Hot Spot)
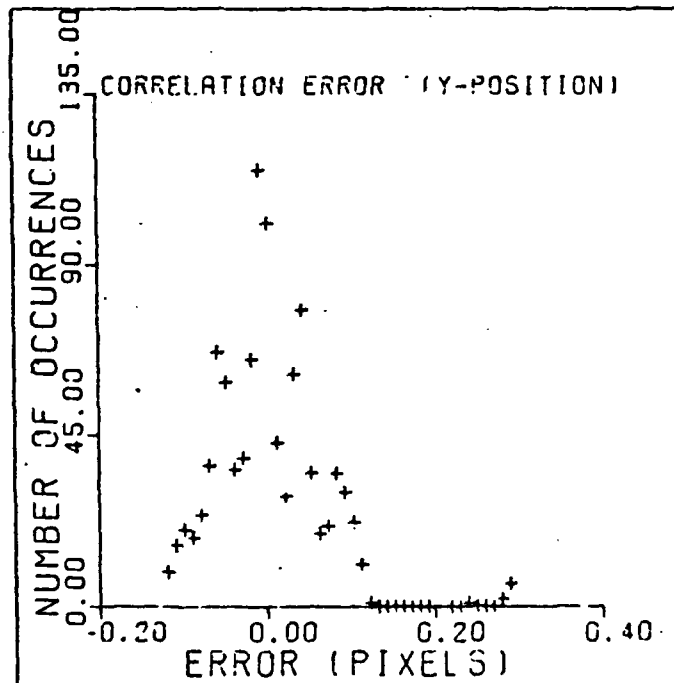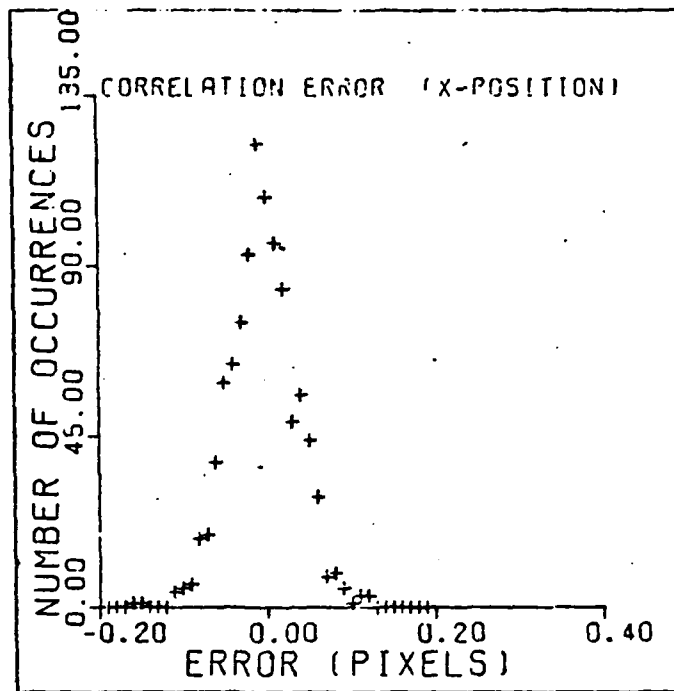
Figure 27 - Histogram of Errors - FFT Method
(Threshold = .3, Three Hot Spots)

Use of the values contained in Table I yields (since the errors in each FLIR dimension are independent of each other)

$$\underline{R}(t_i) = \begin{bmatrix} .01759 & 0 \\ 0 & .01789 \end{bmatrix} \quad (4-9)$$

for the single hot spot case, and

$$\underline{R}(t_i) = \begin{bmatrix} .00149 & 0 \\ 0 & .00295 \end{bmatrix} \quad (4-10)$$

for the three hot spot case. Since, as outlined earlier, these statistics were generated over a large number of runs which used the full range of anticipated conditions for the simulation, the resulting matrices of Equations (4-9) and (4-10) can be assumed representative for each type of target defined in Chapter II as long as the remainder of the conditions specified for the truth model are not violated.

Examination of these statistics reveals three important points. First, it is obvious that both $\underline{R}(t_i)$ matrices are required in the analysis. Thus, the tracker must be told the type of target it is to track along with the initial position data. Secondly, it is also easy to see from the error analysis that $\underline{R}(t_i)$ is time-invariant given the methodology used to develop the statistics. Lastly, the degree of difference between the two FLIR dimension error uncertainties for the three hot spot case warrants explanation. Here, this effect is due to the fact that a three hot spot target, as developed in Section 2.5 of this thesis, would have an intensity pattern which is not radially symmetric about the center of the FLIR image if it is projected so that the COM of its intensity profile is at the center of the FLIR. With these three points clarified, the entire measurement update model and its resulting filter equations are defined for the targets as specified by the truth model of Chapter II.

The system dynamics model used by the filter must now be defined. This model, outlined in the final section of this chapter, takes the enhanced state estimate vector and the

enhanced state covariance matrix, $\hat{\underline{x}}_F(t_i^+)$ and $\underline{P}(t_i^+$

gates them forward based on its knowledge (and th

uncertainty of this knowledge) of the system dyna

$\hat{\underline{x}}(t_{i+1}^-)$ and $\underline{P}(t_{i+1}^-)$ at the next sample period. T

keeps repeating until weapon operation ceases. T

this propagation to the next sample period has be

the tracker algorithm itself is fully defined.

4.3 System Dynamics Model

In contrast to the previously used first-ord

Markov linear target acceleration model, the cons

rate target acceleration model considers the targ

after projection onto the FLIR image plane, to be

modelled as constant-speed, constant turn-rate ma

The nonlinearity in this model arises from the de

of the target's jerk level motion (the time deriv

acceleration).

Specifically, the CTR target acceleration dy

(5,8,18,29) is

$$\underline{a} = - \quad \underline{v} + \underline{w}_F$$

which implies a state differential equation

$$\dot{\underline{x}}_F(t) = \underline{f}\left[\underline{x}_F(t),t\right] + \underline{G}_F \underline{w}_F(t)$$

where

$$\underline{f} = |v_\alpha(t) \ v_\beta(t) \ a_\alpha(t) \ a_\beta(t) \ -\omega^2(t)v_\alpha(t) \ -\omega^2(t)\cdot$$
$$(-1/\tau_{AF})\alpha_A(t) \ (-1/$$

$$\underline{G}_F\underline{w}_F(t) = |0 \ 0 \ 0 \ 0 \ w_{DF}(t) \ w_{DF}(t) \ w_{AF}(t) \ w_{AF}(t)|$$

$$\omega = \frac{|\underline{v} \times \underline{a}|}{|\underline{v}|^2} = \frac{|v_\alpha a_\beta - v_\beta a_\alpha|}{v_\alpha^2 + v_\beta^2}$$

and where

$\underline{f}\left[\underline{x}_F(t),t\right] \equiv$ the nonlinear system dynamic

of the filter states

$\omega \equiv$ the target's turn-rate on th

image plane

$\underline{w}_F$ ≡ zero mean, white, Gaussian noise composed of both filter target dynamics model uncertainties (subscript DF) and filter atmospheric model uncertainties (subscript AF) common to both FLIR plane dimensions with statistics developed by tuning

$\underline{G}_F$ ≡ dynamics driving noise input matrix

and τ_{AF} ≡ correlation time assumed by the filter for the atmospheric jitter

Note that this preserves the original state matrix definition expressed in Equation (4-3).

The statistics of the noise vector are

$$E\{\underline{w}_F(t)\underline{w}_F^T(t+\tau)\} = \underline{Q}_F\delta(\tau) \qquad (4\text{-}13)$$

where $\underline{w}_F(t)$ is defined as a four-element column vector for $\underline{G}_F$ defined as

$$\begin{bmatrix} \underline{0}_{4\times4} \\ --- \\ \underline{I}_{4\times4} \end{bmatrix}$$

Definition in this manner yields the 4x4 $\underline{Q}_F$ matrix as

$$\begin{bmatrix} \sigma_{DF}^2 & 0 & 0 & 0 \\ 0 & \sigma_{DF}^2 & 0 & 0 \\ 0 & 0 & 2\sigma_{AF}^2/\tau_{AF} & 0 \\ 0 & 0 & 0 & 2\sigma_{AF}^2/\tau_{AF} \end{bmatrix}$$

where

σ_{DF}^2 ≡ the assumed target jerk level motion white process power spectral density value

and σ_{AF}^2 ≡ the assumed atmospheric jitter Markov-1 process variance

From the model, the equations necessary to propagate the state estimates and state estimate uncertainties forward in time (to the next sample period) are developed. In discrete

70

time, the general form of the state estimate propagation is

$$\underline{\hat{x}}_F(t_{i+1}^-) = \underline{\hat{x}}_F(t_i^+) + \int_{t_i}^{t_{i+1}} \underline{f}\left[\underline{\hat{x}}_F(t|t_i),t\right] dt \qquad (4\text{-}14)$$

where here the nonlinear system dynamics function is conditioned on time t_i. If a first-order Euler integral approximation to Equation (4-14) is used over the interval $\Delta t = t_{i+1} - t_i$, the expression

$$\underline{\hat{x}}_F(t_{i+1}^-) = \underline{\hat{x}}_F(t_i^+) + \underline{f}\left[\underline{x}_F(t_i^+),t_i\right]\Delta t \qquad (4\text{-}15)$$

can be used for a Δt which is sufficiently small when compared to the natural transient times of the physical system. As such is the case here, Equation (4-15) is totally computed in software to produce the state estimate propagation. This will be further discussed in Chapter V where the method of filter operation is discussed in terms of efficiency.

Similarly, the covariance propagation (state estimate uncertainty propagation) must also be written in terms of the most recent state estimates since

$$\underline{F}(t_i) = \partial\underline{f}\left[\underline{x},t\right]/\partial\underline{x} \Big|_{\underline{x} = \underline{\hat{x}}_F(t_i^+)} \qquad (4\text{-}16)$$

is no longer known a priori as it would be in a linear filter. The definition of $\underline{F}(t_i)$ in Equation (4-16) as a piecewise constant function again is valid due to the relative rates of variation of $\underline{F}(t_i)$ with Δt.

The standard linear covariance propagation equation can thus be used with the restriction that the parameters of interest be recalculated each sample period. Specifically, this equation is

$$\underline{P}(t_{i+1}^-) = \underline{\Phi}_F(t_{i+1},t_i)\underline{P}(t_i^+)\underline{\Phi}_F^T(t_{i+1},t_i) + \underline{Q}_{FD}(t_{i+1},t_i) \qquad (4\text{-}17)$$

where the variables of interest are developed as follows. Using the same first-order Euler approximation as in the state estimation propagation development,

$$\underline{\Phi}_F(t_{i+1},t_i) = \exp\left[\underline{F}(t_i)\Delta t\right] \qquad (4\text{-}18)$$

For the nonlinear system dynamics function specifically defined by Equation (4-12), it can readily be seen that calculation of $\underline{\Phi}_F(t_{i+1},t_i)$ using the strict interpretation of

Equation (4-18) would impose a large computational burden on the system. This is particularly true since it is to be done in software. However, a careful analysis of the matrices of Equation (4-17) reveals that any terms not on the diagonal of $\underline{\Phi}_F$ will have zero contribution to $\underline{P}$. This is because $\underline{P}$ itself is diagonal due to the independence of all of the system uncertainties with each other. With this knowledge, the upper left 6x6 portion of the matrix is truncated to first-order terms, resulting in the expression

$$\underline{\Phi}_F(t_{i+1}, t_i) = \underline{I} + \underline{F}(t_i)\Delta t \qquad (4\text{-}19)$$

The balance of $\underline{F}(t_i)$, being associated with the two atmospheric states, is time-invariant and can be determined in its exact closed form. Appendix B provides a full analysis of this development.

For the same reasons, the $\underline{Q}_{FD}$ matrix is also simplified. Formally, its definition is

$$\underline{Q}_{FD}(t_{i+1}, t_i) = \int_{t_i}^{t_{i+1}} \underline{\Phi}_F(t_{i+1}, \tau)\underline{G}_F\underline{Q}_F(\tau)\underline{G}_F^T\underline{\Phi}_F^T(t_{i+1}, \tau) \, d\tau \quad (4\text{-}20)$$

which must be recalculated every sample period since the $\underline{F}$ upon which $\underline{\Phi}$ is based is not known a priori. However, since the time interval Δt is short compared to the system transients, previous research has shown (8,29) that the definition

$$\underline{Q}_{FD} = \underline{G}_F\underline{Q}_F\underline{G}_F^T\Delta t \qquad (4\text{-}21)$$

is valid for the filter specified. Given the structures already identified for both $\underline{Q}_F$ and $\underline{G}_F$, it is obvious that once the values are specified (through tuning) for $\underline{Q}_F$, $\underline{Q}_{FD}$ becomes constant with values of $\underline{Q}_F\Delta t$.

Processing of the filter's propagation cycle is thus accomplished by using software to execute Equations (4-16) and (4-19) on an iterative basis. Software will also be used to calculate all constant values initially upon each operation of the tracker. The OKF will then implement Equation (4-17) to provide the state estimate covariance propagation.

With these developments, the entire tracker has been
mathematically specified. The remaining task of this thesis
prior to analyzing the tracker's performance is the complete
development of the optical Kalman filter. The next chapter
is devoted to this requirement, as well as tieing the entire
system together in a cohesive form prior to its analysis.

V.   Optical Kalman Filter

5.1   Introduction

With the filter models fully developed and analyzed, the method of implementation of the filter algorithms must be completely described and characterized. This requirement is particularly true given the optical nature of the proposed solution. The processor analysis must consider the accuracy of the results generated by the optical bed versus those produced by a software implementation (given the accuracy required by the problem dynamic range) in addition to system throughput considerations. Successful demonstration of specification compliance will thus constitute satisfaction of the major basis of this thesis.

Several optical architectures were considered as candidates for the optical processor. However, the tradeoff analyses outlined in Chapter I which resulted in the choice of the pipelined iterative optical systolic array architecture are negligible compared to both a description of the architecture itself and the way the architecture implements the operations required to perform the filter algorithms. For this reason, the discussions of this chapter are limited to these areas and the required analyses thus generated.

To accomplish these developments in the most logical manner, the initial thrust of this chapter (Section 5.2) will be limited to development of the optical architecture and its method of implementing the operations required by the general Kalman filter algorithm. To maintain a level of presentation sufficiently basic to allow understanding by engineers unfamiliar with optics, device physics will not be fully developed within the section but will be referenced for optional study. Experienced optical engineers may wish to substitute Reference 2, upon which this architecture is based, in lieu of this section.

74

The final section of this chapter contains all the analyses required to demonstrate processor specification compliance after all of the specific real-world components have been identified and characterized. Sufficient analyses are provided to present a clear comparison between the proposed optical approach and a software implementation of the filter algorithms developed in Chapter IV.

5.2 Pipelined Iterative Optical Systolic Array Development

The decision to employ an optical processor as the solution of choice is chiefly due to the inherent ability of optical components to handle a large degree of data in parallel without requiring component duplication. The particular architecture selected, the pipelined iterative optical systolic array, fully exploits this capability as well as exploiting the advantages presented by data pipelining and the iterative nature of the process itself.

Prior to developing the architecture, clarity requires that each optical device type used within the architecture be fully characterized in order to illustrate clearly the data flow through the assembled architecture. Since the architecture itself is extremely simple, only four optical devices require characterization: light sources, acousto-optic light modulators (AOMs), simple lenses, and optical detectors. The description of each particular device's characteristics will be presented in the order of their occurrence in the architecture and will be tied back to the previous device characteristic descriptions so as to maintain a logical data flow which is easily relatable to the overall architecture.

The first optical component type required by the architecture is a linear array of light sources in order to produce a parallel signal representation in the optical domain. This linear array requirement, as well as the size constraints imposed by the modulator (as will be seen), limits the choice of optical components to two distinct but related semiconductor device types (25,28,30), either light emitting diodes

(LEDs) or laser diodes (LDs), combined as discrete units or
a prepackaged array. While this limitation may appear to be
severe, the range of options available to the system archi-
tect is actually quite large.

LEDs are classified as incoherent sources of light and
are available in a wide range of maximum average power levels,
continuous wave and pulsed operational modes, and output
bandwidths (light spectral content, pulse repetition rate,
and pulse width). However, their incoherency, an output
distributed over some range of light frequencies, produces
five inherent device limitations. These limitations are
directly related to the light frequency range of the device
and can limit their applicability in optical processing
architectures. These limitations include constraints on
(1) the maximum pulse repetition rate and (2) the minimum
pulse width of the device. The component density is also
limited since (3) an LED's projected field of view is much
greater than that of a coherent source. Additionally, these
devices are highly susceptible to (4) spatial and (5) spectral
output variations over time due to thermal effects, although
these drawbacks can be somewhat mitigated by cooling. Despite
the fact that these limitations do sometimes prevent the use
of LEDs in optical architectures, use of these devices is as
often mandated (although not in this case) by their advantage
in available maximum average output power over other semicon-
ductor source types.

Laser diodes, on the other hand, are coherent devices
since they employ an actual laser cavity to produce light.
Cavity losses, principally the extinction of frequencies
not harmonic to the cavity, thus limit their maximum average
output power, particularly when compared to LEDs having
identical active regions in both size and material. Although
this limitation sometimes is a serious drawback to their use
in optical architectures, the fact that the coherency of a
LD allows extremely narrow pulse widths resulting in high
peak power outputs permits their use in the majority of

non-integrating architectures. Additional benefits as-
cribable to coherency include greater pulse repetition rates,
greater device density due to the much narrower projected
FOV, and minimization of thermal effects due to their ability
to maintain a coherent output. For these reasons, LDs are
often the only sources available for high-speed optical pro-
cessing applications.

Either of these device types, when configured in a lin-
ear array, formulate a parallel representation in a spatial
sense of either a group of analog values or a digital bit
stream. Since the projected paths of the signals formulated
by these devices are parallel or at least separated over the
region of interest, as illustrated in Figure 28, modulation
of the values represented by each light source can also occur

Light
Producing
Areas

Maximum Usable Range

(a)

Light
Producing
Areas

(b)
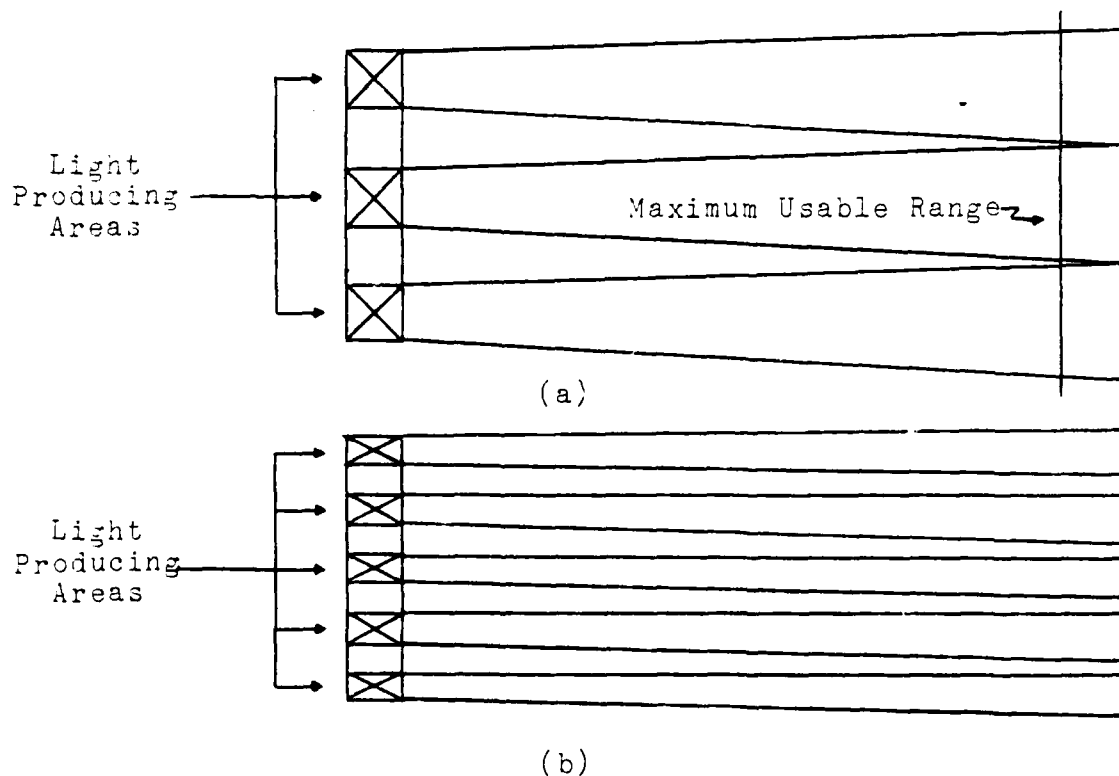
Figure 28 - Parallel Spatial Sense Signal Representation
in (a) LEDs (b) LDs

77

in parallel. For the architecture chosen, this modulation, as noted in Chapter I, is accomplished through use of a single AOM (30).

The first requirement for modulating a spatially parallel signal representation is that the signal loaded into the mod-ulator be spatially matched to the input signal produced by the LED/LD array. In an AOM, this is accomplished by serially injecting a series of bulk acoustic waves (discrete frequency packets) into a crystal which has been carefully oriented along a specific crystal axis. These injected discrete fre-quency packets are often separated by nulls, as illustrated in Figure 29, to preclude crosstalk between values, and have power levels corresponding to each particular value. But
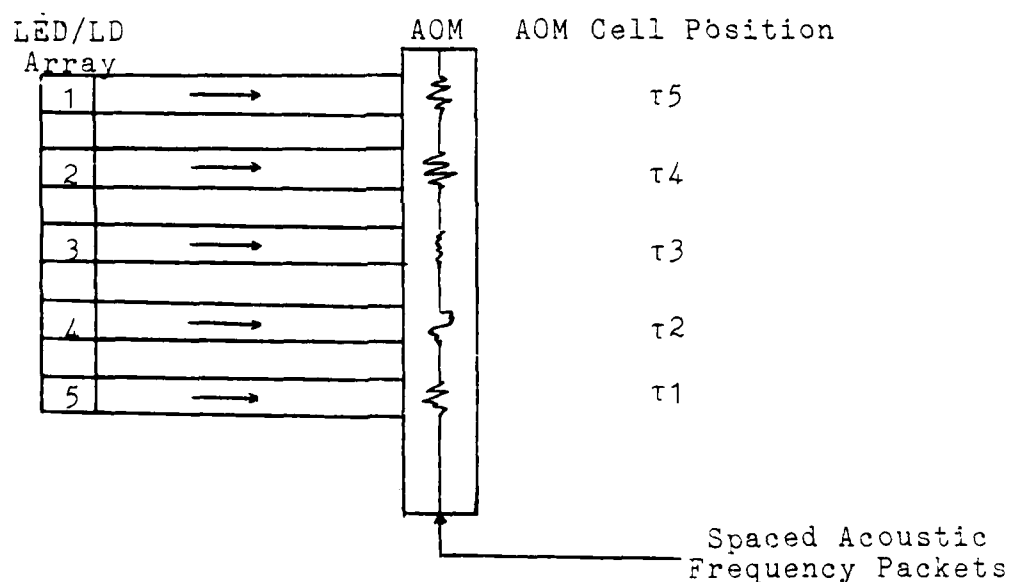
Figure 29 - Matched Parallel Signal Representation

AOMs inherently possess two serious limitations which must be overcome. These are acoustic attenuation within the crystal and the acoustic beam spread as a function of propagation.

These two limitations present a number of tradeoff con-siderations to the architect. However, the limitation im-posed by acoustic attenuation can be overcome by using a

source (LD or LED) which has sufficient output power both to represent the signal input to it accurately and to compensate for the attenuation of the signal in the AOM. This, of course, presupposes that the system throughput rate combined with the velocity of sound (v_s) in the AOM produces a working aperture (spatial extent of the parallel representation) which is of sufficient size to accommodate the required source devices. Additionally, the choice of crystal and crystal axis determines to some extent the degree of correction obtainable to counter the acoustic beam spread limitation. This is due to the fact that choice of transducer geometry only collimates (forms a spatially parallel representation of) the propagation vectors of the acoustic waves at the AOM input and does not affect distortion caused by the sources identified above.

Assuming for the moment (until satisfactory demonstration in Section 5.3) that these limitations have been overcome so that the AOM output response is flat across the entire working aperture (i.e., the response to a unit input to both the AOM and each element of the LED/LD array is uniform across the entire spatial representation of the AOM output), the process of analog multiplication is described. Recall that the bulk acoustic waves are amplitude modulated (in terms of acoustic power per unit area) discrete frequency packets which propagate along the longitudinal axis of the AOM as illustrated in Figure 29. Then for any specified acoustic bandwidth each discrete frequency packet can be composed of a superposition of several amplitude modulated frequencies. Each acoustic frequency (ω_s) present within the AOM can then interact with the input light frequency (ω) in the following manner.

Restricting for the moment the modulating frequency to the AOM acoustic center frequency, a Bragg diffraction condition (30) is purposely implemented as illustrated in Figure 30. In terms of the wavelengths involved, this Bragg condition
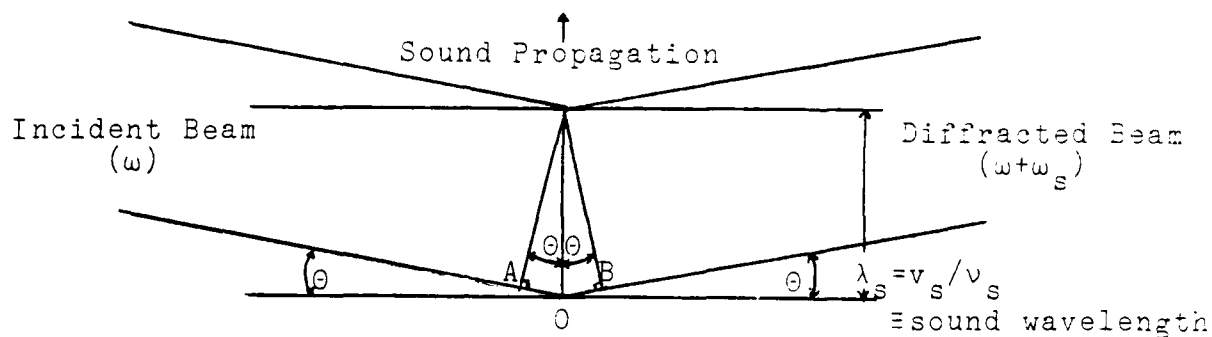
Figure 30 - AOM Bragg Diffraction Condition

exists when the path length AO+OB is equivalent to the optical wavelength within the crystal (the free space wavelength, λ, divided by the crystal's index of refraction, n). Since

$$AO = OB = \lambda_s \sin \Theta = \lambda/2n \qquad (5-1)$$

where λ_s is the wavelength of the acoustic wave within the crystal, the precomputable Bragg angle required to set up the diffraction is

$$\Theta = \sin^{-1}\left[\frac{\lambda}{2n\lambda_s}\right] = \sin^{-1}\left[\frac{\lambda\nu_s}{2nv_s}\right] \qquad (5-2)$$

since λ_s is defined as the velocity of sound in the crystal (v_s) per unit sound frequency (ν_s). In terms of frequency, the diffracted beam's angular propagation (vector) characteristic is now described by $\omega+\omega_s$. Relaxing the fixed frequency assumption, the relationship [with the input Bragg angle as defined in Equation (5-2) maintained] reduces to

$$\Delta\Theta = \frac{\lambda}{nv_s}\Delta\nu_s \qquad (5-3)$$

where $\Delta\nu_s$ is the difference between the input sound frequency and the acoustic center frequency and $\Delta\Theta$ is the resulting angular output difference from the Bragg angle (30). Noting that $\Delta\nu_s$ can be either positive or negative, each discrete sound frequency packet input to the AOM spatially modulates the

80

incident light over an angular range defined by the AOM
acoustic bandwidth. This is expressable as

$$\frac{I_{Diffracted}}{I_{Incident}} = \sin^2\left[\frac{0.6328\sqrt{2}}{\lambda}(\ell)\sqrt{M_\omega I_{Acoustic}}\right] \quad (5-4)$$

where

$I_{Diffracted}$ ≡ diffracted light exitance (emitted power per unit area)

$I_{Incident}$ ≡ incident light irradiance (power per unit area onto a surface)

$\frac{I_{Diffracted}}{I_{Incident}}$ ≡ diffraction efficiency of the AOM or the Bragg efficiency

λ ≡ wavelength of light in um

ℓ ≡ the acoustic interaction length (generally taken to be the width of the acoustic beam through which light would pass if it were input perpendicular to the direction of acoustic propagation)

M_ω ≡ the diffraction figure of merit of the crystal relative to water

and $I_{Acoustic}$ ≡ acoustic intensity within the crystal (acoustic power per mm^2 area)

As the input light intensities are also amplitude modulated,
it is easy to see that for the analog case it is the indivi-
dual products of the values represented by the incident light
power and each of the frequencies present in the discrete
frequency packet that are angularly separated, whereas for
the digital case, multiple two-bit AND functions are pro-
duced. Since this occurs at every modulation point in the
AOM parallel representation, discrimination between products
is impossible without further spatial modulation. In the
chosen architecture, this required spatial modulation is
accomplished by a simple lens.

Although commonly thought of as chiefly of use in imaging, the simple lens (6,30) has the additional capability of producing a phase-flat Fourier transform in the time it takes light to transit twice the lens focal length. For example, given a 500mm focal length lens, the time required to produce a Fourier transform of a spatial frequency expressed input waveform is

$$t = 2f/c = 1m/3x10^8 \text{ m/sec} = 3.3\overline{3} \text{ nsec} \qquad (5-5)$$

Since each diffracted order (i.e., each distinct angular propagation vector) is the optical equivalent of a distinct frequency, a lens will focus any modulation products having the same angular orientation to the same point in space as illustrated in Figure 31. This important property of a lens
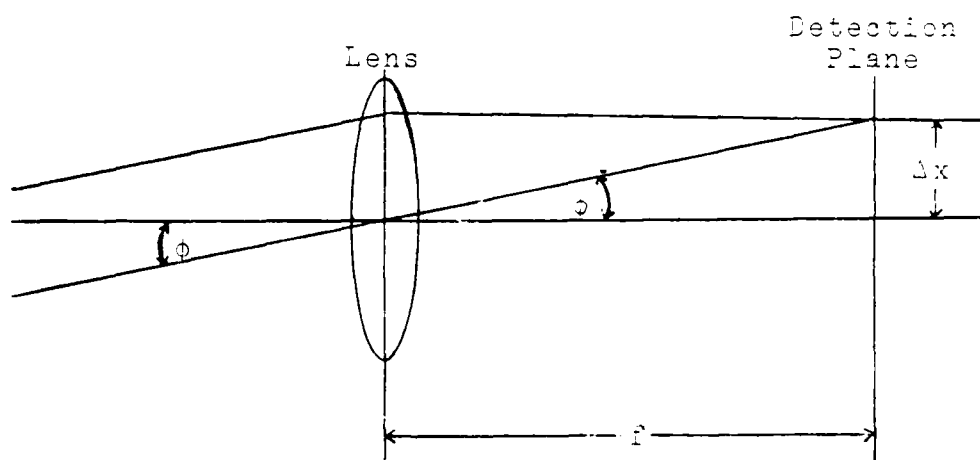
Figure 31 - Deflection of a Ray by a Simple Lens

thus allows sums of products to be formulated in parallel. When combined with the superposition abilities of an AOM, it is easy to see that a number of product sums can be formulated in parallel. The separation between these sums at the detection plane thus becomes only a function of the frequency differences which are input into the AOM. By defining the slope of the input ray as the tangent of the angle ϕ, the separation between products is

$$\Delta x = f \tan \phi \qquad (5-6)$$
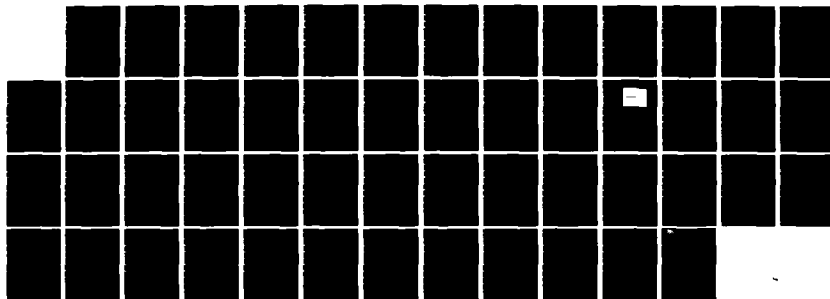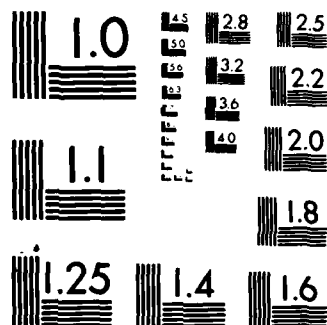
MICROCOPY RESOLUTION TEST CHART

NATIONAL BUREAU OF STANDARDS-1963-A

Thus, for the case of a lens oriented so that its diameter is perpendicular to the propagation vector (from an AOM) resulting from the Bragg angle and having all products modulated using either positive or negative multiples of a fixed frequency $\Delta\nu_s$ about the AOM acoustic center frequency, the separation between any two product sums is expressible as

$$\Delta x = f\ \tan\ \Delta\Theta \qquad\qquad (5\text{-}7a)$$

$$= f\ \tan\left[\frac{\lambda}{n\nu_s}\right]\Delta\nu_s \qquad\qquad (5\text{-}7b)$$

where the multiples of $\Delta\nu_s$ over the product sum range are only constrained by the AOM acoustic bandwidth.

There are, however, some constraints for the utilization of these relationships. Since they are based on thin lens formulae, the lens diameter must be oriented perpendicular to the Bragg angle Θ to produce the $\Delta\Theta$ relationship expressed in Equation (5-7) accurately. Additionally, due to lens aberration properties, minimization of error is achieved only when the inner portion (roughly corresponding to the semi-circle described by half the lens diameter) of the lens is used and the lens F-number (lens focal length divided by the lens diameter) is relatively high ($\geq f/4$) to preclude the effects of large angles. Moreover, all of these constraints become increasingly more difficult to satisfy as the system throughput rate and/or array size is increased.

Now that the specific product sums have been focused at the same point in space, a linear detector array (25,28,30) is required to convert the optical signal back into an electronic signal accurately. Due to size constraints, the choice is limited to semiconductor devices, where the parameters of interest are the device quantum efficiency for the particular light wavelength used, the device minimum detectable power, and the maximum (or saturation) power of the device. Since the final two parameters are directly related to the size of the device's active area, the major constraint is once again maintaining sufficient lateral separation to accomodate component size.

83

With the devices incorporated within the architecture defined, a step-by-step development of the linear algebra operations required for a Kalman filter algorithm must be accomplished. Although only illustrated here for square matrices and vectors of dimension three, the architecture and processing steps are directly expandable to any higher dimension within the aforementioned component constraints.

The least complex linear algebra required for a Kalman filter is the formation of a matrix-vector product, expressible as

$$\begin{bmatrix} a_{11} & a_{12} & a_{13} \\ a_{21} & a_{22} & a_{23} \\ a_{31} & a_{32} & a_{33} \end{bmatrix} \begin{bmatrix} b_1 \\ b_2 \\ b_3 \end{bmatrix} = \begin{bmatrix} c_1 \\ c_2 \\ c_3 \end{bmatrix} \qquad (5\text{-}8)$$

Using the architecture as illustrated in Figure 32 (with the Bragg angle not depicted for clarity) and superimposing the matrix column values in the sequence outlined in Table II, the complete matrix-vector product is available in $(2N-1)$ time intervals for a matrix of dimension MxN and a vector of dimension N. For tabular purposes, AOM modulation frequencies are expressed as diffraction orders where each full diffraction order is defined to be a multiple of $\Delta\nu_s$ about the AOM acoustic center frequency. Thus for an odd number of superimposed frequencies, the diffraction orders are expressed as

$$0, \pm 1, \pm 2, \pm 3, \ldots, \pm \frac{(S-1)}{2}$$

where S is the number of superimposed frequencies, whereas for the case of an even number of superimposed frequencies, the diffraction orders are

$$0, \pm 0.5, \pm 1.5, \pm 2.5, \ldots, \pm \frac{(S-1)}{2}$$

Use of this technique maintains a symmetric diffraction pattern about the AOM acoustic center frequency and thus minimizes potential error sources as well as maintaining the

84

Table II. Matrix-Vector Formation Sequence

Time	Actions	Outputs
T1	a_{11} at +1, a_{21} at 0, and a_{31} at -1 input to AOM at τ_1	
T2	1st column of $\underline{A}$ propagates to τ_2 2nd column of $\underline{A}$ input to AOM @ τ_1 using same superposition frequencies	
T3	1st column of $\underline{A}$ propagates to τ_3 2nd column of $\underline{A}$ propagates to τ_2 3rd column of $\underline{A}$ input to AOM @ τ_1 using same superpostion frequencies	
T4	1st column of $\underline{A}$ propagates to τ_4 2nd column of $\underline{A}$ propagates to τ_3 3rd column of $\underline{A}$ propagates to τ_2	
T5	1st column of $\underline{A}$ propagates to τ_5 2nd column of $\underline{A}$ propagates to τ_4 3rd column of $\underline{A}$ propagates to τ_3 b_1 input to LED/LD 1 b_2 input to LED/LD 2 b_3 input to LED/LD 3	c_1 c_2 c_3

relationship expressed in Equation (5-7b). Therefore, in
Table II (and other appropriate tables in this section),
"a_{11} at +1" means "a_{11} at diffraction order +1" or a_{11} at
a frequency of $\nu_s + (1)\Delta\nu_s$", and so forth.

Note: Drawing Not to Scale
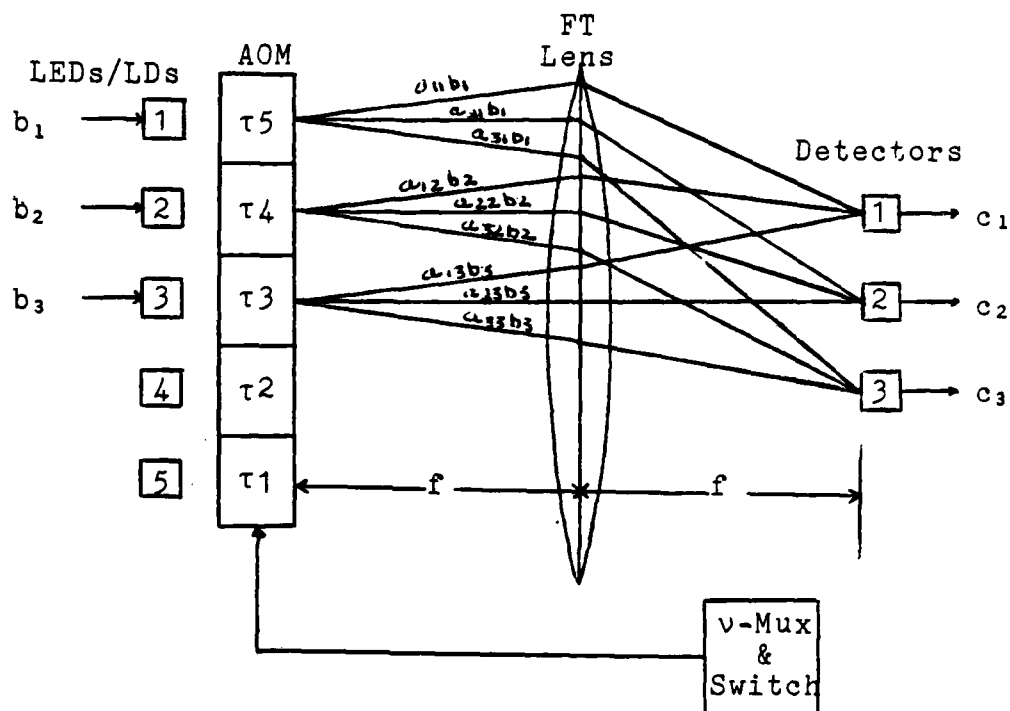
Figure 32 - Matrix-Vector Multiplication (at t=T5)

Although it can be readily seen that a matrix-vector
product could be available at either T3, T4, or T5, use of
the same architecture for matrix-matrix or higher order
operations requires the timing illustrated. This can be
demonstrated by merely tabulating the required operations
for matrix-matrix multiplication (here $\underline{A}\,\underline{B} = \underline{C}$) by the same
architecture. This process, illustrated by the combination
of Table III and Figure 33a-c, again requires only (2N-1)
time intervals to produce the desired outputs. In general,
the multiplication of two matrices of dimensions (MxN) and

Table III - Matrix-Matrix Multiplication Sequence

Time	Actions	Outputs
T1	1st column of $\underline{A}$ input to AOM @ τ_1 using same superposition frequencies as matrix-vector case	
T2	1st column of $\underline{A}$ propagates to τ_2 2nd column of $\underline{A}$ input to AOM @ τ_1 using same superposition frequencies	
T3	1st column of $\underline{A}$ propagates to τ_3 2nd column of $\underline{A}$ propagates to τ_2 3rd column of $\underline{A}$ input to AOM @ τ_1 using same superposition frequencies b_{11} input to LED/LD 3 b_{21} input to LED/LD 4 b_{31} input to LED/LD 5	c_{11} c_{21} c_{31}
T4	1st column of $\underline{A}$ propagates to τ_4 2nd column of $\underline{A}$ propagates to τ_3 3rd column of $\underline{A}$ propagates to τ_2 b_{12} input to LED/LD 2 b_{22} input to LED/LD 3 b_{32} input to LED/LD 4	c_{12} c_{22} c_{32}
T5	1st column of $\underline{A}$ propagates to τ_5 2nd column of $\underline{A}$ propagates to τ_4 3rd column of $\underline{A}$ propagates to τ_3 b_{13} input to LED/LD 1 b_{23} input to LED/LD 2 b_{33} input to LED/LD 3	c_{13} c_{23} c_{33}

Note: Drawings Not to Scale
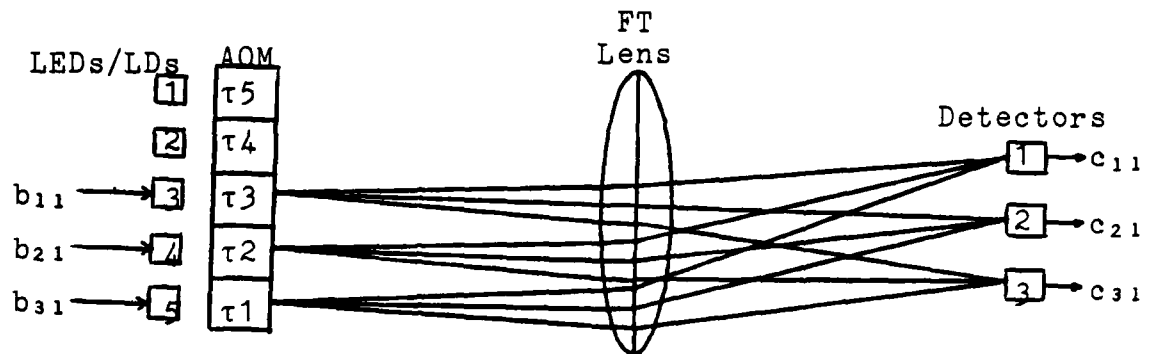
(a)
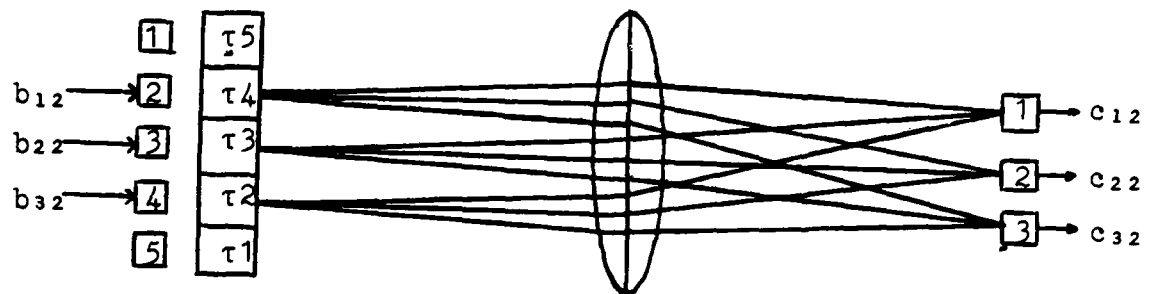
(b)
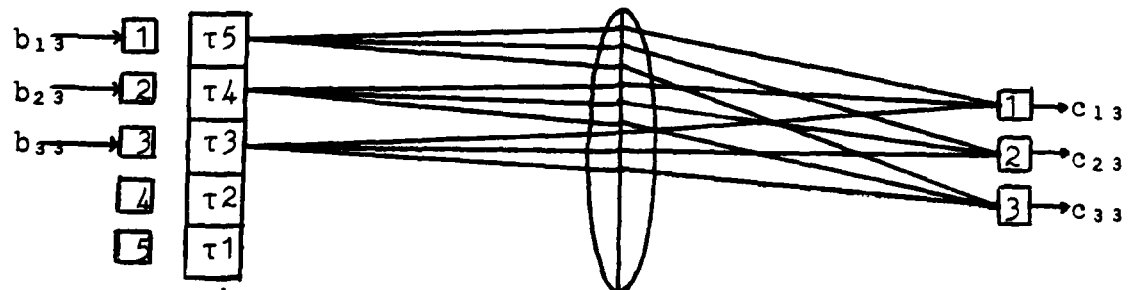
(c)

Figure 33 - Snapshots of Matrix-Matrix Product Formation
at (a) T3 (b) T4 (c) T5

(NxM) requires M frequencies, M detectors, (2N-1) LEDs/LDs, and (2N-1) time intervals of which (N-1) time intervals is dead or delay time.

If the linear algebra operations required by the Kalman filter algorithm were limited solely to the product formations already illustrated, architectural development could stop at this point. However, the necessity of being able to perform matrix-matrix-matrix multiplies and matrix inversions in an efficient manner requires the addition of three externally engageable electronic devices to the optics already illustrated. The efficiency requirement precludes repetition of matrix-matrix operations to accomplish these higher order operations if better alternatives are available.

For example, the architecture required to support matrix-matrix-matrix product formation is illustrated in Figure 34 and requires inclusion of a sample and hold (S/H) device in the added feedback loop. Noting that the optical bed is identical to those discussed previously, only a tabular summation of processing steps for the product $\underline{E} = \underline{A}\,\underline{B}\,\underline{D}$ (where $\underline{A}\,\underline{B} = \underline{C}$ and $\underline{E} = \underline{C}\,\underline{D}$) is presented in Table IV. From Table IV, it is obvious that the overall computation time required for the complete formation of $\underline{E}$ is $(3N-1)$ time intervals of which $(N-1)$ time intervals is again dead or delay time. Further matrix multiplications are also achievable using the same algorithm with each additional matrix requiring an additional N time intervals to form the complete product.

Rather than illustrating further pipelining beyond matrix-matrix-matrix multiplication, matrix inversion using the same optical package is outlined. Here, a modified Richardson algorithm (2) to solve $\underline{C} = \underline{H}\,\underline{B}$ for $\underline{B} = \underline{H}^{-1}\underline{C}$ without explicitly computing the matrix inversion $\underline{H}^{-1}$ is utilized. Use of this algorithm exploits the pipelined itera- tive nature of the algorithm as follows. Within this concept,

89
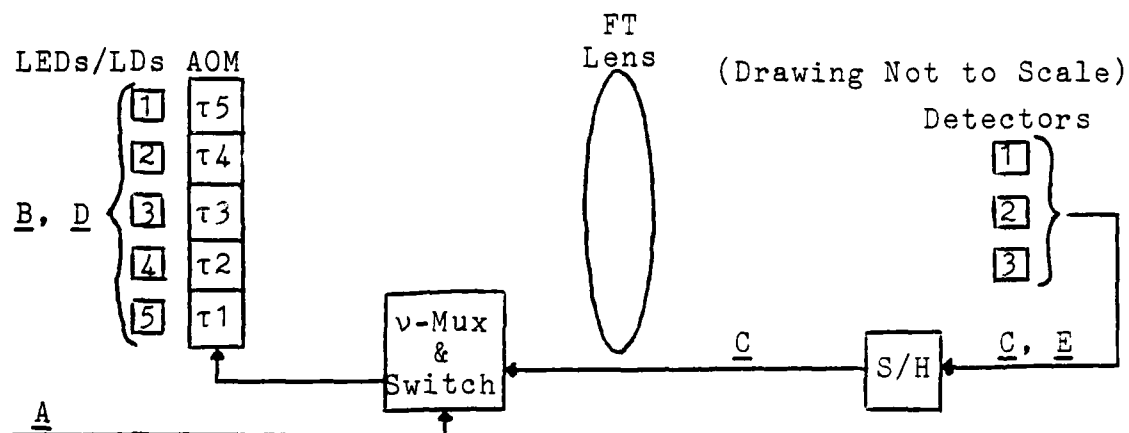
Figure 34 - Architecture for Matrix-Matrix-Matrix Multiplier

Table IV - Time History of Figure 34 Components

T1	T2	T3	T4	T5	T6	T7	T8	Parameter	Comments
a_{11}	a_{12}	a_{13}	c_{11}	c_{12}	c_{13}	-	-	+1	
a_{21}	a_{22}	a_{23}	c_{21}	c_{22}	c_{23}	-	-	0	C from Detectors
a_{31}	a_{32}	a_{33}	c_{31}	c_{32}	c_{33}	-	-	-1	
-	-	-	-	b_{13}	-	-	d_{13}	1	
-	-	-	b_{12}	b_{23}	-	d_{12}	d_{23}	2	
-	-	b_{11}	b_{22}	b_{33}	d_{11}	d_{22}	d_{33}	3	Inputs to LED/LDs
-	-	b_{21}	b_{32}	-	d_{21}	d_{32}	-	4	
-	-	b_{31}	-	-	d_{31}	-	-	5	
-	-	c_{11}	c_{12}	c_{13}	e_{11}	e_{12}	e_{13}	1	
-	-	c_{21}	c_{22}	c_{23}	e_{21}	e_{22}	e_{23}	2	Detector Outputs
-	-	c_{31}	c_{31}	c_{33}	e_{31}	e_{32}	e_{33}	3	

the iterative algorithm

$$\underline{B}_{k+1} = [\underline{I} - \omega \underline{H}]\underline{B}_k + \underline{C} \qquad (5-9)$$

is used where ω is the acceleration parameter that is chosen
to speed convergence of the algorithm. When the results
$\underline{B}_k = \underline{B}_{k+1}$ on two successive iterations k and k+1 are equal,
Equation (5-9) reduces to the solution

$$\underline{B} = \underline{H}^{-1}\underline{C} \qquad (5-10)$$

The full architecture, illustrated in Figure 35, realizes
the algorithm by modifying Equation (5-9) into

$$\underline{B}_{k+1}/\omega = [\underline{I}/\omega - \underline{H}]\underline{B}_k + \underline{C} \qquad (5-11)$$

where $[\underline{I}/\omega - \underline{H}]$ is electronically precalculated for efficiency.
Realizing that $\underline{H}$ is known and fixed and that $\underline{I}/\omega$ is easily
computable by a simple scaling of its elements, $[\underline{I}/\omega - \underline{H}]$
is thus written as a matrix $\underline{A}$ which is assumed known and
fixed for a given value of ω, yielding

$$\underline{B}_{k+1} = \omega [\underline{A}\,\underline{B}_k + \underline{C}] \qquad (5-12)$$

The optical system thus performs the matrix-matrix multipli-
cation $\underline{A}\,\underline{B}_k$, the matrix $\underline{C}$ is added one row at a time in real
time (in a resistive adder) to form $[\underline{A}\,\underline{B}_k + \underline{C}]$, and this matrix
summation is then electronically multiplied by ω as shown in
the figure to form the next $\underline{B}_{k+1}$ iterative input to the AOM.
Table V clearly shows the time history of the algorithm, where
for notational simplicity the initial k=0 matrix $\underline{B}_0$ is denoted
by elements b_{mn}, $\underline{B}_1$ by b'_{mn}, and $\underline{B}_2$ by b''_{mn}. As can be seen
in the table, the initial b_{mn} inputs to the AOM originate
from an initial estimate described in Reference 2 and there-
after all future AOM inputs come from prior iterations. This
again yields an ideal pipelining of operations as there is
no dead or delay time after the initial (N-1) AOM cell delay.
Given the filter matrices defined in Chapter IV, the only
inversion required for the problem of this thesis [Equation
(4-6)] is only of dimension (2x2). By defining $\underline{C} = \underline{I}_2$,
the $\underline{B}_0$ matrix and acceleration parameter ω are easily
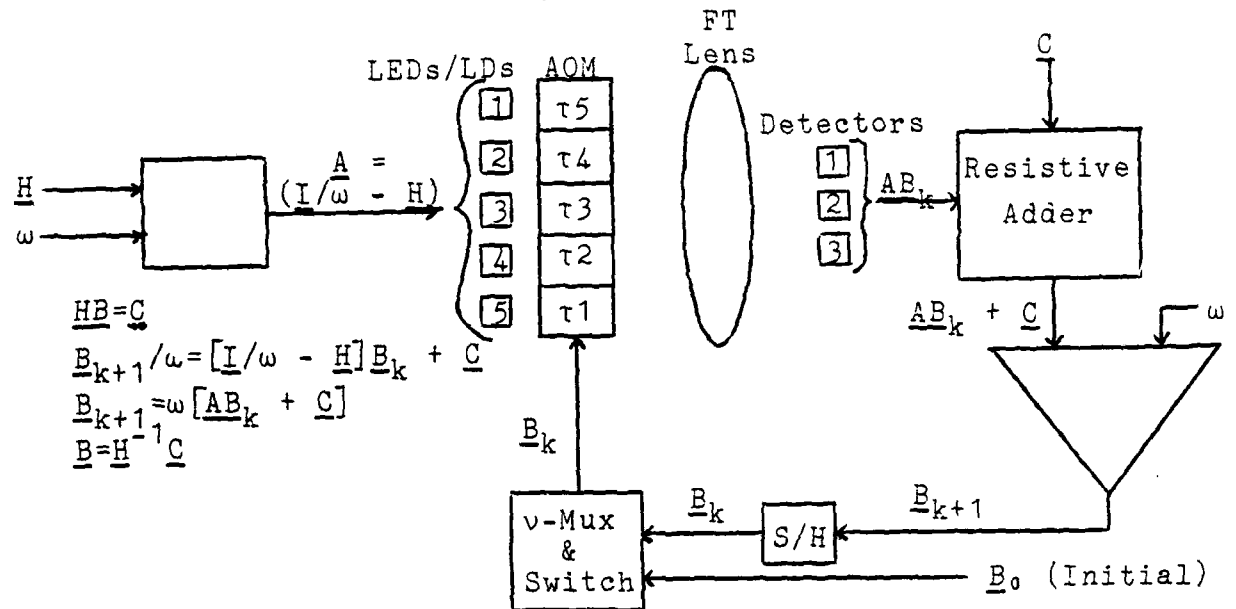
Note: Drawing Not to Scale

FT
Lens

LEDs/LDs AOM

Detectors

$\underline{H} \rightarrow$
$\omega \rightarrow$
$\dfrac{A}{(I/\omega - H)} = \rightarrow$

AOM: τ5, τ4, τ3, τ2, τ1
LEDs/LDs: 1, 2, 3, 4, 5

Detectors: 1, 2, 3 $\xrightarrow{AB_k}$

$C \downarrow$

Resistive Adder

$\underline{AB}_k + \underline{C} \downarrow$ $\qquad \omega \downarrow$

$\underline{HB} = \underline{C}$

$\underline{B}_{k+1}/\omega = [\underline{I}/\omega - \underline{H}]\underline{B}_k + \underline{C}$

$\underline{B}_{k+1} = \omega[\underline{AB}_k + \underline{C}]$

$\underline{B} = \underline{H}^{-1}\underline{C}$

$\underline{B}_k$

ν-Mux & Switch $\xleftarrow{\underline{B}_k}$ S/H $\xleftarrow{\underline{B}_{k+1}}$

$\underline{B}_0$ (Initial)

Figure 35 – General OKF Architecture (Matrix Inversion Case Detailed)

Table V – Time History for Matrix Inversion

T1	T2	T3	T4	T5	T6	T7	T8	Parameter	Comments
b_{11}	b_{21}	b_{31}	b'_{11}	b'_{21}	b'_{31}	b''_{11}	b''_{21}	$+1$	
b_{12}	b_{22}	b_{32}	b'_{12}	b'_{22}	b'_{32}	b''_{12}	b''_{22}	0	T4 on from dets
b_{13}	b_{23}	b_{33}	b'_{13}	b'_{23}	b'_{33}	b''_{13}	b''_{23}	-1	
–	–	–	–	a_{31}	–	–	a_{31}	1	
–	–	–	a_{21}	a_{32}	–	a_{21}	a_{32}	2	
–	–	a_{11}	a_{22}	a_{33}	a_{11}	a_{22}	a_{33}	3	LED/LD Inputs
–	–	a_{12}	a_{23}	–	a_{12}	a_{23}	–	4	
–	–	a_{13}	–	–	a_{13}	–	–	5	
–	–	d_{11}	d_{21}	d_{31}	d'_{11}	d'_{21}	d'_{31}	1	Detector Outputs
–	–	d_{12}	d_{22}	d_{32}	d'_{12}	d'_{22}	d'_{32}	2	$\underline{D} = \underline{AB}$
–	–	d_{13}	d_{23}	d_{33}	d'_{13}	d'_{23}	d'_{33}	3	$\underline{D'} = \underline{AB'}$
–	–	c_{11}	c_{21}	c_{31}	c_{11}	c_{21}	c_{31}	1	Matrix $\underline{C}$
–	–	c_{12}	c_{22}	c_{32}	c_{12}	c_{22}	c_{32}	2	Inputs to
–	–	c_{13}	c_{23}	c_{33}	c_{13}	c_{23}	c_{33}	3	the Adder
–	–	b'_{11}	b'_{21}	b'_{31}	b''_{11}	b''_{21}	b''_{31}	1	$\underline{B'} = \underline{B}_{k+1}$ and
–	–	b'_{12}	b'_{22}	b'_{32}	b''_{12}	b''_{22}	b''_{32}	2	$\underline{B'^T} = \underline{B}_{k+2}$ Inputs
–	–	b'_{13}	b'_{23}	b'_{33}	b''_{13}	b''_{23}	b''_{33}	3	to the S/H
–	–	–	b'_{11}	b'_{21}	b'_{31}	b''_{11}	b''_{21}	1	Freq-Muxed
–	–	–	b'_{12}	b'_{22}	b'_{32}	b''_{12}	b''_{22}	2	Inputs ≡ AOM
–	–	–	b'_{13}	b'_{23}	b'_{33}	b''_{13}	b''_{23}	3	Inputs from T4 on

92

defined (2) to produce a usable inversion product (where the two iteration values are equivalent within the processor accuracy) after only (4N-1) cell operations. This specification thus completes the time history definitions for all of the required Kalman filter operations.

It is evident that the general architecture illustrated in Figure 35 can also accomplish all the linear algebra required for Kalman filter operations. It has thus been chosen as the basic architecture for processing the filter algorithms identified in Chapter IV. However, prior to individual component selection and identification, the method by which the processor handles bipolar-valued data requires discussion. This requirement arises from the inability to detect the potential fields due to light. Since only power (or power per unit area) can be detected in the optical domain, there is thus no capability to represent negative numbers directly without a bipolar algorithm.

Since the overriding concerns in any bipolar-valued data handling algorithm are the pipelining of data and operations and the system throughput rate, utilization of a feedback loop requiring extensive A/D and D/A conversions must be avoided if at all possible. The simplest method of accomplishing this algorithm within the constraint thus becomes performing the necessary matrix algebra in the analog system to sufficient accuracy as the rest of the processor.

Consider first the multiplication of two bipolar scalars a and b. Allowing each scalar to be represented in bipolar form using a^+, a^-, b^+, and b^- notations, a positive scalar is expressed using the $^+$ notation whereas a negative scalar is denoted by the $^-$ notation. This form thus permits a representation of both positive and negative scalars which is always positive by defining the unused half of the bipolar representation to be zero. This yields the required bipolar multiplication

$$ab = (a^+ - a^-)(b^+ - b^-) = (a^+ b^+ + a^- b^-) - (a^- b^+ + a^+ b^-) \quad (5\text{-}13)$$

93

where the positive and negative parts of the product ab are

$$(ab)^+ = (a^+b^+ + a^-b^-) \qquad (5\text{-}14a)$$

$$(ab)^- = (a^-b^+ + a^+b^-) \qquad (5\text{-}14b)$$

and the bipolar output product is

$$ab = (ab)^+ - (ab)^- \qquad (5\text{-}15)$$

It is evident that one of the two terms of Equation (5-15) will always be zero. Extending this technique to the case of matrix-matrix multiplication (here, $\underline{A}\,\underline{B} = \underline{C}$) where the matrix elements are bipolar valued, each element a_{mn} of the $\underline{A}$ matrix is arranged as a (2x2) submatrix and each element of $\underline{B}$ is arranged as a two-element column vector. For example, in the case of N=M=2,

$$
\begin{bmatrix}
a_{11}^+ & a_{11}^- & a_{12}^+ & a_{12}^- \\
a_{11}^- & a_{11}^+ & a_{12}^- & a_{12}^+ \\
a_{21}^+ & a_{21}^- & a_{22}^+ & a_{22}^- \\
a_{21}^- & a_{21}^+ & a_{22}^- & a_{22}^+
\end{bmatrix}
\begin{bmatrix}
b_{11}^+ & b_{12}^+ \\
b_{11}^- & b_{12}^- \\
b_{21}^+ & b_{22}^+ \\
b_{21}^- & b_{22}^-
\end{bmatrix}
=
\begin{bmatrix}
c_{11}^+ & c_{12}^+ \\
c_{11}^- & c_{12}^- \\
c_{21}^+ & c_{22}^+ \\
c_{21}^- & c_{22}^-
\end{bmatrix}
\qquad (5\text{-}16)
$$

where each element c_{mn} of the output matrix is likewise represented as a two-element column vector as shown. As before, one of the two elements of each column vector of $\underline{C}$ will always be zero and all input and output elements will always be positive or zero.

This algorithm lends itself to direct pipelining and incorporation into all the linear algebra processing algorithms since the matrix output $\underline{C}$ is in the required form of $\underline{B}$ and can thus be fed back to the processor. The algorithm execution sequence is altered as illustrated in Table VI, resulting in an additional N operations of both processing and dead or delay time over each non-bipolar-valued case. The net effect of this algorithm on the architecture is thus merely an increase in the processor size: (3N-1) LEDs/LDs, 2M frequencies, and 2M detectors are now required. However, its direct integration into the flow and pipelining of data and operations yields significant increases in the potential sytem throughput rate.

94

Table VI. Bipolar-Valued Matrix-Matrix Sequence

Time	Actions	Outputs
T1	a_{11}^+ @ +1.5, $\bar{a}_{11}$ @ +.5, a_{21}^+ @ -.5, and $\bar{a}_{21}$ @ -1.5 input to AOM at τ1	
T2	1<u>st</u> column of $\underline{A}$ propagates to τ2 2<u>nd</u> column of $\underline{A}$ input to AOM at τ1 using same superposition frequencies	
T3	1<u>st</u> column of $\underline{A}$ propagates to τ3 2<u>nd</u> column of $\underline{A}$ propagates to τ2 3<u>rd</u> column of $\underline{A}$ input to AOM at τ1 using same superposition frequencies	
T4	1<u>st</u> column of $\underline{A}$ propagates to τ4 2<u>nd</u> column of $\underline{A}$ propagates to τ3 3<u>rd</u> column of $\underline{A}$ propagates to τ2 4<u>th</u> column of $\underline{A}$ input to AOM at τ1 using same superposition frequencies b_{11}^+ input to LED/LD 2 $\bar{b}_{11}$ input to LED/LD 3 b_{21}^+ input to LED/LD 4 $\bar{b}_{21}$ input to LED/LD 5	c_{11}^+ $\bar{c}_{11}$ c_{21}^+ $\bar{c}_{21}$
T5	1<u>st</u> column of $\underline{A}$ propagates to τ5 2<u>nd</u> column of $\underline{A}$ propagates to τ4 3<u>rd</u> column of $\underline{A}$ propagates to τ3 4<u>th</u> column of $\underline{A}$ propagates to τ2 b_{12}^+ input to LED/LD 1 $\bar{b}_{12}$ input to LED/LD 2 b_{22}^+ input to LED/LD 3 $\bar{b}_{22}$ input to LED/LD 4	c_{12}^+ $\bar{c}_{12}$ c_{22}^+ $\bar{c}_{22}$

The arrangement in Equation (5-16) can also be used to perform a true matrix subtraction without the need to handle negative numbers. For example, for

$$\underline{A} - \underline{B}\,\underline{C} = \underline{D} \qquad (5\text{-}17)$$

the equation is rewritten using the earlier $()^+$ and $()^-$ notation as

$$\underline{D} = \underline{D}^+ - \underline{D}^- = (\underline{A}^+ - \underline{A}^-) - |(\underline{BC})^+ - (\underline{BC})^-|$$
$$= |\underline{A}^+ + (\underline{BC})^-| - |\underline{A}^- + (\underline{BC})^+| \qquad (5\text{-}18)$$

Realization of Equation (5-17) in the form of Equation (5-18) follows directly from the matrix partitioning used in Equation (5-16). The bipolar and matrix subtraction algorithm now completes the list of required operations for Kalman filtering. It is left to the final section of this chapter to specify the performance of this processor completely as well as to compare its performance to a software implementation. Until these steps are accomplished, the worth of the processor cannot be adequately judged.

5.3   Design and Analysis of the Optical Kalman Filter

It is in this section that the actual processor design and development subject to all the previously outlined constraints is reported. Analysis of the final design is accomplished with particular emphasis on satisfaction of the overall problem specifications. The analysis also includes a comparison of the projected optical solution to one which has been formulated in software. It is on the basis of these analyses that the optical architecture developed in Section 5.2 is proposed as a viable, and perhaps preferable, alternative to other previously developed solutions.

Prior to system design, an analysis of the overall algorithm is required to generate a minimum system processing rate for the OKF. Figure 36 illustrates the master flow diagram of the tracker. For the purposes of these analyses, each cycle of the tracker is defined to start at the time of $\underline{R}(\alpha,\beta)$ availability from the enhanced optical correlator (EOC)
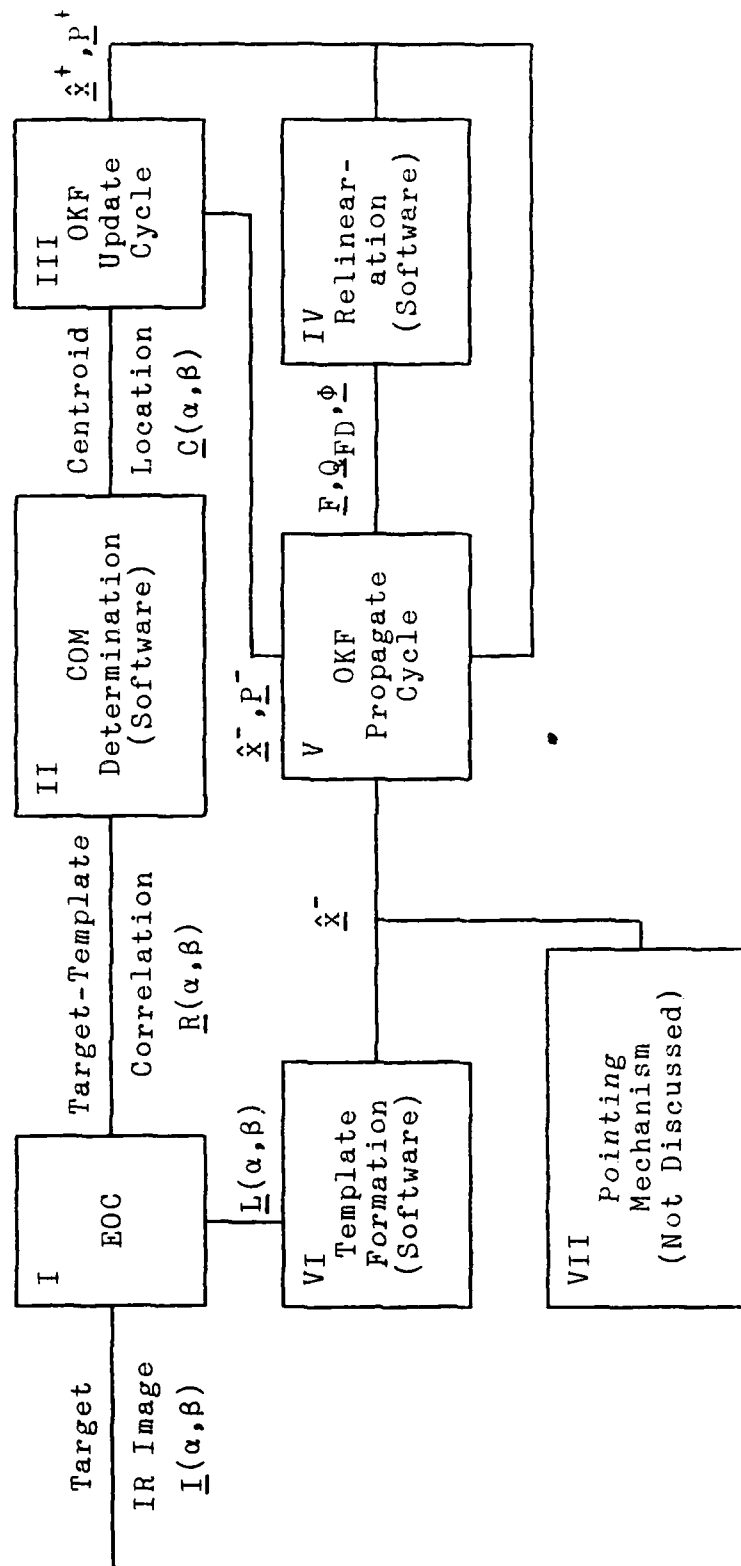
96

Figure 36 - Master Tracker Flow Diagram

shown as Block I in Figure 36. Noting that the pointing system response must occur prior to the next sampling time, some assumption must be made as to the amount of time this block will require. For the purposes of this research, the time required to generate and implement the pointing system commands is assumed to be 15 milliseconds. This assumption is based on two factors: (1) it is anticipated that implementation of the tracking algorithm developed in Chapters III and IV will require only small excursions (in terms of microradians) after each propagation cycle for correction of the previously applied control inputs; and (2), since the template for the EOC is generated in parallel with the pointing commands, the template is easily generated within this time frame. With these developments, the remaining software processing time must be specified to generate the minimum throughput rate of the OKF.

The following computation times (11) were thus used in the analysis.

Memory Storage or Retrieval	1 μsec
Addition or Subtraction	2.7 μsec
Multiplication	4.1 μsec
Division	6.6 μsec
A/D or D/A Conversion	50 μsec

The computational and memory manipulation times specified are representative of single precision processing times typical of the IBM 360 series and some smaller state-of-the-art computers.

The format $C(\alpha, \beta)$ in Block II, under these definitions, requires μsec. This figure was obtained by 64 iterations of the utine and one iteration of the T2 routine defined in Table VII. For operations in parallel, the determining time factor is specified as the largest processing time applicable. For example, since the correlation A/D conversion occurs in parallel with the rest of the processing steps of T1, this subblock requires one iteration of 79.7 μsec

and 63 iterations of 50 µsec. The other processing blocks were analyzed in a similar manner. Thus, the OKF measurement update cycle (Block III in Figure 36) requires 422 µsec of software processing time as indicated by the routine outlined in Table VIII (where N is specified in Chapter IV). Table IX develops the processing time required both on an initial basis (formation of all values) and thereafter (formation of only non-constant values) for the relinearization process (Block IV). These processing times are 613.9 µsec and 298.9 µsec, respectively. Finally, Table X lists the task breakdown of the OKF propagation cycle (Block V) which specifies the 486.4 µsec software processing time. Combining these requirements with the 15 msec pointing system/template formation (Blocks VI and VII) time assumed earlier, the total amount of non-OKF processing time is 19.7682 msec for the initial iteration and 19.4532 msec thereafter.

These tables also specify the number of optical processing operations required for the formation of $\underline{x}^+$, $\underline{P}^+$, and $\underline{P}^-$ in the OKF. Adding these requirements from both filter cycles, a total number of 194 optical processing operations will completely perform the required linear algebra. By subtracting the non-OKF processing time from the time per FLIR frame (33.3333 msec), the optical operations must be accomplished within 13.5651 msec on the initial cycle and 13.8801 msec on subsequent cycles. Thus, the minimum OKF processing rate is approximately 14.3 kHz.

With this number in hand, the component choice for the optimum (in terms of both component integration and uniform output across the entire parallel signal representation) OKF can now be specified. Since all of the operations in the OKF update cycle are bipolar, the optical processor must have (as outlined in Section 5.2) 23 LEDs/LDs and 16 detectors for $N=M=8$. This immediately presents a tradeoff between the LED/LD power with its resulting spatial requirement and the amount of acoustic attenuation over the resulting required (by the LED/LD array) AOM aperture. This in itself is the major design constraint.

99

Table VII. COM Determination Processing Requirements

Time	Operation	Duration (μsec)
T1	1-In parallel, get vertical pixel number, get horizontal pixel number, and A/D convert one of 64 pixels	50
	2-Threshold pixel intensity	2.7
	3-Tempstore pixel intensity	1
	4-Add value to vertical sum	2.7
	5-Store vertical sum	1
	6-Retrieve value from tempstore	1
	7-Multiply by vertical pixel number	4.1
	8-Add to weighted vertical sum	2.7
	9-Store in weighted vertical sum	1
	10-Retrieve value from tempstore	1
	11-Repeat 4 and 5 for horizontal sum	3.7
	12-Repeat 6 through 9 for weighted horizontal sum	8.8
		Total 79.7
T2	1-Divide weighted horizontal sum by horizontal sum	6.6
	2-Store in memory	1
	3-Get weighted vertical sum	1
	4-Repeat 1 and 2 for vertical case	7.6
		Total 16.2

Table VIII. OKF Update Cycle Processing Requirements

Time	Operation	Software Duration	Optical Operations
T1	D/A convert $\underline{H}$, $\underline{P}^-$, $\underline{H}^T$, $\underline{R}$, $\underline{x}^-$, and $\underline{z}$ as per pipeline (one iteration of 22 memory retrievals plus D/A conversion and seven iterations of D/A conversion/memory retrieval in parallel)	422 µsec	
T2	Form $\underline{H}\,\underline{P}^-\underline{H}^T + \underline{R}$ (Bipolar 3-matrix multiply with real-time resistive add, N=8)		31 (4N-1)
T3	Form $\underline{H}\,\underline{P}^-$ (Bipolar 2-matrix multiply, N=8)		23 (3N-1)
T4	Form $\underline{z} - \underline{H}\,\hat{\underline{x}}^-$ using Eqn. (5-18) (Bipolar 2-matrix multiply with real-time resistive add, N=8		23 (3N-1)
T5	Invert $\underline{H}\,\underline{P}^-\underline{H}^T + \underline{R}$ (Bipolar inversion, N=2)		9 (5N-1)
T6	Form $\underline{K}$ (Bipolar 3-matrix multiply, N=8)		31 (4N-1)
T7	Form $\underline{P}^+$ using Eqn. (5-18) (Bipolar 3-matrix multiply with real-time resistive add, N=8)		31 (4N-1)
T8	Form $\hat{\underline{x}}^+$ (Bipolar 2-matrix multiply with real time resistive add, N=8)		23 (3N-1)

Table IX.   Relinearization Processing Requirements

Time	Operation	Initial	Thereafter
T1	Zero $\underline{\Phi}_F$, $\underline{Q}_{FD}$ matrices (64 elements each)	128 μsec	
T2	Produce $\underline{\Phi}_F$, $\underline{Q}_{FD}$ matrices (Initial cycle-60 multiplies, 11 additions, 77 memory manipulations, 2 divisions, and 2 exponentials @ 50 sec per exponential; thereafter 47 multiplies, 10 additions, 66 memory manipulations, and 2 divisions)	485.9 μsec	298.9 μsec
	Totals	613.9 μsec	298.9 μsec

Table X.   OKF·Propagation Cycle Processing Requirements

Time	Operation	Software Duration	Optical Operations
T1	Form $\hat{\underline{x}}^-$ using Eqn. (4-15) (8 multiplies & 8 additions)	54.4 μsec	
T2	D/A Convert $\underline{\Phi}_F$, $\underline{P}^+$, and $\underline{\Phi}_F^T$ as per pipeline (one iteration of 32 memory retrievals plus D/A conversion and seven iterations of memory retrieval/conversion in parallel)	432 μsec	
T3	Form $\underline{P}^-$ (3-matrix multiply with real time resistive add, N=8)		23 (3N-1)

This major design constraint defines the approach to the component selection stage of the design process. Recalling that the modulator is the key component of the architecture, it must be specified first and the other components (since there is a greater range of product availability for each type) fitted to the modulator. However, in order to specify the modulator, some assumptions must be made about the power range (in terms of peak power) required of the source array. This will allow an initial design which can be modified (if required) to correspond to actual component selection.

From industrial data, the appropriate parameters of interest for various AOM materials are listed in Table XI.

Table XI. AOM Parameters of Interest

Material/ Mode	Acoustic Velocity v_s (mm/μsec)	Acoustic Attenuation α_0 (dB/μs-GHz^2)	Fig. of Merit M_ω
PbMO$_4$/ L(001)	3.63	5.5	0.22
TeO$_2$/ L(001)	4.2	6.3	0.23
GaP/ L(110)	6.32	3.8	0.8473

Assuming for the moment that each laser diode (due to the power versus size relationship and output power required) must be spaced 1.5mm center-to-center, the resulting working aperture of 34.5mm when combined with the AOM acoustic velocities yields the following data rates into the cell (acoustic velocity divided by the laser diode spacing) and time apertures (working aperture divided by acoustic velocity).

Material	Data Rate Into Cell	Time Aperture
PbMO$_4$	2.42 MHz	9.5 usec
TeO$_2$	2.8 MHz	8.21 usec
GaP	4.213 MHz	5.46 usec

103

As none of these required data rates are unreasonable for the associated electronics, further investigation is warranted. Since AOMs are specified at 3dB frequency response bandwidths (for the acoustic frequencies), the requirement that only the flat (i.e., uniform) part of the response curve for a given frequency range specifies that the device response bandwidth be larger than required just by the necessity of producing 16 products (from 2M detectors, M=8) spaced at some constant distance. As this (as well as diffraction efficiency) is a function of transducer impedance matching (higher frequencies require smaller area transducers), the additional desire is that the center frequency be kept as low as possible. These factors merge into specifications of 10 MHz frequency separation per row product (150 MHz total bandwidth for 16 products), a 250 MHz AOM acoustic bandwidth, and an AOM center frequency of 380 MHz to preclude second harmonic effects within the range of cell frequencies.

With these criteria defined, the total cell attenuation across the AOM working aperture becomes

Material	α
$PbMO_4$	7.55 dB
TeO_2	7.47 dB
GaP	3.00 dB

where the total cell attenuation is the acoustic attenuation identified in Table XI multiplied by the AOM's time aperture and acoustic center frequency. Combining this data with the superior thermal conductivity of GaP (37 times that of TeO_2), the choice of material is obvious. Thus, a GaP AOM with a center frequency of 380 MHz, a device acoustic bandwidth of 250 MHz (380 MHz ± 125 MHz), and a transducer with appropriate shape to produce the collimated acoustic beam illustrated in Figure 37 is selected.
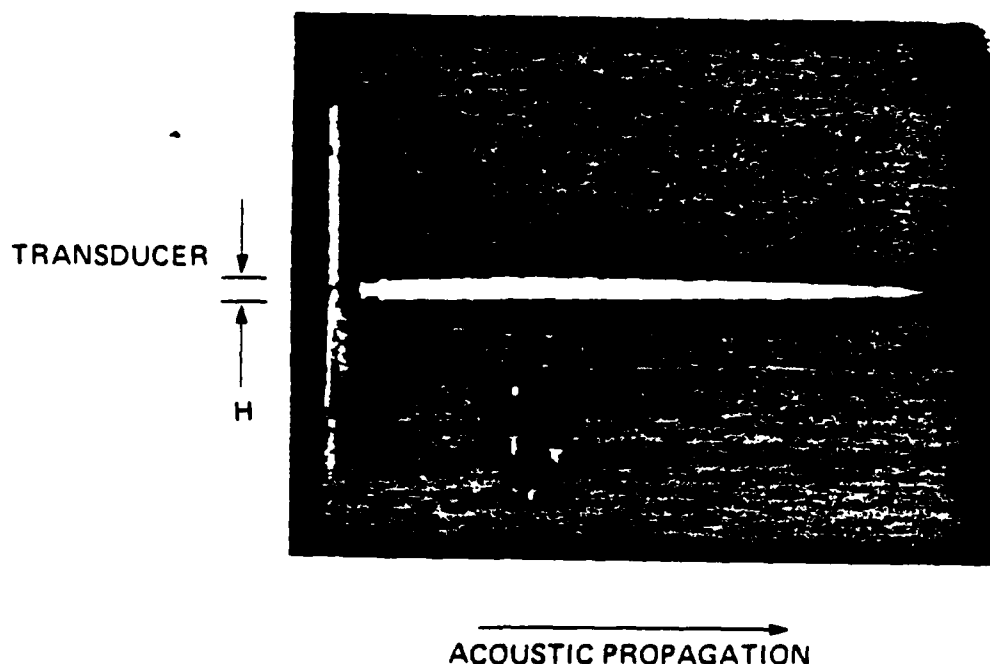
104

TRANSDUCER

H

ACOUSTIC PROPAGATION

Figure 37 - Acoustic Beam Propagation in GaP

The entire OKF can now be specified. For ease of imple-
mentation, the input data rate is chosen to be 4 MHz so that
custom clocks do not need to be incorporated into the archi-
tecture. This produces the specifications (based on $\lambda=0.85\mu m$
so as to provide the greatest possible range of laser diode
product selection) summarized in Table XII, where all values
are as defined in this chapter. These specifications thus

Table XII. AOM Specifications

Parameter	Value
Working Aperture	36.34mm
LD Center-to-Center Spacing	1.58mm
Attenuation over working aperture	3.16 dB
Bragg Angle	0.442^0
Angular Separation Between Products ($\Delta\theta$)	0.023^0
Undiffracted-Diffracted Angular Separation	0.712^0
Diffraction Efficiency (1 Watt Drive)	50%

require: (1) the detector selected must have a minimum dyna-
mic range of 30 dB (from the original problem specification)
at the wavelength of interest; (2) the laser diode chosen
must have a minimum dynamic range of 33.16 dB; and (3), the
lens system used must have an effective focal length of 5m
[from Equation (5-7)] to produce a center-to-center spacing
of 2mm (due to the minimal 30 dB dynamic range requirement
plus an allowance for greater dynamic range) and a focussed
spot of 145 μm at the output plane.

Taking these criteria one at a time, the detector cho-
sen has the following specifications (1983 Laser Focus
Buyer's Guide, page 52):

Minimum Detectable Power	500 pW
Saturation Power	1 mW
Rise Time	50 nsec
Diameter	1.85 mm

Although these detectors must be housed in a custom-built
array, their compact size allows ready implementation in
this manner.

Similarly, the same source (page 184) defines the fol-
lowing specifications for the laser diode selected:

Peak Power	20 mW
Dynamic Range	54 dB
Repetition Rate (Maximum)	5 MHz
Pulse Length	60 nsec
Beam Divergence	Collimated
Wavelength	0.85 μm
Diameter	1.35 mm

Again, the geometry is such that a custom array is easily
formed.

This leaves only the lens system to be specified.
Obviously, a five-meter focal length lens resulting in a
10-meter separation between the AOM and the detection plane

would make the system unwieldy in a physical sense. Thus, the sole method of accomplishing the required focal length within physical realizable limits necessitates combining a negative lens in tandem with a positive lens. This process increases the angular divergence of the products in a linear manner, and is most easily calculated in diopters. From the 1983 Melles Griot Optics Guide, a diopter is defined as 1000 divided by the lens focal length in mm. Since a five-meter focal length is desired, the number of diopters required is 0.2. To keep the focal lengths of both lenses at a reasonable limit, an arbitrary boundary of 5 mm is selected. For a negative lens with a focal length of -400mm, the diopter conversion works out to be -2.5. This then requires a 2.7 diopter positive lens, which works out to a 370mm focal length lens by the formula given above. Thus, all specifications are satisfied for the lens system, and this completes the specification of OKF componenets.

To analyze the OKF completely, since it is obvious from the dynamic range of the laser diode that a uniform response is achievable (across the output parallel representation) by introducing additional gain where required at the input (Section 5.2), it is only necessary to calculate the minimum and maximum signals through the system and compute their resultant dynamic range. Thus, for minimum power, the calculation is (using the minimum value for each data point)

(80nW input)(.01 diffraction efficiency)(.95 lens trans)=760 pW

which is above the defined threshold of the detector. The maximum power level through the system is

(20 mW input)(.5 diffraction efficiency)(.95 lens trans)=9.5 mW

Since this value is above the detector's saturation level, the system is specified to operate at a maximum power level of 1 mW throughput. This yields an effective dynamic range of 61.2 dB (equivalent to 20-bit digital accuracy).

With the entire OKF designed and analyzed, the operation of the tracking algorithm warrants reinvestigation. Since 194 optical operations are required for the filter linear algebra, the OKF accomplishes all its processing in 48.5 µsec at the 4 MHz data rate. This can be contrasted with a software computation time requirement of 435.2 usec merely to multiply a square matrix of dimension eight by a vector of appropriate length. This decrease in computation time results in the overall computation time of the tracker being capable of supporting much higher bandwidth operations.

For example, a 100 Hz system bandwidth could be supported as follows. Given the fact that the dynamics model used is based on a constant turn-rate, it can be postulated that for a sample period less than one-third the earlier definition, the resultant filter errors will be reduced by about the ratio since $\underline{Q}_{FD}$ is directly proportional to Δt. Thus, by merely maintaining the pointing system response rate, the pointing system response time can be cut to 5 msec from the earlier assumption of 15 msec. Template formation can also be accomplished within this time frame. By redefining the pointing system response time in this manner, the system processing requirements (optical and software) now become 9.8167 msec for the first iteration and 9.5017 msec thereafter.

This, however, would require that the FLIR sensor be discarded in favor of a custom array of real time sensors, which would be sampled every 10 msec. This proposal may produce some very useful advantages. Since the sensors are real-time, smearing of the image (and thus introducing noise into the transform) due to relative motion between the target and tracking window trajectories would cease to exist. Additionally, since the noise mechanisms of the detector types are different, the individual pixel noise term (heretofor neglected due to predominance of spatially correlated noise) can be substantially reduced by careful detector choice. As an array of truly independent detectors, moreover, the

108

inevitable crosstalk between pixels is entirely negated. Finally, due to the substantially higher sampling rate, filter transient response times should decrease dramatically.

With the entire tracker now completely specified, conclusions and recommendations can be drawn about its worth. Thus, the next chapter relates the thesis research to the original goals expressed in Chapter I and projects these relationships forward to their next logical step.

VI. Conclusions and Recommendations

6.1 Overview

As the major goal of this research is to demonstrate that the use of optics and optical processing can produce substantial system enhancement at the current state of optical development, this theme is central to all conclusions drawn. Coupled to this theme is the necessity of identifying a satisfactory stochastic algorithm that will be fully capable of providing the level of performance required of a high energy laser pointing system. These two factors thus constitute the major bases for this study.

All conclusions and recommendations developed within this chapter are therefore related to these bases. Although the chapter is not strictly separated into stochastic and optical sections, care is taken to identify each conclusion and recommendation made with respect to its relationship to both the stochastic and optical bases. By examining all factors in this light, all research reported in this thesis is tied together to produce an end product which is usable in either its current form or easily modified to reflect alternate performance criteria.

Section 6.2 thus identifies all appropriate conclusions which can be drawn from the research performed. Recommendations developed from these conclusions are then listed in the final section of this chapter. In this manner, the thesis is concluded.

6.2 Conclusions

Since two trackers using the same stochastic algorithm have been proposed in this thesis, both the FLIR-constrained and unconstrained trackers must be examined in turn. In this manner, any differences in conclusions can be brought to light, and will allow recommendations to be developed based on these differences.

Initially examining the FLIR-constrained tracker, it is important to note that the use of optical processing in this tracker produces no substantial performance enhancement. This is chiefly due to the fact that the optical Kalman filter and enhanced optical correlator have system processing bandwidths far in excess of that provided by the use of the FLIR array sensor. This limitation thus results in the tracking system being required to idle a minimum of 40% between measurements and represents a substantial waste of the capability of the tracker's individual components. On a stochastic basis, given the previous research (8,21,23), the developed algorithm can be reasonable anticipated to yield acceptable performance against the postulated targets of interest. Therefore, should the FLIR-constrained tracker be the solution of choice, it must be concluded that a software implementation of the developed stochastic algorithm is more than adequate and indeed preferable to process the data.

However, if the unconstrained tracker is used to develop an alternative solution, the use of the optical processing techniques described within this thesis become mandatory to provide the necessary system bandwidths to support the overall tracker throughput rate. Additionally, use of the same stochastic algorithm at the higher measurement rate can reasonably be expected to produce enhanced performance in the critical areas of transient response times and error statistics, as outlined in Chapter V. Given the statistics developed in the earlier research (8,21,23), it is indeed possible that the unconstrained tracker can produce a pointer-constrained system due to its higher processing bandwidth against most targets of interest. Thus, it must be concluded that the unconstrained tracker developed within this thesis is indeed the preferable solution.

Finally, some conclusions which are common to both of the trackers proposed in this thesis must be identified. Given the state-of-the-art of integrated optics (27), either tracker's optical Kalman filter could be implemented in this form. This

could produce major savings in size, weight, and power consumption requirements for the system. Additionally, the use of optics in either case does permit the use of more sophisticated stochastic algorithms, particularly if a multiple-model adaptive filter is to be used. While these conclusions do not seem to be critical for the case of a ground-based laser weapon, translation of the laser system to either an airborne or space environment may very well require a combination of these benefits, chiefly provided by the use of optical processing techniques.

In sum, it is the conclusion of this thesis that the unconstrained tracker developed within this thesis is the solution of choice for a ground-based laser weapons system. Since any successful implementation of this tracker requires the use of the optical processing techniques developed and analyzed within this thesis within the constraint of using currently available optical components, the major basis of the thesis has been satisfied. Lastly, given the other conclusions developed within this section, the use of the identified optical processing techniques will provide substantially more flexibility in the choice of stochastic algorithms to match the scenario of application. As the use of stochastic algorithms is indicated due to their enhanced performance over correlation algorithms, the processing bed developed is applicable to the widest range of problem scenarios.

6.3 Recommendations

The conclusions developed in Section 6.2 yield three recommendations for future research efforts. These recommendations are based not only on the conclusions but also on the premise that the maximum benefit be derived from the work performed within this thesis.

The first recommendation is that a complete Monte Carlo performance analysis be performed for both trackers proposed. This performance analysis should be conducted in two phases.

First, both trackers should be evaluated against the trajec-
tories outlined in the truth model presented in Chapter II.
After careful evaluation of the tuning parameters involved,
both trackers should then be analyzed using the same techniques
against trajectory tapes of actual aircraft and missile per-
formance. In this manner, realistic statistics can be genera-
ted while gaining tuning experience with the filter.

Secondly, a test bed optical Kalman filter should be
developed and used to generate a true modulation transfer
function after all optical components have been optimized as
identified in Chapter V. This test bed can then be used
to evaluate the system throughput rate of any stochastic
algorithm. Upon combining the results of this recommendation
with those of recommendation one, a reasonable projection of
filter performance versus sampling rate variations can be
developed for a variety of different algorithms.

Lastly, it is strongly recommended that a serious inves-
tigation into alternatives to the FLIR array sensor be initiated.
As the major system limitation, the FLIR array sensor is the
major stumbling block to enhanced performance. Development
of a reasonable alternative to the FLIR sensor, particularly
in time response characteristics, will then enable the develop-
ment of a final optimal package.

It is believed that the results of these recommendations
will enable the final specification of a pointing and tracking
system which will yield enough performance benefit to warrant
implementation. It is also postulated that the experience
gained from both this thesis and implementation of its recom-
mendations will allow a much easier translation of the final
result from a ground-based version to other scenarios. In
sum, the optimization of the final product is the end goal of
this thesis, its conclusions, and its recommendations.

Bibliography

1. Casasent, D. P., and G. Silbershatz. "Product Code Processing on a Triple Product Processor," _Applied Optics_, 21: 2076-2084 (1 June 1982).

2. Casasent, D. P., J. Jackson, and C. Neuman. "Frequency-Multiplexed and Pipelined Iterative Optical Systolic Array Processors," _Applied Optics_, 22: 115-124 (1 January 1983).

3. Casasent, D. P., and A. Ghosh. "Optical Linear Algebra," _SPIE Proceedings_, 388: 388-24 (January 1983).

4. Caufield, H. J., W. K. Cheng, and J. H. Gruninger. "Using Optical Processors for Linear Algebra," _SPIE Proceedings_, 388: 388-25 (January 1983).

5. Flynn, P. M. _Alternative Dynamics Models and Multiple Model Filtering for a Short Range Tracker_. MS Thesis. Wright-Patterson AFB, Ohio: School of Engineering, Air Force Institute of Technology, December 1981.

6. Goodman, J. W. _Introduction to Fourier Optics_. San Francisco, McGraw-Hill, 1968.

7. Jensen, R. L., and D. A. Harnley. _An Adaptive Distributed-Measurement Extended Kalman Filter for a Short Range Tracker_. MS Thesis. Wright-Patterson AFB, Ohio: School of Engineering, Air Force Institute of Technology, December 1979.

8. Kozemchak, M. R. _Enhanced Image Tracking: Analysis of Two Acceleration Models in Tracking Multiple Hot-Spot Images_. MS Thesis. Wright-Patterson AFB, Ohio: School of Engineering, Air Force Institute of Technology, December 1982.

9. Lee, S. H. "New Optical Transforms for Statistical Image Recognition," _SPIE Proceedings_, 388: 388-22 (January 1983).

10. Lewak, G., S. H. Lee, and W. T. Cathey. "Solution of Matrix and Integral Equations by Optical Methods," _SPIE Proceedings_, 388: 388-32 (January 1983).

11. Maybeck, P. S. _Stochastic Models, Estimation, and Control, Volume 1_. New York, Academic Press, 1979.

12. Maybeck, P. S., and D. E. Mercier. "A Target Tracker Using Spatially Distributed Infrared Measurements," _IEEE Transactions on Automatic Control_, AC-25: 222-225 (April 1980).

13. Maybeck, P. S., D. A. Harnley, and R. L. Jensen. "Robustnes of a New Infrared Target Tracker," _Proceedings of the IEEE National Aerospace and Electronics Conference_: 639-644 (May 1980).

14. Maybeck, P. S., R. L. Jensen, and D. A. Harnley. "An Adaptive Extended Kalman Filter for Target Image Tracking," _IEEE Transactions on Aerospace and Electronics Systems_, AES-17, No. 2: 173-180 (march 1981).

15. Maybeck, P. S. _Stochastic Models, Estimation, and Control, Volume 2_. New York, Academic Press, 1982.

16. Maybeck, P. S. "Advances in the Techniques and Technology of the Application of Nonlinear Filters and Kalman Filters," _AGARD-AG-256_: 10-1 - 10-15 (March 1982).

17. Maybeck, P. S. _Stochastic Models, Estimation, and Control, Volume 3_. New York, Academic Press, 1982.

18. Maybeck, P. S., W. H. Worsley, and P. M. Flynn. "Investigation of Constant Turn-Rate Dynamics Models in Filters for Airborne Vehicle Tracking," _Proceedings of the IEEE National Aerospace and Electronics Conference_: 896-903 (May 1982).

19. Maybeck, P. S., and S. K. Rogers. "Adaptive Tracking of Dynamic Multiple Hot-Spot Target IR Images," _Proceedings of the IEEE Conference on Control_: 111-118 (December 1982).

20. Mercier, D. E. _An Extended Kalman Filter for Use in a Shared Aperture Medium Range Tracker_. MS Thesis. Wright-Patterson AFB, Ohio: School of Engineering, Air Force Institute of Technology, December 1978.

21. Millner, P. P. _Enhanced Tracking of Airborne Targets Using a Correlator/Kalman Filter_. MS Thesis. Wright-Patterson AFB, Ohio: School of Engineering, Air Force Institute of Technology, December 1982.

22. Rhodes, W. T., A. Tarasevich, and N. Zepkin. "Complex Covariance Matrix Inversion with a Resonant Electro-Optic Processor," _SPIE Proceedings_, 388: 388-26 (January 1983).

23. Rogers, S. K. *Enhanced Tracking of Airborne Targets Using Forward Looking Infrared Measurements.* MS Thesis. Wright-Patterson AFB, Ohio: School of Engineering, Air Force Institute of Technology, December 1981.

24. Strang, G. *Linear Algebra and its Applications.* New York: Academic Press, 1980.

25. Sze, S. M. *Physics of Semiconductor Devices.* New York: Wiley, 1981.

26. Vander Lugt, A. "Adaptive Optical Processing Techniques," *SPIE Proceedings*, *388*: 388-17 (January 1983).

27. Verber, C., H. J. Caufield, J. E. Ludman, and P. D. Stilwell, Jr. "Suggested Optical Instrumentation of Pipelined Polynomial Processors," *SPIE Proceedings*, *388*: 388-30 (January 1983).

28. Verdeyen, J. T. *Laser Electronics.* Englewood Cliffs, NJ: Prentice-Hall, 1981.

29. Worsley, W. M. *Comparison of Three Extended Kalman Filters for Air-to-Air Tracking.* MS Thesis. Wright-Patterson AFB, Ohio: School of Engineering, Air Force Institute of Technology, December 1980.

30. Yariv, A. *Introduction to Optical Electronics.* New York: Holt, Rinehart and Winston, 1976.

116

Two-Dimensional Finite Discrete Fourier Transform
Interpretation and Test

Similar to the presentation of J. W. Goodman, Reference 6, the Rect function is defined to extract one period of the spatial intensity function as

$$\text{Rect}_N(x,y) = \begin{bmatrix} 1 & 0 \leq x \leq N-1, \ 0 \leq y \leq N-1 \\ 0 & \text{otherwise} \end{bmatrix} \quad (A-1)$$

Reproducing Equations (2-3) and (2-4) of Reference 23 and using the Rect function to define the area sequence $g(x,y)$ as being zero outside the interval $0 \leq x \leq N-1$

$$g(x,y) = g'(x,y) \ \text{Rect}_N(x,y) \quad (A-2)$$

$$G(f_x, f_y) = \left[\sum_{x=0}^{N-1} \sum_{y=0}^{N-1} g(x,y) \ e^{\frac{-j2\pi}{N}(f_x x + f_y y)} \right] \text{Rect}_N(f_x, f_y) \quad (A-3)$$

$$g(x,y) = \frac{1}{N^2} \left[\sum_{f_x=0}^{N-1} \sum_{f_y=0}^{N-1} G(f_x, f_y) \ e^{\frac{+j2\pi}{N}(f_x x + f_y y)} \right] \text{Rect}_N(f_x, f_y) \quad (A-4)$$

$G(f_x, f_y)$ is the Finite Discrete Fourier Transform of $g(x,y)$. The Rect function of Equation (a-1) is separable in the two independent variables:

$$\text{Rect}_N(f_x, f_y) = \text{Rect}_N(f_x) \ \text{Rect}_N(f_y) \quad (A-5)$$

Equation (A-3) can now be written as

$$G(f_x, f_y) = \left[\sum_{y=0}^{N-1} X(f_x, y) \ \exp^{\frac{-j2\pi}{N}(f_y y)} \right] \text{Rect}_N(f_y) \quad (A-6)$$

where

$$X(f_x, y) = \left[\sum_{x=0}^{N-1} g(x,y) \ \exp^{\frac{-j2\pi}{N}(f_x x)} \right] \text{Rect}_N(f_x) \quad (A-7)$$

Equation (A-7), $X(f_x, y)$ corresponds to an N-point one dimensional Discrete Fourier Transform for each value of the row index y. $X(f_x, y)$ is the result of N one dimensional

117

transforms, one for each row of $g(x,y)$. In figure A-1a, if y is held constant, say $y=2$, and a one-dimensional Fourier Transform is accomplished across that row, the variation in the image intensities from column to column would result in the zero frequency of that variation being located at $x'=1$ and $y'=2$ of Figure A-1b, while the coefficient associated with the fundamental, the first harmonic, in both directions would be found at $x'=2$ and $y'=2$ with its conjugate located at $x'=N$ and $y'=2$.
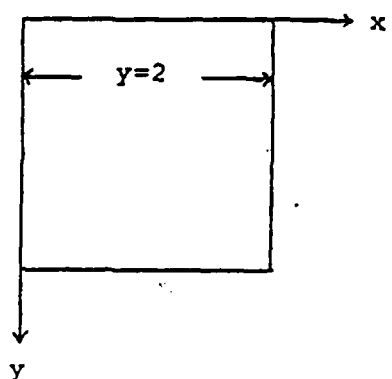
(a) Original Data Array
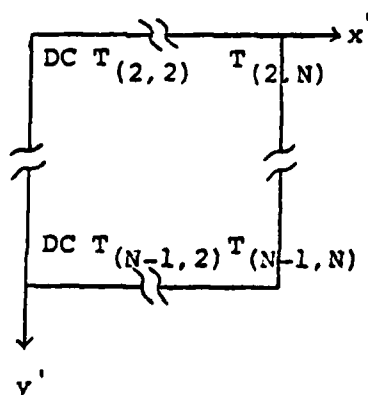
(b) Transformed Data

Figure A-1 - Row Transform Result of 2-D DFT

To complete the two-dimensional Discrete Fourier Transform, Equation (A-6) expresses how to implement the N one-dimensional transforms along each column. To summarize this general interpretation of the two-dimensional Discrete Fourier Transform, Equations (A-6) and (A-7) show how the two-dimensional transform is achieved by using a one-dimensional transform on the rows first and then on the columns, or vice versa.

For the case where the image intensity function is separable in the two independent variables x and y, for example $g(x,y)$ having the property that

$$g(x,y) = g_1(x) \; g_2(y) \qquad (A-8)$$

the two-dimensional Discrete Fourier Transform, $G(f_x, f_y)$, becomes the product of the one-dimensional independent transforms $G_1(f_x)$ and $G_2(f_y)$.

$$G(f_x, f_y) = G_1(f_x) \; G_2(f_y) \qquad (A-9)$$

A function of two independent variables is separable within a specific coordinate system if it can be written as a product of two functions of one independent variable each. The two-dimensional transform degenerates to holding the row index constant, for example, and running the one-dimensional transform across the columns, for any one of the N rows. Similarly the column index is held while the one-dimensional transform is accomplished across the rows, and this is done for any of the columns. The results of these two independent transforms are then multiplied together.

This leads to some interesting algebra which can be exploited to test the implementation of the two-dimensional Discrete Fourier Transform. In Figure A-1, $T_{(2,2)}$ will consist of the product of the two one-dimensional transform fundamental coefficients for that row or column. If x is the column coordinate and y is the row coordinate, then $T_{(y,x)}$ is defined as

$$T_{(2,2)} = \left[\left[\begin{array}{c} \text{1st harmonic in } y \\ \text{for column 2} \end{array} \right] \equiv y_{(1,2)} \right] \cdot \left[\left[\begin{array}{c} \text{1st harmonic in } x \\ \text{for row 2} \end{array} \right] \equiv x_{(1,2)} \right]$$

$$(A-10)$$

119

$$T_{(2,N)} = \left[\left[\begin{array}{c} \text{1st harmonic in } y \\ \text{for column } N \end{array} \right] \equiv y_{(1,N)} \right] \cdot \left[\left[\begin{array}{c} \text{conjugate of 1st} \\ \text{harmonic in } x \\ \text{for row 2} \end{array} \right] \equiv x^{*}_{(1,2)} \right]$$

$$(A-11)$$

$$T_{(N-1,2)} = \left[\left[\begin{array}{c} \text{conjugate of 1st} \\ \text{harmonic in } y \\ \text{for column 2} \end{array} \right] \equiv y^{*}_{(1,2)} \right] \cdot \left[\left[\begin{array}{c} \text{1st harmonic in } x \\ \text{for row } N-1 \end{array} \right] \equiv x_{(1,N-1)} \right]$$

$$(A-12)$$

$$T_{(N-1,N)} = \left[\left[\begin{array}{c} \text{conjugate of 1st} \\ \text{harmonic in } y \\ \text{for column } N \end{array} \right] \equiv y^{*}_{(1,N)} \right] \cdot \left[\left[\begin{array}{c} \text{conjugate of 1st} \\ \text{harmonic in } x \\ \text{for row } N-1 \end{array} \right] \equiv x^{*}_{(1,N-1)} \right]$$

$$(A-13)$$

if $y_1 < N/2$, $x_1 < N/2$

$$T_{(y_1,x_1)} = \left[\left[\begin{array}{c} (y_1-1) \text{ harmonic in } y \\ \text{for column } x_1 \end{array} \right] \equiv y_{(y_1-1,x_1)} \right] \cdot$$
$$\left[\left[\begin{array}{c} (x_1-1) \text{ harmonic in } x \\ \text{for row } y_1 \end{array} \right] \equiv x_{(x_1-1,y_1)} \right]$$

If the variation in intensity across every row is equal to the variation in intensity for every other row and the variation across all of the columns is similarly set equal, then the componenets of the transform can be defined as

$$y_{(1,2)} = a + jb \qquad x_{(1,2)} = c + jd$$
$$y_{(1,N)} = a + jb \qquad x_{(1,N-1)} = c + jd$$
$$y^{*}_{(1,2)} = a - jb \qquad x^{*}_{(1,2)} = c - jd \qquad (A-14)$$
$$y^{*}_{(1,N)} = a - jb \qquad x^{*}_{(1,N-1)} = c - jd$$

Using Equation (A-14) to solve (A-10) through (A-13)

$$T_{(2,2)} = y_{(1,2)} x_{(1,2)} = (a+jb)(c+jd) = (ac-bd) + j(bc+ad) \qquad (A-15)$$

$$T_{(2,N)} = y_{(1,N)} x^{*}_{(1,2)} = (a+jb)(c-jd) = (ac+bd) - j(ad-bc) \qquad (A-16)$$

$$T_{(N-1,2)} = y^{*}_{(1,2)} x_{(1,N-1)} = (a-jb)(c+jd) = (ac+bd) + j(ad-bc) \qquad (A-17)$$

$$T_{(N-1,N)} = y^{*}_{(1,N)} x^{*}_{(1,N-1)} = (a-jb)(c-jd) = (ac-bd) - j(ad+bc) \qquad (A-18)$$

Equation (A-15) for $T_{(2,2)}$ is the conjugate of Equation (A-18) for $T_{(N-1,N)}$ under the conditions of uniform variations on any row and similarly for the columns, which just implies separability.

120

To implement the two-dimensional Fourier Transform, sub-
routine Fourt, a common Fortran Subroutine, was used. To
test subroutine Fourt to see where it places harmonics with a
two-dimensional array, the results of Equations (A-15) through
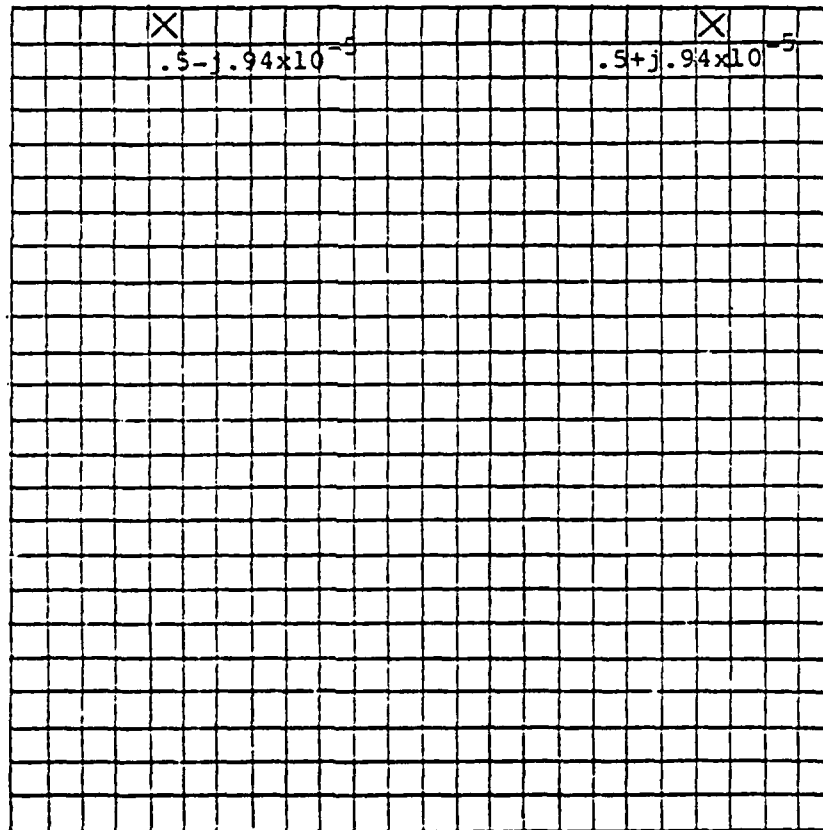(A-18) were used. Figures A-2 through A-7 show the results
of these tests.

Figure A-2 - Cos 2πx/6

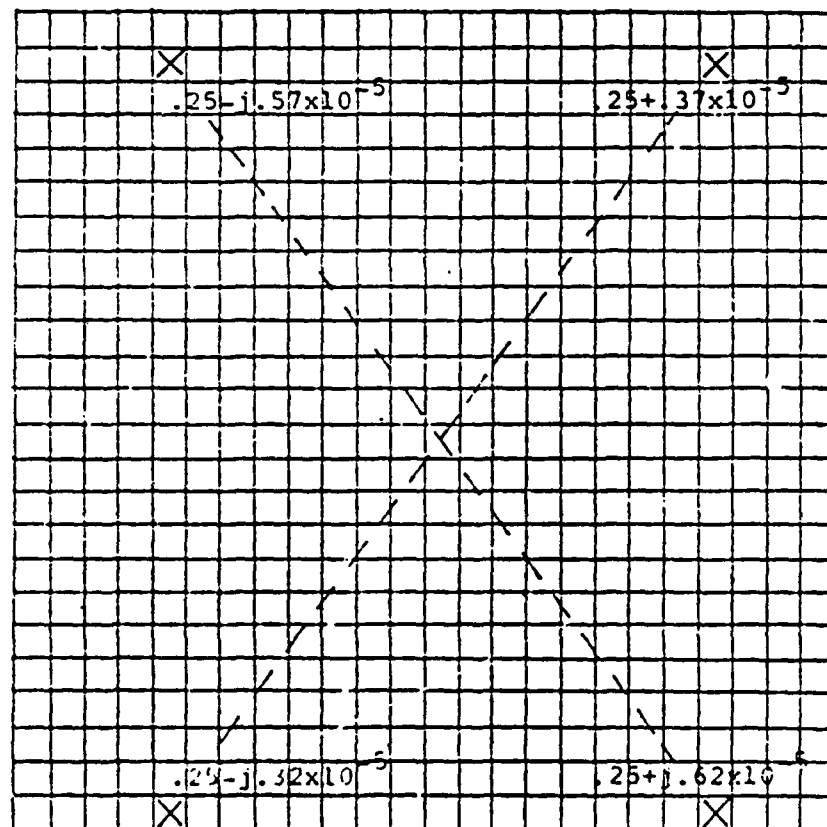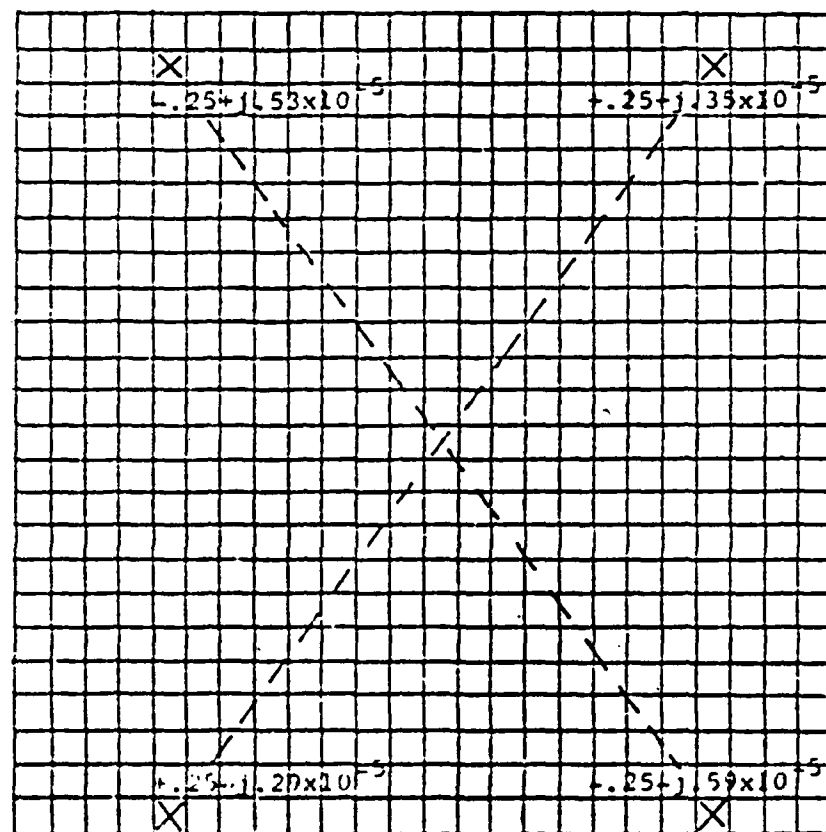Figure A-3 - $(\cos 2\pi x/6)(\cos 2\pi y/24)$
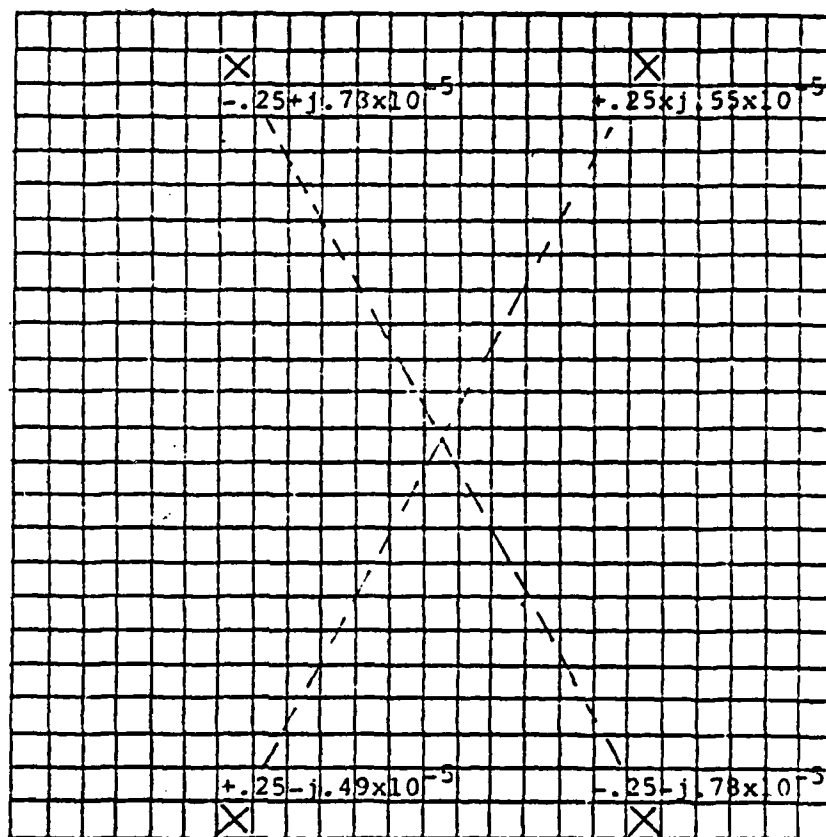
Figure A-4 - $(\sin 2\pi x/6)(\sin 2\pi y/24)$
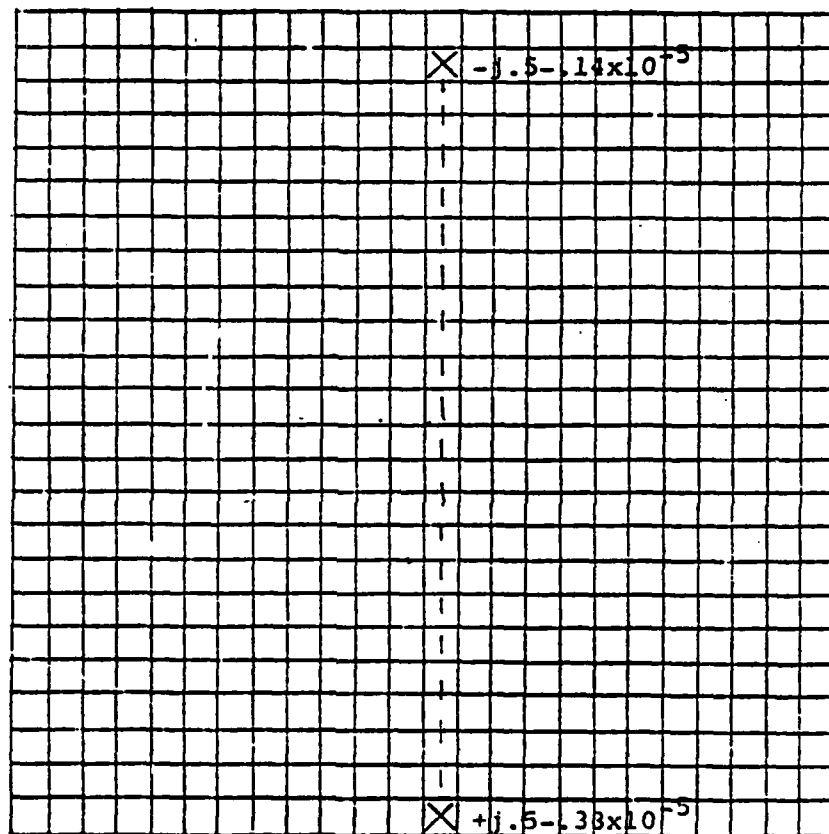
123

Figure A-5 - (sin 2πx/4)(sin 2πy/24)

Figure A-6 - $(\cos 2\pi x/2)(\sin 2\pi y/24)$
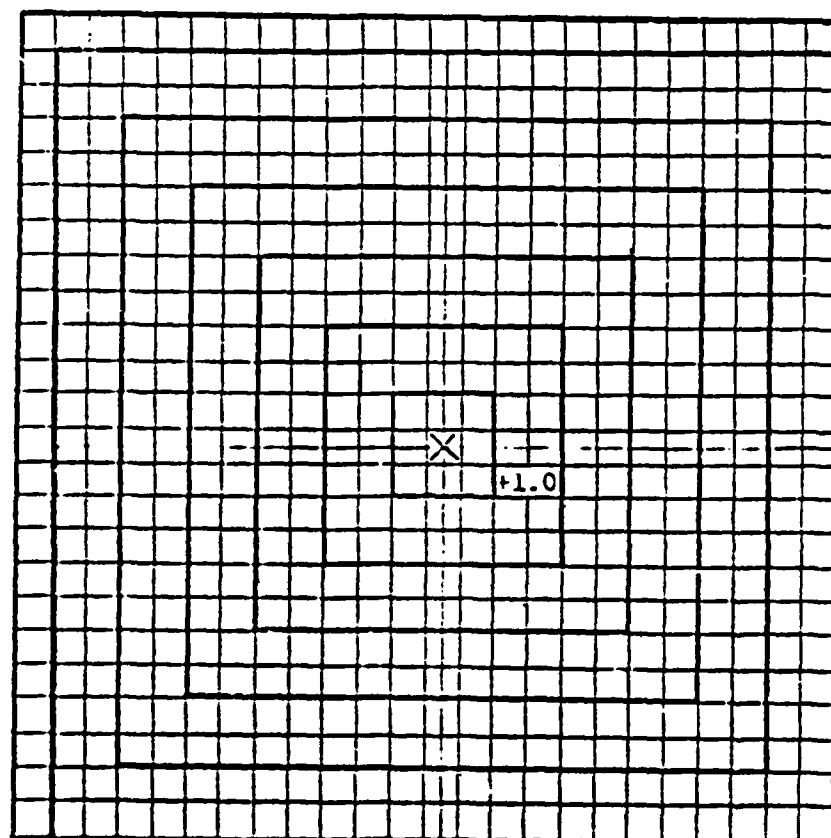
Figure A-7 - $(\cos 2\pi x/2)(\cos 2\pi y/2)$

Figure A-1 had as its input a 24x24 array with magnitudes of each element varying only across the rows via cos(2πx/6). Using the above interpretation of a two-dimensional Fourier Transform, the fundamental frequency assumed would be one which corresponded to one period across the 24-element array. Since the input obviously fits four cycles in that space, the only nonzero component of the Fourier Transform expected would be at the fourth harmonic. The transform would also be expected to be real only since the input is a pure cosine. Figure A-2 is then encouraging in that the only nonzero components are where expected and the imaginary portions of that answer are extremely small. The reason that there are nonzero elements only in the first row is that when the transform was accomplished across the columns, there was no variation in the y-coordinate, which is equivalent to taking a transform of a constant one. That transform results in a one in the zero frequency components of each column which is the first row and zero everyplace else. When the multiplication of Equation (A-9) is accomplished, Figure A-2 results.

Figure A-3 had an input of (cos 2πx/6)(cos 2πy/24) which is the same variation in the x-direction and a variation in the y-direction which corresponds to exactly one period. The only nonzero result from the transform along the columns, variation in y, should be along the fundamental, which it is.

Figures A-4 through A-7 are just further examples to demonstrate Fourt. Figure A-4 had an input of the fourth harmonic in the x-direction and the fundamental in the y-direction. Figure A-5 contains the sixth harmonic in the x-direction. Figure A-6 contains the twelfth harmonic in the x-direction which only appears as a conjugate. Figure A-7 contains only the twelfth harmonic in both directions and encloses spatial frequencies within boxes. A thorough understanding of these results is needed to understand the processes of taking derivatives and shifting in the transform domain.

127

In summary, Figure A-8 is provided to show the output of subroutine Fourt. The DC component is the product of the zero frequency components of the one-dimensional transforms in both directions. Elements $T_{(1,2)}$ through $T_{(24,24)}$ can be interpreted similarly to Equations (A-10) through (A-13).
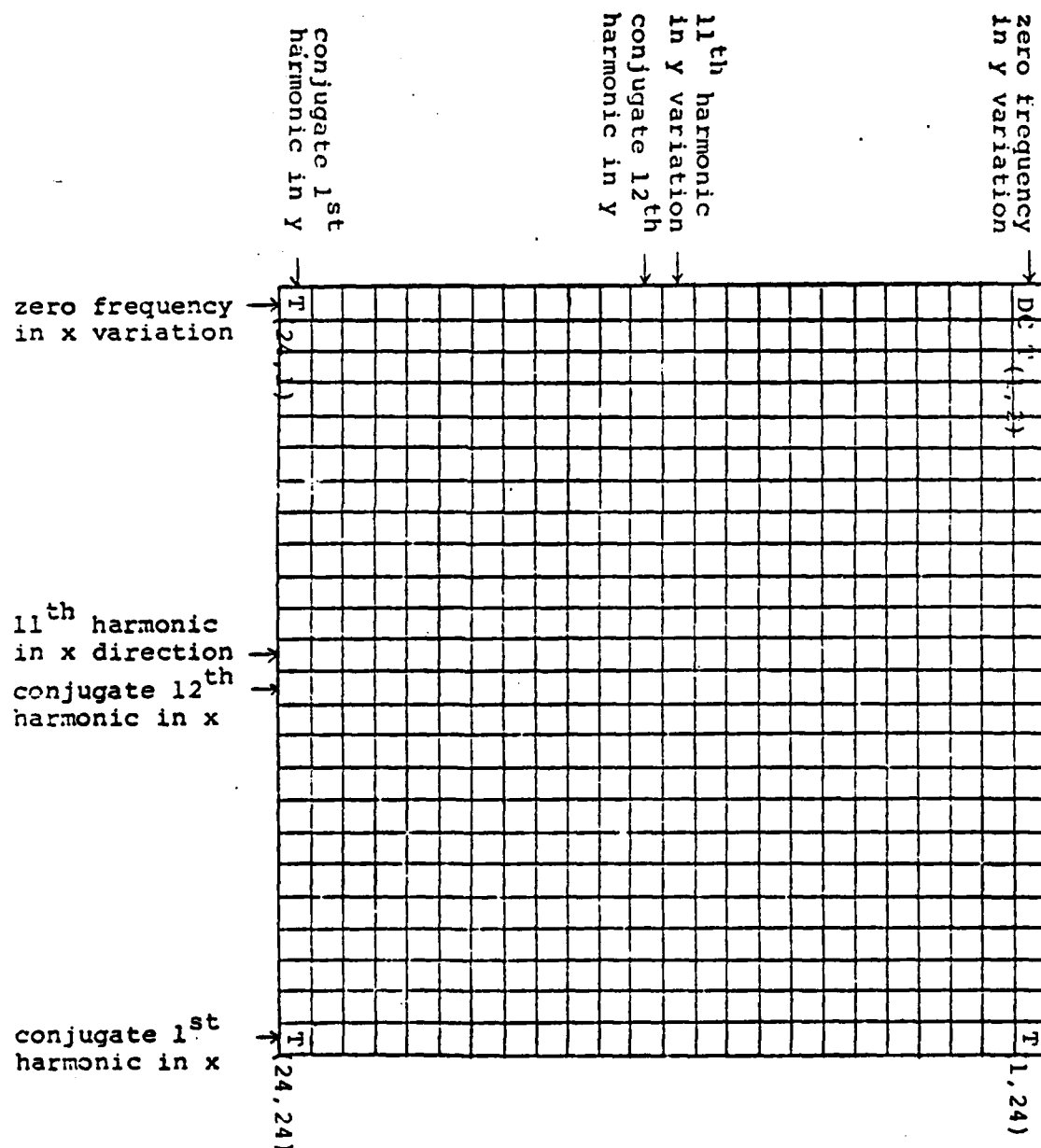

Figure A-8 - Output of Fourt

128

Derivation of the $\underline{\Phi}_F$ Matrix

The derivation of the linearized $\underline{F}$ and $\underline{\Phi}_F$ matrices for the nonlinear constant turn-rate target acceleration dynamics model is not as simple as it is for a linear filter. This is because the point of linearization is dependent on the current value of the state vector and cannot be precomputed. Repeating Equation (4-16)

$$\underline{F}(t_i) = \partial \underline{f}[\underline{x},t]/\partial \underline{x} \Big|_{\underline{x}=\hat{\underline{x}}(t_i^+)} \qquad (B-1)$$

and recalling the definition of the nonlinear function $\underline{f}|x(t),t|$ from Equation (4-12), the $\underline{F}$ matrix has the form

$$\underline{F}(t_i) = \begin{bmatrix} 0 & 0 & 1 & 0 & 0 & 0 & 0 & 0 \\ 0 & 0 & 0 & 1 & 0 & 0 & 0 & 0 \\ 0 & 0 & 0 & 0 & 1 & 0 & 0 & 0 \\ 0 & 0 & 0 & 0 & 0 & 1 & 0 & 0 \\ 0 & 0 & F1 & F2 & F3 & F4 & 0 & 0 \\ 0 & 0 & F5 & F6 & F7 & F8 & 0 & 0 \\ 0 & 0 & 0 & 0 & 0 & 0 & F9 & 0 \\ 0 & 0 & 0 & 0 & 0 & 0 & 0 & F9 \end{bmatrix} \qquad (B-2)$$

where

$$F1 = -(\omega/A1)(A2 - 4\omega x_3^2 + 2x_3 x_6)$$

$$F2 = 2x_3 \omega (x_5 A1 + 2x_4 A2)/A1^2$$

$$F3 = 2x_3 x_4 \omega / A1$$

$$F4 = -2x_3^2 \omega / A1$$

$$F5 = -2x_4 \omega (x_6 A1 + 2x_4 A2)/A1^2$$

$$F6 = -\omega [\omega - 2x_4 (x_5 A1 + 2x_4 A2)/A1^2]$$

$$F7 = 2x_4^2 \omega / A1$$

$$F8 = -2x_3 x_4 \omega / A1$$

$$F9 = -1/\tau_A$$

in which

$$A1 = x_3^2 + x_4^2$$

$$A2 = x_3 x_6 - x_4 x_5$$

$$\omega = A2/A1$$

τ_A = correlation time of the atmospheric jitter

and with the components of the state vector specified in Chapter Iv written as

$$\underline{x} = [x_1 \ x_2 \ x_3 \ x_4 \ x_5 \ x_6 \ x_7 \ x_8]^T$$

Once the $\underline{F}(t_i)$ matrix is determined, the state transition matrix can be evaluated using the quasi-static approximation of Equation (4-19) except for the two atmospheric terms which are obtained in exact closed form. Specifically, this approximation results in the form of

$$\underline{\Phi}_F(t_{i+1}, t_i) = \begin{bmatrix} 1 & 0 & A & 0 & B & 0 & 0 & 0 \\ 0 & 1 & 0 & A & 0 & B & 0 & 0 \\ 0 & 0 & 1 & 0 & A & 0 & 0 & 0 \\ 0 & 0 & 0 & 1 & 0 & A & 0 & 0 \\ 0 & 0 & C1 & C2 & C3 & C4 & 0 & 0 \\ 0 & 0 & C5 & C6 & C7 & C8 & 0 & 0 \\ 0 & 0 & 0 & 0 & 0 & 0 & D & 0 \\ 0 & 0 & 0 & 0 & 0 & 0 & 0 & D \end{bmatrix} \quad (B-3)$$

where

$$A = \Delta t \qquad\qquad B = \Delta t^2/2$$

$$C1 = \Delta t F1 \qquad\qquad C2 = \Delta t F2$$

$$C3 = \Delta t F3 + 1 \qquad\qquad C4 = \Delta t F4$$

$$C5 = \Delta t F5 \qquad\qquad C6 = \Delta t F6$$

$$C7 = \Delta t F7 \qquad\qquad C8 = \Delta t F8 + 1$$

$$D = \exp(-\Delta t/\tau_A)$$

Vita

William A. Roemer was born on September 30, 1949 in Emory University, Georgia. After several years enlisted experience in the Air Force, he was selected for the Airman Education and Commissioning Program, graduating with a Bachelor of Science in Engineering degree from Arizona State University with high honors in May 1979. After commissioning in August 1979, Second Lieutenant Roemer was assigned to the National Security Agency at Fort George G. Meade, Maryland, and worked in the field of optical processing for three years. He was then selected to attend the Air Force Institute of Technology to pursue a Master of Science Degree in Electrical Engineering (Electro-Optics). Captain Roemer is a member of both the Optical Society of America and the Society of Photo-Optical and Instrumentation Engineers.

Permanent Address: 59 Commonwealth Avenue
Newark, NJ 07106

REPORT DOCUMENTATION PAGE

1a. REPORT SECURITY CLASSIFICATION UNCLASSIFIED		1b. RESTRICTIVE MARKINGS	
2a. SECURITY CLASSIFICATION AUTHORITY		3. DISTRIBUTION/AVAILABILITY OF REPORT	
2b. DECLASSIFICATION/DOWNGRADING SCHEDULE		Approved for public release; distribution unlimited.	
4. PERFORMING ORGANIZATION REPORT NUMBER(S) AFIT/GEO/EE/ 84M-2		5. MONITORING ORGANIZATION REPORT NUMBER(S)	

6a. NAME OF PERFORMING ORGANIZATION School of Engineering	6b. OFFICE SYMBOL (If applicable) AFIT/ENG	7a. NAME OF MONITORING ORGANIZATION
6c. ADDRESS (City, State and ZIP Code) Air Force Institute of Technology Wright-Patterson AFB, Ohio 45433		7b. ADDRESS (City, State and ZIP Code)

8a. NAME OF FUNDING/SPONSORING ORGANIZATION	8b. OFFICE SYMBOL (If applicable)	9. PROCUREMENT INSTRUMENT IDENTIFICATION NUMBER		

8c. ADDRESS (City, State and ZIP Code)	10. SOURCE OF FUNDING NOS.			
	PROGRAM ELEMENT NO.	PROJECT NO.	TASK NO.	WORK UNIT NO.

11. TITLE (Include Security Classification)
See Box 19

12. PERSONAL AUTHOR(S)
William A. Roemer, B.S.E., Capt, USAF

13a. TYPE OF REPORT MS Thesis	13b. TIME COVERED FROM _____ TO _____	14. DATE OF REPORT (Yr., Mo., Day) 1984 March	15. PAGE COUNT 145

16. SUPPLEMENTARY NOTATION

Approved for public release: IAW AFR 190-17.

LYNN E. WOLAVER   7 May 84

Dean for Research and Professional Development

Air Force Institute of Technology (ATC)

17.	COSATI CODES		18. SUBJECT TERMS (Continue on reverse if necessary and identify by block number)
FIELD	GROUP	SUB. GR.	Kalman Filters, Optical Processing, Pipelined Iterative Optical Systolic Arrays

19. ABSTRACT (Continue on reverse if necessary and identify by block number)

Title: AN OPTICALLY-IMPLEMENTED KALMAN FILTER ALGORITHM

Thesis Chairman: Dr. Peter S. Maybeck

20. DISTRIBUTION/AVAILABILITY OF ABSTRACT	21. ABSTRACT SECURITY CLASSIFICATION	
UNCLASSIFIED/UNLIMITED ☒ SAME AS RPT. ☐ DTIC USERS ☐	UNCLASSIFIED	

22a. NAME OF RESPONSIBLE INDIVIDUAL Dr. Peter S. Maybeck	22b. TELEPHONE NUMBER (Include Area Code) 513-255-3576	22c. OFFICE SYMBOL AFIT/ENG

DD FORM 1473, 83 APR   EDITION OF 1 JAN 73 IS OBSOLETE.

    An extended Kalman filter algorithm which incorporates
an enhanced correlator/linear measurement model and a non-
linear target acceleration dynamics model is described for
use in a pointing and tracking system for high-energy ground-
based laser weaponry. The measurement model used in the
filter combines the computational benefits of a correlation
algorithm with the statistical accuracy available from a
Kalman filter. The dynamics model, based on a constant
turn-rate target acceleration model, is deemed to be a better
representation of the true target dynamics than a linear
first-order Gauss-Markov target acceleration model for the
cases of interest. Optical processing techniques are com-
pletely specified for the correlation stage to perform the
required correlations in real time, and the filter stage to
perform the linear algebra required for the Kalman filter.
This extensive use of optics allow the development of two
tracking algorithms based on the same models: a FLIR-con-
strained tracker with a 30 Hz frame rate and an unconstrained
tracker with a 100 Hz frame rate using real-time sensors in
place of the FLIR.

END

FILMED

DTIC